UNIVERSITY OF OKLAHOMA

GRADUATE COLLEGE

INVESTIGATING THE REGIONAL AND LOCAL STRUCTURE OF OKLAHOMA'S CRUST USING INDUCED EARTHQUAKES

A DISSERTATION

SUBMITTED TO THE GRADUATE FACULTY

in partial fulfillment of the requirements for the

Degree of

DOCTOR OF PHILOSOPHY

by

PRANSHU RATRE

Norman, Oklahoma

2021

Downloaded from SHAREOK. Persistent Handle URL: https://hdl.handle.net/11244/332428

INVESTIGATING THE REGIONAL AND LOCAL STRUCTURE
OF OKLAHOMA'S CRUST USING INDUCED EARTHQUAKES

A DISSERTATION APPROVED FOR THE
SCHOOL OF GEOSCIENCES

BY THE COMMITTEE CONSISTING OF

Dr. Brett M. Carpenter, Chair

Dr. Michael Behm, Co-Chair

Dr. Xingru Wu

Dr. Xiaowei Chen

Chapter[2] © American Geophysical Union 2021
Used by permission
All other content © Copyright by PRANSHU RATRE 2021
All rights reserved.

TABLE OF CONTENTS

Table of Contents iv

List of Tables vii

List of Figures viii

Acknowledgments xiv

Abstract of the dissertation xvi

1 Introduction 1
- 1.1 Oklahoma: A Missing Piece in the Precambrian Assemblage of North America . . . 1
- 1.2 Seismicity in Oklahoma . . . 3
- 1.3 Structure of the Dissertation . . . 5
- Bibliography . . . 9

2 Imaging the deep crustal structure of central Oklahoma using stacking and inversion of local earthquake waveforms 10
- 2.1 Abstract . . . 10
- 2.2 Introduction . . . 11
- 2.3 Regional Geology and Previous Geophysical Studies . . . 15
  - 2.3.1 Geology . . . 15
  - 2.3.2 Previous Seismic Studies . . . 17
- 2.4 Data and Methodology . . . 20
  - 2.4.1 Data . . . 23
  - 2.4.2 Pg Processing . . . 23
    - 2.4.2.1 Geometric and Kinematic Corrections (Datuming) . . . 24
    - 2.4.2.2 Pre-stack Signal Processing . . . 25
    - 2.4.2.3 CMP Sorting and Stacking . . . 27
    - 2.4.2.4 Travel Time Curve Picking . . . 28
    - 2.4.2.5 1-D Travel Time Inversion and Combination into a 3-D Model . . . 30
  - 2.4.3 Other Crustal Phases (PmP, Pn, Reflections/Refractions from within the Uppermost Mantle) . . . 35
- 2.5 Discussion and Interpretation . . . 37

2.5.1 Assessment of the 3-D Velocity Model 37
2.5.2 Comparison with Existing Velocity Models 39
2.5.3 Crustal Structures 40
2.5.4 Implications on the Midcontinent Rift (MCR) Structure 45
2.5.5 Seismic Velocities and Spatial Distribution of Seismicity 47
2.6 Conclusions 48
2.7 Supplementary Materials 50
2.7.1 Introduction 50
2.7.2 Resolution Assessment 50
Bibliography 73

3 Shear wave velocity structure and compositional analysis of the crustal structure in Oklahoma 74
3.1 Abstract 74
3.2 Introduction 75
3.3 Previous Seismic Studies 77
3.4 Data and Methodology 78
3.4.1 Data 78
3.4.2 Methodology 80
3.5 Discussion and Interpretation 85
3.5.1 Comparison with Existing Velocity Model 85
3.5.2 Crustal Structures 90
3.5.3 V_P/V_S Ratio and Compositional Analysis 93
3.6 Conclusions 97
Bibliography 104

4 Earthquake depth and local velocity estimation using crustal reverberations and phase correlation for the Cushing Fault zone 105
4.1 Abstract 105
4.2 Introduction 106
4.3 Data 108
4.4 Methodology 109
4.4.1 Earthquake Relocation 109
4.4.2 Travel Time Modeling 110
4.4.2.1 Phase Identification 110
4.4.2.2 Basement Depth Determination 112
4.4.3 Forward Waveform Modelling and Earthquake Depth Estimation 114
4.5 Results 115
4.5.1 Event Relocation 115
4.5.2 Basement Depth and V_P/V_S Estimates 116
4.5.3 Constraints on Earthquake Depth 117
4.6 Discussion 118
4.7 Conclusions 121

Bibliography 124

5 Conclusions **125**
5.1 Summary of Results 125
5.2 Future Work 127
Bibliography 129

LIST OF TABLES

Table 4.1 Original event locations and magnitudes. 116
Table 4.2 Relocated event locations and depth estimates from Velest relocation. Last column shows the final depth estimates derived using phase delay times. 116

LIST OF FIGURES

Figure 2.1 Tectonic provinces in the central part of the midcontinent (Modified from Bickford et al. (2015)). Bouguer gravity anomalies (based on Decade of North American Geology (DNAG) data) are shown after applying a 200 km high-pass wavelength filter to suppress upper mantle features. A possible continuation of the Midcontinent Rift (MCR) in Oklahoma is shown as proposed by previous studies. (EGRP: Eastern Granite-Rhyolite province). Study area shown in black dashed box. 13

Figure 2.2 Major tectonic features in Oklahoma (adapted from Northcutt and Campbell (1996). Red dashed lines: major fault systems. Black solid lines: depth-to-basement contours (meters) computed from basement well information as given by Campbell and Weber (2006). Areas beyond the state of Oklahoma are in white. 18

Figure 2.3 Black thick lines: previous active seismic studies conducted in Oklahoma for crustal investigations. Red dots: location of earthquakes used in this study. Blue triangles: recording stations used in this study. Areas beyond the state of Oklahoma are in white. 21

Figure 2.4 Example of preprocessing on one datum-corrected event gather with a linear move-out for a velocity of 6 km/s. a) bandpass filtered (2-4-6-8 Hz), b) signal converted to envelope, c) STA/LTA applied. 26

Figure 2.5 Measures of lateral resolution and trace fold for the CMP bins (a) bin size, (b) number of traces in each bin. CMP bin center locations are shown as "x". 28

Figure 2.6 Comparison of CMP stacks for 10%, 50%, and 100% data sets (see text for details). Red arrows indicate non-physical deviations from a 1-D travel time curve. 29

Figure 2.7 Examples of CMP stacks from different locations. The map on the right shows the location and size of the CMP bin for each of the stacked gathers. Small black dots: location of individual trace midpoints within one CMP bin. Blue cross: CMP bin center locations. Red line (on stacks): picked travel times. Green line (on stacks): theoretical travel-time curve based on 1-D velocity model for continental shields. 31

Figure 2.8 Processing steps illustrated for one CMP bin. (a) All source-receiver pairs (grey lines) shown for the CMP bin (black square); (b) Pre-processed earthquake waveforms in this CMP gather with a linear move-out correction of 6 km/s; (c) Stacked gather obtained from 5 km offset-bin stacking of sorted gather in b), red dashed line shows the picked travel time curve; (d) Initial and inverted 1-D velocity model, and resolution elements obtained for the CMP bin location. 33
Figure 2.9 Horizontal slices through the 3-D Pg wave velocity model superimposed on the geologic provinces map. Note the varying color scale for each depth slice (same range of 500 m/s). Black contour lines show the Bouguer Gravity anomaly [mGal]. Regions A, B and C are discussed in the text. 34
Figure 2.10 Examples of event gathers with interpreted Pg and Pn phases. The expected offset range for over-critical PmP arrivals is indicated by the blue arrow. Long offsets result from inclusion of US Array stations outside the investigated area. Strong Pn amplitude at large offsets might also represent a reflection from within the lithospheric mantle (PlP). 35
Figure 2.11 Three bandpass filtered, LMO corrected, and bulk-shifted event gathers with respective event locations (red dot) and receiver locations (blue triangles) shown in map insets. The red curve plotted on each of the event gathers represents the calculated first arrival travel time for our final 3-D velocity model. . 38
Figure 2.12 Pg-velocity model cross-sections. Bouguer gravity anomaly (red curve) and magnetic anomalies (green curve) are plotted above corresponding cross sections. On cross sections, black vertical lines show fault locations and blue vertical lines show extent of regions (A,B,C). Inset maps show the fault locations (grey lines), location of regions A,B,C (blue polygons) overlain on geologic province map. "Proposed MCR" indicates the tentative continuation of the Midcontinent Rift as suggested by previous studies. See text for discussion. 43
Figure 2.13 a) Earthquake locations; b) Total injection volume (MMbbl) for saltwater disposal wells from 2011-2017, overlain on the velocity slice at 5 km depth. The absence of seismicity in the high-velocity regions is discussed in section 2.5.5. 48
Figure S2.14 Depth distribution of earthquakes used in this study. . 52
Figure S2.15 Range of time and offset corrections for raytracing-based re-datuming to a reference level Z=5 km as a function of source-receiver offset and earthquake depth. Each point on the graphs represent one source-receiver pair. The scatter is caused by the non-linear relationships between ray geometry, basement depths, earthquake depths, velocity distribution, and source-receiver offset. Colors represent earthquake depth (km). 53

Figure S2.16 Resolution elements for each velocity element at a given depth and CMP location shown for 5-40 km depth slices. . . . 54
Figure S2.17 We test for dependency on initial model during inversion by inverting for different initial models. Left panel: Initial velocity models used for inversion. The black line shows initial velocity model used in this study. Coloured lines show perturbations introduced to the initial model (in black). Middle panel: Examples of 1-D velocity model computed using the perturbed models as initial models for real travel times from three different locations in this study. Right panel: Corresponding percentage change for each of the final velocity models computed from modified initial models when compared to final velocity model reported in the study. For up to 15% perturbations in the initial model we only observe deviations of $\sim$ +/-0.2% with a maximum deviation of $\sim$1%. 55
Figure S2.18 Histograms for RMS travel time residuals before (blue) and after (red) 1-D travel time inversion. Used data points are the RMS residuals of all 1-D inversions (n=686). 56
Figure S2.19 Relative Pg and PmP amplitudes without spherical spreading, calculated for a representative 1-D crustal model, a Moho depth of 42 km, and an event depth of 5.5 km. The strong Pg amplitude in the critical PmP offset range as well as similar travel times of the two phases illustrates the difficulty of identifying a clear PmP phase in the data. 56
Figure S2.20 (a,c,e) show velocities in Z, X and Y directions respectively for bin#1. (b,d,f) show velocities in Z, X and Y directions respectively for bin#2. Source, receiver and mid-point locations for each of the bins are shown in (a,b). 57
Figure S2.21 Modeled travel times and corresponding inverted velocity model for bin#1 are shown in blue in a) and b) respectively. Modeled travel times and corresponding inverted velocity model for bin#2 are shown in blue in c) and d) respectively. Orange and yellow lines in (a,c) show the corresponding 1D travel time curves for locations at the rift axis and outside the rift, respectively. Higher velocity estimates as compared to velocity model with no MCR, are obtained for both the bins using the source-receiver geometry used in this model. This implies that the source-receiver geometry used in the model is sufficient to estimate velocity anomalies that may result from highly mafic structure of the MCR. 58

Figure S2.22 A comparison of velocity model from Chen (2016) and current study. 2-D velocity profiles A4 and A5 refer to figures 2.17d and 2.17e in Chen (2016) thesis. a) and c) show lines A4 and A5 respectively, adapted from Chen (2016); and b) and d) show lines A4 and A5 respectively as computed in current study. Blue box shows the extent of velocity model by Chen (2016) for respective profiles. They interpret high velocity anomalies shown in red box, to be correlated to Midcontinent rift as shown in a) and c). Here we observe that in deeper sections, the high velocity anomaly either disappears (as in b)) or becomes less prominent (as in d)). This lends to the interpretation that these velocity anomalies are present mostly in the upper crust and may not be related to a lower crustal rift structure. They also interpret intrusions on the eastern side of profiles A4 and A5 (a) and c)). We observe similar high velocity anomalies in the same area (ref. Figure 2.9 region B in main text). 60
Figure S2.23 Ray paths computed for earthquake depth of 3km, 4km, 5km, and 6km (top to bottom), for an averaged 1-D velocity model of the crust. For this model basement depth is assumed at 2.2 km. It is evident from the ray path geometries that for source-receiver offset greater than ∼65km, ray paths sample depths greater than 10km. So, the assumption of Pei et al. (2018) to average velocities for 5-10 km depth, derived from offsets as far as 120-130 km could introduce a bias in their model. 60

Figure 3.1 Red dots: location of earthquakes used in this study. Blue triangles: recording stations used in this study. Areas beyond the state of Oklahoma are in white. 79
Figure 3.2 a,b) and c,d) show East and North component for two events respectively. The traces are bandpass filtered (4-6-10-12 Hz) and LMO corrected with a velocity of 3.45 km/s. (Note: These values are only used for visualization and not part of processing routine). 81
Figure 3.3 Example of preprocessing on one datum-corrected event gather with LMO correction applied for a velocity of 3.45 km/s. (a) Signal converted to envelope + bandpass filtered (0.5-2-4-6 Hz), (b) STA/LTA applied 82
Figure 3.4 (a)Number of traces in each bin, (b)CMP bin size. . . . 83
Figure 3.5 Processing steps illustrated for one CMP bin. (a) All source-receiver pairs shown for the CMP bin (black square); (b) Pre-processed earthquake waveforms in this CMP gather with a linear move-out correction of 3.45 km/s; (c) Stacked gather obtained from 5 km offset-bin stacking of sorted gather in (b), red dashed line shows the picked travel time curve; (d) Initial and inverted 1-D velocity model for the CMP bin location. . . 85

Figure 3.6 Horizontal slices through the 3-D Sg wave velocity model superimposed on the geologic provinces map. Note the varying color scale for each depth slice (same range of 250 m/s). Black contour lines show the Bouguer Gravity anomaly [mGal]. Regions A, B, and C are discussed in the text. 87
Figure 3.7 Horizontal slices through the 3-D Vp/Vs model superimposed on the geologic provinces map. Black contour lines show the Bouguer Gravity anomaly [mGal]. Regions A, B, and C are discussed in the text. 88
Figure 3.8 Box plot depicting the variation of Sg velocity with depth for central Oklahoma. Light blue: Zhu et al. (2018), red: Tan et al. (2021), black: this study 89
Figure 3.9 Sg velocity model cross sections. Bouguer gravity anomaly (red curve) and magnetic anomalies (green curve) are plotted above corresponding cross sections. On cross sections, black vertical lines show fault locations and blue vertical lines show extent of Regions (A, B, and C). Inset maps show the fault locations (gray lines), location of Regions A, B, and C (blue polygons) overlain on geologic province map. See text for discussion. 92
Figure 3.10 Plots of (a)V_P/V_S vs V_P and (b) Poisson's ratio vs V_P for upper, middle and lower crust of Oklahoma. Plots compare the data from this study to a) V_P and V_S relationships derived by Brocher (2005); b) Poisson's ratio and V_P values for different rock types compiled by Christensen (1996). Multiple values for the same rock type for the upper, middle and lower crust represent the values at two different lithostatic pressure that would correspond to the the specific layer [Upper crust : 200, 400 MPa, Middle crust : 400, 600 MPa, Lower crust : 800, 1000 MPa. Error bars for rock types represent one standard deviation. 94
Figure 3.11 Box plot showing the distribution of Poisson's ratio data from this study across depth and mineral composition. Center horizontal line in each box plot diagram represents the median depth. The data are sorted according to Poisson's ratio and P wave velocity bounds of each of the rock types. Anorthite content shown within the plagioclase field. 95

Figure 4.1 Left: Overview of tectonic provinces and faults in Oklahoma. The black square shows the location of the Cushing Fault zone. Right: Map view of nodal array stations (blue triangles) and earthquake locations (black dots) from Oklahoma Geological Survey (OGS) catalog from October 2014 to May 2018. The background is the basement depth map derived from basement penetrating wells (Northcutt and Campbell, 1996). The three cyan circles indicate earthquakes used in this study. 108

Figure 4.2 a,b)Event waveform aligned using the original catalog location and relocation from Velest. Red dots indicate the picked P and S arrival times for each event. c) P wave velocity model derived from Tan et al., 2021 used for relocation. d) Map and cross section views showing the location of events before and after Velest relocation. Black dots denote seismicity used in Qin et al.,2019 for the Cushing fault zone. 110
Figure 4.3 Map and cross section view for the three events showing the 90% confidence interval (black dashed ellipse) based on bootstraping. 111
Figure 4.4 Comparison of modelled travel times for different phases and observed data. Blue arrows show increase in delay time between P and S-to-P phases with offset and a similar observation noted on observed waveform. Green arrows show the almost constant delay time between S-to-P and S phases in the modelled waveform which is consistent with the observed arrivals as shown. 112
Figure 4.5 a)For a given velocity model: delay time between S and S_P increases as basement depth increases, b) Delay times between S and S_P arrivals vs offset when plotted for different earthquake depths shows that earthquake depth has almost no influence on the delay time beyond 3 km offsets, c) Delay times between S and S_P arrivals vs earthquake depth for different offsets, offsets beyond 3.5 km are not clearly differentiated as the delay times for those remain constant. 115
Figure 4.6 (top) Distribution of basement depth estimates at each station (offset >1 km) from each of the three events [Red:5813, Blue:5815, Green:5816], (bottom) histogram distribution of basement depth estimates show that basement depth estimates for majority of stations lie between 1.04 and 1.06 km. 117
Figure 4.7 P - S_P delay time misfits plotted for the three events. Minimum value of misfit represents the chosen final depth estimates for each of the events. 118

Acknowledgments

This work would not have been possible without the amazing people who have been an integral part of this journey.

I would first like to thank my advisor, Dr Michael Behm, for his guidance and motivation throughout my PhD journey. His knowledge and patient approach made me comfortable to ask questions even if they sounded irrelevant in my head. He was always available to discuss research questions and his attention to detail has helped me become a better researcher and evaluate all the possibilities when working on a problem. His knowledge of geophysics field work has helped me immensely in understanding the do's and don'ts when out in the field. I am grateful for his mentoring in different Geophysical techniques and giving me the unique opportunity to be part variety of field experiences. Gaining the knowledge and experience in such a wide range of topics has helped me be a better Geophysicist and given me the confidence to explore new research avenues. Thank you Michael for your mentorship.

I would like to express my sincere gratitude towards Dr. Brett Carpenter for encouraging me and helping me finish my work through the last year. He showed confidence in me and my work, that I had lost in the weird and complicated last year of my PhD. His empathy and motivation gave me the confidence to get through one of the most difficult year. I would also like to thank Dr. Xiaowei Chen for providing the opportunity for summer projects one of which ultimately became a chapter in this dissertation. Her guidance and enthusiasm helped me explore new research avenues that I would not have thought otherwise. I am extremely grateful to her for offering me a postdoc opportunity that will allow me to pursue exciting new questions in seismology. I would also like to thank Dr Xingru Wu and Dr Marianne Karplus for their insightful questions and discussions that has immensely improved this work.

I would also like to sincerely thank the teachers and staff at the department who have made this journey enjoyable and rewarding. The research facilities and funding opportunities at the School of Geosciences at OU is some of the best I have experienced and I am grateful to have benefited from all of it.

I am grateful for my friends here in the department — Anna, Colin, Deepankar, Folarin, Raymond, Yan, and Zhuobo. The board games, climbing evenings, watching trashy reality TV, day or night coffee breaks, were some of my best and most memorable times here in Oklahoma. Good or bad days you all were always there to get me through it all. I feel lucky to have been surrounded by some of the best people that made the my journey less lonely. I hope and wish for a continued friendship and research collaboration in future.

A special thanks to Arushi Saxena and Shivani Gupta who have been my best friends since undergrad. I am so thankful for you to be part of my life. You both have been always there for me whenever I needed a support whether in my research or in life. I cannot thank you both enough for being a constant support and source of motivation. You both have made me a better person and helped me aspire for higher career goals.

I want to thank my partner in life and research, Pulkit Singh, for making all of this worthwhile. You always had more confidence in my work than I did, and I am grateful for that. You have been a constant source of motivation since the beginning and I would not be here without your support and encouragement.

Lastly and most importantly to Mom and Dad, you are the greatest inspiration and I am so thankful for your love and constant support throughout my studies. You have always pushed me to be better everyday and the only reason I can follow my dreams is because of you. I also want to thank my brothers and my family for their belief in me and encouraging me to achieve my goals. Thank you all for everything!

Abstract of the dissertation

There are still fundamental questions that remain unanswered with respect to the processes involved in the formation and evolution of the continental crust of North America. Data about the rock properties and rock types from the deeper crust can help us answer these questions. Seismic data provides one of the most detailed looks at the characteristics of the rocks in the subsurface. Active tectonic margins are well studied as these regions have a lot of natural seismicity due to active tectonic processes. On the other hand intracratonic regions can be difficult to study due to the lack of such natural seismicity. Deep crustal active seismic studies can be expensive and spatially restrictive. Oklahoma presents a unique case as the intraplate seismicity due to waste water injection provided the data required to evaluate the deep and shallow crustal structures. The combination of high local seismicity, installation of local monitoring stations in response to it, and coincidental overlap of the US Transportable Array can be utilized to study the deep crust of Oklahoma.

To study the deeper crust, I present a non-standard methodology of processing a passive seismic data set. Vertical and horizontal component data with a maximum offset of 250 km is selected for processing. The data are bandpass filtered, converted to envelope, and STA/LTA (short-term average/long-term average) ratio applied. Next, the waveforms are sorted into common-midpoint (CMP) gather and stacked into 5 km offset bins. These steps simplify

the waveforms and increase the signal-to-noise ratio, thus making it easier to identify and pick the P- and S-wave arrivals, especially for far-offset(>150 km) traces. Travel-time curves for each of the CMP bin are picked and inverted to obtain 1-D velocity-depth function at respective CMP bin locations. These are then combined to obtain 3-D P- and S-wave velocity model for the crust of Oklahoma up to 40 km depth. The P- and S-wave velocity models are combined to produce a V_P/V_S ratio and Poisson's ratio model for the crust. The results are enlightening and show a high P-wave velocity (>7 km/s) lower crust for Oklahoma. V_P/V_S ratios of >1.8 are reported for the lower crust. These values suggest a mafic lower crust that possibly formed through mafic underplating and crustal melting. The P- and S-wave velocity anomalies observed in the upper-middle crust are well correlated with local structures and gravity data. This methodology overcomes the limitations of traditional local earthquake tomography where the low S/N ratio for far offsets limits the depth of investigation. Our final velocity models reveal a heterogeneous upper crust that transitions to a more homogenous lower crust.

The source of induced seismicity in Oklahoma has been the waste-water injection operations related to the local petroleum production activities. To understand the earthquake source processes and fault dynamics we need accurate earthquake location estimates. The vast majority of earthquake location algorithms improve on the lateral earthquake location but still have major inaccuracies in the earthquake depth estimates. I use delay times observed between seismic phases to improve depth estimates for the local basement structure and the observed earthquakes. A local nodal array deployment over the Cushing Fault Zone in Oklahoma recorded three earthquake events that occurred on the fault that show seismic phase conversions possibly occurring at the basement interface. Using travel time modelling of the phase delay

times I can establish that the observed phase conversion is an S-to-P (S_P) conversion at the basement and a basement depth of 1.05 km is estimated using the delay times between S_P and S phase arrivals. Using the established basement depth, I model synthetic waveforms for the three events for varying earthquake depths. Finally, I pick the P and S_P arrivals on modelled and observed data and use their delay times to estimate the earthquake depths. The results for basement depth and earthquake depth do agree with the local geology and seismicity. This technique can be used to improve the local structure and earthquake depth estimates. I also propose future work that involves full waveform modelling for each of the earthquakes that will remove assumptions related to the moment tensor of the earthquakes and will lead to a more accurate depth estimates.

Chapter 1

Introduction

The aim and motivation of this dissertation is twofold — first, to constrain the formation history of Oklahoma's crust and second, to aid in developing a better basement fault database for Oklahoma. The 3-D P and S wave velocity model developed in this dissertation is one of the first deep crustal seismic velocity model available for Oklahoma. Seismic velocity models are used to assess the lithology of the crust and are also hugely important for earthquake location estimates. Deep crustal lithology can help us in determining the crustal processes that shaped the present day basement rocks of Oklahoma. Earthquake location estimations from an improved velocity model and novel techniques as presented in the third chapter of this dissertation, will provide a more detailed map of the fault structures in Oklahoma.

1.1 Oklahoma: A Missing Piece in the Precambrian Assemblage of North America

Oklahoma belongs to the Great Plains region of the North America, a vast expanse of plains and grasslands which on the first glance can be geologically

underwhelming but below the surface, Oklahoma hosts a rich geological history. The basement rocks of Oklahoma are part of ∼1.5-1.35 Ga continent building event that gave rise to the the vast midcontinent Southern Granite-Rhyolite province (SGRP) of North America. Following a long period of geologic lull that eroded large swaths of geologic history, the region experienced several periods of eustatic sea level changes starting from the late Cambrian. Late Cambrian, Ordovician, Silurian and Devonian were tectonically quiet and were dominated by widespread deposition of limestones, dolomites, and shales with interspersed layers of sandstone. Crustal unrest during the Late Mississippian with rapid subsidence resulted in deposition of thick shale and limestone sequences in southern Oklahoma. This was followed by intense deformation during the Pennsylvanian subperiod when rapid basin subsidence and orogeny in the south occurred. These deformations are associated with the Ancestral Rockies orogenesis and are responsible for the present day tectonic configuration of Oklahoma. Shales interspersed with sandstones and limestones are the dominant Pennsylvanian rocks found in Oklahoma. Rocks from this period are the dominant reservoir rocks in Oklahoma.

While the sedimentary rocks have been extensively studied as they form the basis of the oil and gas industry in the region, there is relatively little information available regarding the Precambrian rocks that form the basement of Oklahoma. Most of the information available regarding the nature of these rocks are derived from drill cuttings of the upper most part of the basement (Denison, 1981; Nelson and DePaolo, 1985; Bickford and Lewis, 1979; Bickford et al., 1981; Muehlberger et al., 1967). Through geochemical and petrographic analysis of the basement rocks of Oklahoma and surrounding regions, several models of the formation of the rocks of the Southern Granite-Rhyolite province (SGRP) have been presented. Several authors propose an anorogenic origin

due to the presence of coeval A-type plutons. Many authors argue for an extensional settings for the origin of these rocks while others for a convergent and transpressional settings for these rocks. Some of the recent studies suggest that the midcontinent granite-rhyolite rocks were formed from basaltic underplating and crustal melting. Deep crustal seismic velocity models and Poisson's ratio estimates can provide evidence of processes that led to the formation of the SGRP. I use the local seismicity in Oklahoma to derive deep crustal P and S wave velocity models and Poisson's ratio estimates to characterize the deeper crustal rocks in Oklahoma and begin to address some of the bigger questions regarding the evolution and formation of the North American midcontinent.

1.2 Seismicity in Oklahoma

The 1966 Rangely, Colorado induced seismicity experiment led to the discovery of anthropogenic influence on local seismicity through fluid injection in the subsurface (Raleigh et al., 1976). Four decades later, Oklahoma had the perfect conditions for a similar but unintended seismic experiment. The result was a natural laboratory that provided geoscientists with access to observing large-scale geodynamic processes and increased our understanding of intraplate seismicity.

The oil and gas industry has been a part of Oklahoma's history for more than a century. Once a top producer for the United States, the production in Oklahoma declined in the latter half of the 20^{th} century. In the last decade, advancement in oil recovery techniques lead to an increase in oil and gas production. The huge boom in production activities was accompanied by an increase in wastewater produced during these processes which was injected back

into deeper sedimentary formations. The high rate and volume of waste water injection resulted in an exponential rise in seismicity starting from 2009 and achieving peak seismicity rates between 2014-2016 (Ellsworth, 2013; Keranen et al., 2013, 2014; Weingarten et al., 2015; Keranen and Weingarten, 2018), with more or less all of the earthquakes originating in the shallow basement. The rate of induced seismicity has since declined as the waste-water injection rate was reduced as part of efforts to mitigate the seismicity and related hazard in the region. Even with an overall reduced rate of injection, Oklahoma experienced one of the largest earthquake at Pawnee in 2016 with Mw 5.8 which underscores the need to better understand the basement structure of Oklahoma.

The induced earthquakes reactivated several dormant, unmapped faults in Oklahoma. Most of the earthquakes in Oklahoma occurred in basement rooted unmapped faults (Qin et al., 2018). The earthquake locations in Oklahoma showed previously unmapped fault structures in the shallow crust emphasizing the need to perform seismic imaging of the basement to characterize these structures. A comprehensive fault map was developed by Marsh and Holland (2016). They created the fault database by compiling fault maps from published literature, and geologic interpretations from data collected by the oil and gas industry in the region. These data however mostly comprised of faults mapped in the sedimentary layers. Researchers have used aeromagnetic data (Shah and Keller, 2017) and earthquake clustering (Schoenball et al., 2018; Qin et al., 2019) to identify basement faults and add to the fault database for Oklahoma. The fault locations are important when assessing the local seismic hazard and to regulate waste-water injection in the region. Several studies have also analyzed the ambient stress field, the state of stress for faults in Oklahoma, and how the stress changes are caused by varying injection rates

(Darold et al., 2015; Barbour et al., 2017; Walsh and Zoback, 2015; Schoenball et al., 2018; Qin et al., 2018).

Local and regional seismic velocity models are required to obtain accurate earthquake location estimates which forms the basis of most of the earthquake hazard studies. The rise in seismicity along with increased seismic monitoring has provided an extensive passive seismic dataset for Oklahoma. Local seismicity is useful to perform local earthquake tomography, but earthquakes in Oklahoma are very shallow and thus results in shallow upper crustal velocity models. A few studies have utilized the seismicity to developed low resolution upper crustal velocity models for Oklahoma (Chen, 2016; Toth, 2014; Pei et al., 2018) but due to lower resolution and/or limited extent of the models, deeper crustal features are not highlighted. I make use of the extensive passive seismic dataset available for central Oklahoma and apply active seismic processing techniques to develop 3-D P- and S-wave velocity models for Oklahoma that highlight the regional crustal features. Another major problem with earthquake location is the uncertainty in vertical location estimates. In Oklahoma for some local earthquake records shallow crustal reverberation and phase changes are observed. I perform forward travel time modelling to understand the origin of the phase changes and further perform waveform modelling to model the time delays between phases to further enhance the earthquake depth locations.

1.3 Structure of the Dissertation

I present my work in three chapters, one of which is reformatted from a published paper and two are in preparation for submission. The chapters are summarized below:

- Chapter 2: provides detailed methodology that I have used to process the passive seismic data. It focuses on the description and interpretation of a 3-D P-wave velocity model for central Oklahoma. In addition to this, it also provides a summary of geologic and geophysical studies relevant to understanding the Precambrian basement rocks of Oklahoma.

- Chapter 3: focuses on the interpretation of a 3-D S-wave velocity model and Poisson's ratio estimates derived for central Oklahoma.

- Chapter 4: focuses on the travel time and waveform modeling of local seismic waveforms from Cushing to obtain better estimates of vertical earthquake location.

- Chapter 5: summarizes the major results and proposes future research.

Bibliography

Barbour, A. J., Norbeck, J. H., and Rubinstein, J. L. (2017). The effects of varying injection rates in osage county, oklahoma, on the 2016 m w 5.8 pawnee earthquake. *Seismological Research Letters*, 88(4):1040–1053.

Bickford, M. E., Harrower, K. L., Hoppe, W. J., Nelson, B. K., Nusbaum, R. L., and Thomas, J. J. (1981). Rb-Sr and U-Pb geochronology and distribution of rock types in the Precambrian basement of Missouri and Kansas. *Geological Society of America Bulletin*, 92:323–341.

Bickford, M. E. and Lewis, R. D. (1979). U-Pb geochronology of exposed basement rocks in Oklahoma. *Geological Society of America Bulletin*, 90(6):540.

Chen, C. (2016). *Comprehensive analysis of Oklahoma earthquakes: from earthquake monitoring to 3D tomography and relocation.* PhD thesis, University of Oklahoma.

Darold, A. P., Holland, A. A., Jennifer, K., and Gibson, A. R. (2015). Oklahoma Earthquake Summary Report 2014. Technical report.

Denison, R. E. (1981). Basement Rocks In Northeastern Oklahoma.

Ellsworth, W. L. (2013). Injection-Induced Earthquakes. *Science*, 341(6142):1225942–1225942.

Keranen, K. M., Savage, H. M., Abers, G. A., and Cochran, E. S. (2013). Potentially induced earthquakes in oklahoma, usa: Links between wastewater injection and the 2011 mw 5.7 earthquake sequence. *Geology*, 41(6):699–702.

Keranen, K. M. and Weingarten, M. (2018). Induced Seismicity. *Annual Review of Earth and Planetary Sciences*, 46(1):149–174.

Keranen, K. M., Weingarten, M., Abers, G. A., Bekins, B. A., and Ge, S. (2014). Sharp increase in central Oklahoma seismicity since 2008 induced by massive wastewater injection. *Science*, 345(6195):448–451.

Marsh, S. and Holland, A. (2016). Comprehensive fault database and interpretive fault map of oklahoma. *Oklahoma Geol. Surv. Open-File Rep. OF2-2016, Oklahoma Geological Survey, Norman, OK.*

Muehlberger, W. R., Denison, R. E., and Lidiak, E. G. (1967). Basement Rocks in Continental Interior of United States. *AAPG Bulletin*, 51(12):2351–2380.

Nelson, B. K. and DePaolo, D. J. (1985). Rapid production of continental crust 1.7 to 1.9 b.y. ago: Nd isotopic evidence from the basement of the North American mid-continent. *Geological Society of America Bulletin*, 96(6):746.

Pei, S., Peng, Z., and Chen, X. (2018). Locations of Injection-Induced Earthquakes in Oklahoma Controlled by Crustal Structures. *Journal of Geophysical Research: Solid Earth*, 123(3):2332–2344.

Qin, Y., Chen, X., Carpenter, B. M., and Kolawole, F. (2018). Coulomb Stress Transfer Influences Fault Reactivation in Areas of Wastewater Injection. *Geophysical Research Letters*, 45(20):059–11.

Qin, Y., Chen, X., Walter, J. I., Haffener, J., Trugman, D. T., Carpenter, B. M., Weingarten, M., and Kolawole, F. (2019). Deciphering the Stress State of Seismogenic Faults in Oklahoma and Southern Kansas Based on an Improved Stress Map. *Journal of Geophysical Research: Solid Earth*, 124(12):12920–12934.

Raleigh, C., Healy, J., and Bredehoeft, J. (1976). An experiment in earthquake control at rangely, colorado. *Science*, 191(4233):1230–1237.

Schoenball, M., Walsh, F. R., Weingarten, M., and Ellsworth, W. L. (2018). How faults wake up: The Guthrie-Langston, Oklahoma earthquakes. *The Leading Edge*, 37(2):100–106.

Shah, A. K. and Keller, G. R. (2017). Geologic influence on induced seismicity: Constraints from potential field data in Oklahoma. *Geophysical Research Letters*, 44(1):152–161.

Toth, C. R. (2014). *Separation of the Earthquake Tomography Inverse Problem to Refine Hypocenter Locations and Tomographic Models: A Case Study from Central Oklahoma*. PhD thesis, University of Oklahoma.

Walsh, F. R. and Zoback, M. D. (2015). Oklahoma's recent earthquakes and saltwater disposal. *Science Advances*, 1(5):e1500195.

Weingarten, M., Ge, S., Godt, J. W., Bekins, B. A., and Rubinstein, J. L. (2015). High-rate injection is associated with the increase in u.s. mid-continent seismicity. *Science*, 348(6241):1336–1340.

Chapter 2

Imaging the deep crustal structure of central Oklahoma using stacking and inversion of local earthquake waveforms

2.1 Abstract

The southern Granite-Rhyolite province contains a comprehensive record of lithospheric evolution in North America. During the last decade, increased seismicity along with improved seismic monitoring in Oklahoma provided a rich catalog of local earthquakes. The source-receiver geometry of this dataset is well posed to illuminate the middle and lower crust through long-offset recordings of the Pg phase. We present a 3-D P-wave velocity model for central and northern Oklahoma developed through a non-standard processing scheme applied to local earthquake waveforms recorded from 2010-2017, focusing on the deeper crust. We employed common-mid-point sorting, stacking, and inversion of Pg-phases which resulted in a set of localized velocity-depth functions up to depths of 40 km. Using this methodology, we significantly

increased the S/N ratio for far offset (∼200 km) local earthquake waveforms which led to the increase in depth of investigation in the final 3-D velocity model. We find high velocity (> 7 km/s) lower crust throughout the investigated area which suggests a mafic lower crust. The high velocities support previously established models which state that the lower crust of the Southern Granite-Rhyolite province was derived from melting of older crust. We further relate shallow and middle crustal velocity anomalies to other data sets such as gravimetric and magnetic anomalies, and the spatial distribution of earthquakes. We do not find clear evidence for the existence of the Midcontinent Rift (MCR) in northern Oklahoma.

2.2 Introduction

The study of Precambrian rocks in the midcontinent region (Figure 2.1) of North America is crucial in understanding the Proterozoic evolution of the North American continental lithosphere. Due to the limited exposures of the Precambrian crystalline rocks in the midcontinent region, most studies have used cores and drill cuttings to study the Precambrian geology in this region. In Oklahoma, the Precambrian basement is covered by Phanerozoic sediments except for a small area in Spavinaw, OK in the northeast and in the eastern Arbuckle mountains in the southeast.

Some of the early petrological and geochronological studies of the Precambrian basement rocks laid the groundwork for investigating the continental evolution in the midcontinent region (Bickford and Lewis, 1979; Bickford et al., 1981, 1986; Denison et al., 1984; Lidiak, 1996; Muehlberger et al., 1966, 1967; Nelson and DePaolo, 1985). U-Pb zircon geochronological studies from outcrop and drill cuttings established the age of these rocks to be about 1.4-1.34 Ga

in the southern midcontinent (Bickford et al., 1981; Muehlberger et al., 1967). Nelson and DePaolo (1985) differentiated the rocks in the Southern and Eastern Granite-Rhyolite provinces based on Sm-Nd isotopic studies. Their "Nd-line" defines an isotopic boundary that divides the granite-rhyolite provinces based on the model ages, where rocks in the northwestern part are derived from older cratonic rocks (1.8-1.6 Ga) while rocks in the southeast of the Nd-line are derived from juvenile rocks (1.5-1.3 Ga) (Figure 2.1). Denison et al. (1984) used petrographic analysis to further divide the Precambrian basement rocks in northeastern Oklahoma. These early studies were instrumental in establishing the ages and extent of the Southern and Eastern Granite-Rhyolite provinces in midcontinent but are based on outcrop and drill cuttings and are therefore unable to describe the nature of the lower crustal rocks. Lack of coeval xenoliths in the midcontinent region has further contributed to our lack of knowledge of the deeper crust in this region. Figure 2.1 shows the major tectonic provinces and crustal features in the midcontinent region.

While the early studies were able to establish the vast extent of the Granite-Rhyolite provinces, its origin has been debated for decades. Presence of A-type plutons further adds to the enigma of its origin (Anderson and Bender, 1989; Bickford et al., 2015; Denison et al., 1984). Based on the studies of these plutons and rocks from the Granite-Rhyolite provinces, several theories including extensional anorogenic settings, back-arc magmatism related to early Grenville orogeny, and back-arc and intracontinental magmatism related to accretionary tectonism in Laurentia $\sim$1.6-1.3 Ga, have been considered (Amato et al., 2011; Anderson and Bender, 1989; Whitmeyer and Karlstrom, 2007). Recent Lu-Hf studies by Bickford et al. (2015) provide a new model for the formation of the granite-rhyolite province of the midcontinent. Their isotope data corroborates the presence of the Nd-line as given by Nelson and DePaolo

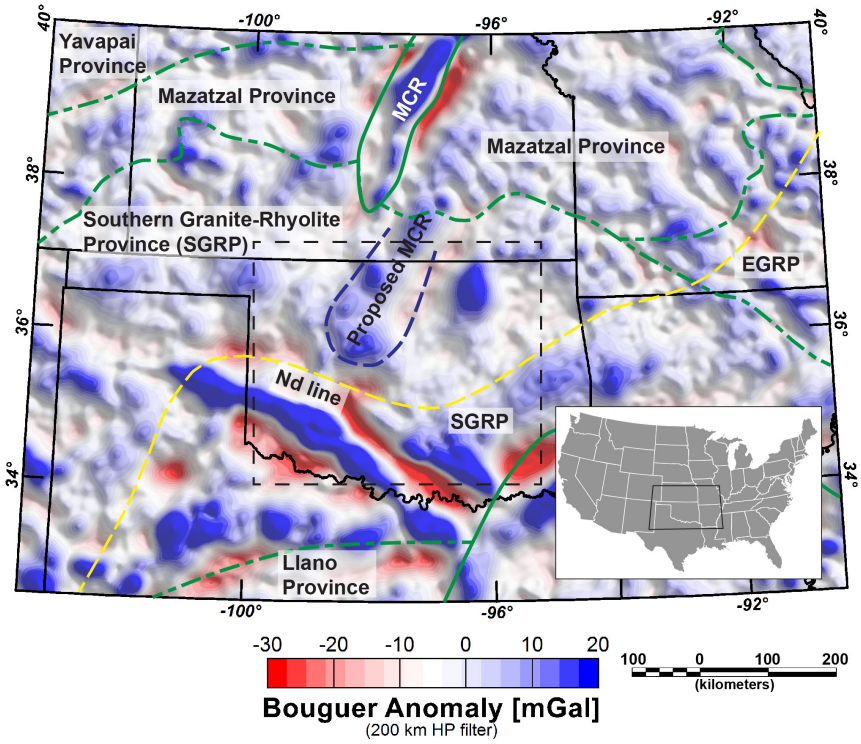


Figure 2.1: Tectonic provinces in the central part of the midcontinent (Modified from Bickford et al. (2015)). Bouguer gravity anomalies (based on Decade of North American Geology (DNAG) data) are shown after applying a 200 km high-pass wavelength filter to suppress upper mantle features. A possible continuation of the Midcontinent Rift (MCR) in Oklahoma is shown as proposed by previous studies. [EGRP: Eastern Granite-Rhyolite province]. Study area shown in black dashed box.

(1985). They suggest basaltic underplating as part of the mechanism that led to the melting of lower crustal rocks that intruded to form the granite-rhyolite provinces. Basaltic underplating is inferred from high velocity lower crust (P-wave velocity 6.9-7.5 km/s), in deep crustal seismic models in other parts of the world (Karlstrom et al., 2005; Thybo and Artemieva, 2013). However, deep crustal seismic imaging with sufficient vertical and horizontal resolution is scarce in the Southern Granite-Rhyolite province.

Another intriguing feature in the midcontinent is the ∼3000 km long Midcontinent Rift (MCR), a failed rift that formed ca. 1.1 Ga within Laurentia (Hinze et al., 1997; Van Schmus and Hinze, 1985). During the ∼20-40 Myr

rifting event, vast amounts of igneous rocks and later sedimentary rocks were deposited within the rift zone. The signature of the MCR is observed as a high gravity anomaly stretching from the Great Lakes to central Kansas (Hinze et al., 1997; Sims et al., 2005; Van Schmus and Hinze, 1985). Several authors extend the MCR into north central Oklahoma based on relatively high gravity anomalies that they interpret to continue from the gravity anomalies observed in the north (Kolawole et al., 2020; Stein et al., 2014, 2015) (Figure 2.1). Unlike modern rifts, where crustal thinning due to extension is observed (Thybo and Artemieva, 2013), crustal thickening is observed for the northern part of the MCR (Chichester et al., 2018; Hinze et al., 1997; Shen et al., 2013; Zhang et al., 2016). Increased crustal thickness is attributed to a compressive event that inverted the rift, after it had already failed (Stein et al., 2015, 2018a). Studies by Chichester et al. (2018) and Zhang et al. (2016) were conducted in the northern part of the MCR. There is evidence for underplating beneath the MCR in certain regions (Chichester et al., 2018; Woelk and Hinze, 1991; Zhang et al., 2016). Surface evidence for the rift is not observed in Oklahoma, and so deep crustal studies that reveal the seismic structure can inform about the presence or absence of the rift feature in Oklahoma.

Despite emphasis on seismic studies for hydrocarbon exploration in its sedimentary basins, Oklahoma is significantly under-explored by means of deep crustal-scale seismic imaging campaigns. Consequently, knowledge of the deep crustal structure is limited and constrained to a few locations only. The recent increase in induced seismicity due to oil and gas production (Ellsworth, 2013; Keranen et al., 2014) and the subsequent efforts in instrumentation to monitor this activity, which also coincided with the ongoing deployment of US Transportable Array across United States, resulted in a large-scale, albeit unintentional, seismic experiment. In our study, we make use of local earthquake

data recorded across 10 networks between 2010-2017 to develop a 3-D P-wave velocity model of the crust for central Oklahoma, a core part of the Precambrian midcontinent crust. As the station coverage and earthquake distribution resembles an irregular 3-D active seismic experiment, we employ active seismic processing techniques such as common mid-point sorting and stacking. This improves the signal-to-noise ratio and simplifies the wavefields of the recorded data, allowing for imaging deeper structures and large areas. Our study aims to contribute to understanding the evolution of this understudied part of the midcontinent crust. Furthermore, we suggest a workflow for processing local earthquake data which is potentially applicable to other areas as well. In this paper we present and discuss our methodology and geologic and tectonic implications from our derived 3-D seismic model.

2.3 Regional Geology and Previous Geophysical Studies

2.3.1 Geology

The evolution of Laurentia through a periodic and continued accretion of igneous material from volcanic and island arcs over the Archean cratons, is the most widely accepted model for the formation of the lithosphere in the continental United States (Whitmeyer and Karlstrom, 2007). The Mazatzal Orogeny ca. 1.65-1.6 Ga resulted in the accretion of juvenile volcanic arcs forming the older crustal rocks in Oklahoma (Whitmeyer and Karlstrom, 2007). Although the southern extent of the Mazatzal province has not been mapped, isotopic evidence by Nelson and DePaolo (1985) and core and outcrop evidence from surrounding states of New Mexico and Kansas suggest an extension of

this province beneath the Southern Granite-Rhyolite province of Oklahoma (Anderson and Bender, 1989; Whitmeyer and Karlstrom, 2007).

The Mazatzal orogeny was followed by the accretion of the Southern Granite Rhyolite province (SGRP) ca. 1.5-1.35 Ga. The Sm-Nd isotopic study by Nelson and DePaolo (1985) provided a major breakthrough in understanding the origins of SGRP. Their studies lead to the conclusion that these rocks were derived from older crustal rocks. This study was further supported by Van Schmus et al. (1996) who calculated Sm-Nd model ages showing the Mesoproterozoic rocks of SGRP with a consistent increase in age moving from southeast to northwest. The tectonic setting of the SGRP and the coeval A-type plutons have been studied and evaluated by various workers. Whitmeyer and Karlstrom (2007) suggest a convergent and transpressional setting wherein the emplacement of the Granite-Rhyolite province was caused by a tectonic episode away from the plate margins. Amato et al. (2011) suggest an extensional or transpressional setting for the Granite-Rhyolite terrane based on their studies of granitic plutons in Burro Mountain, New Mexico, which are coeval with the basement rocks of Oklahoma. Studies based on A-type plutons indicate an anorogenic origin, suggesting the source of these plutons as partial melting of juvenile crust (Anderson and Bender, 1989). A recent study by Bickford et al. (2015) presents new geochronological and isotopic data for samples across the mid-continent region of the United States, revealing that continental scale magmatism was long lived (150-200 Ma) and locally episodic as given by the bimodal zircon age distribution in the midcontinent. Lack of zircon in many samples analyzed by Bickford et al. (2015), along with magma temperatures derived from the existing zircon samples suggest magma temperatures above 850 °C. Similarly, Goodge and Vervoort (2006) analyzed Hf isotope compositions in the zircons in samples from the Penokean (1.9-1.8

Ga), Mojave (1.8-1.7 Ga), Yavapai (1.8-1.7 Ga), and Granite-Rhyolite (1.5-1.3 Ga) provinces. Studies of A-type plutons also suggest their formation from partial melting of tholeiitic magma (Frost and Frost, 2011, 2013; Shaw et al., 2005). Bickford et al. (2015) suggest a convergent plate boundary model at the northeastern margins of Laurentia that led to the creation of back arcs in the continental interior. They argue that the convergent active margin can lead to destabilization of the back arcs. This can cause delamination of the lithosphere, consequently leading to a shallower lithosphere-asthenosphere boundary and higher temperatures at shallower depths which may induce crustal melting. This model seems to agree with the models suggested by Karlstrom et al. (2001), Slagstad et al. (2009), and Whitmeyer and Karlstrom (2007).

The Precambrian accretion of the lithosphere was followed by opening of the Iapetus Ocean in late-Neoproterozoic - early-Cambrian and the formation of the Southern Oklahoma Aulacogen (SOA) (Gilbert et al., 1993; Buckey, 2012; Thomas, 1991; Whitmeyer and Karlstrom, 2007). The SOA comprises the Wichita uplift, the Arbuckle uplift and the Anadarko basin. The evolution of these structures continued through the Cambrian through continued subsidence, deposition, erosion, and intrusion of igneous rocks (Keller et al., 1983). Finally, intense deformation and erosion during the Pennsylvanian associated with the Ancestral Rockies orogeny led to the present-day configuration of the tectonic features including the Nemaha Uplift (Figure 2.2) (Garner and Turcotte, 1984; Gilbert et al., 1993; Johnson, 2008).

2.3.2 Previous Seismic Studies

Tryggvason and Qualls (1967) derived a simple layered model for Oklahoma's crust through a 2-D active seismic refraction study. The ∼450 km profile runs northeast-southwest across Oklahoma, cutting through different

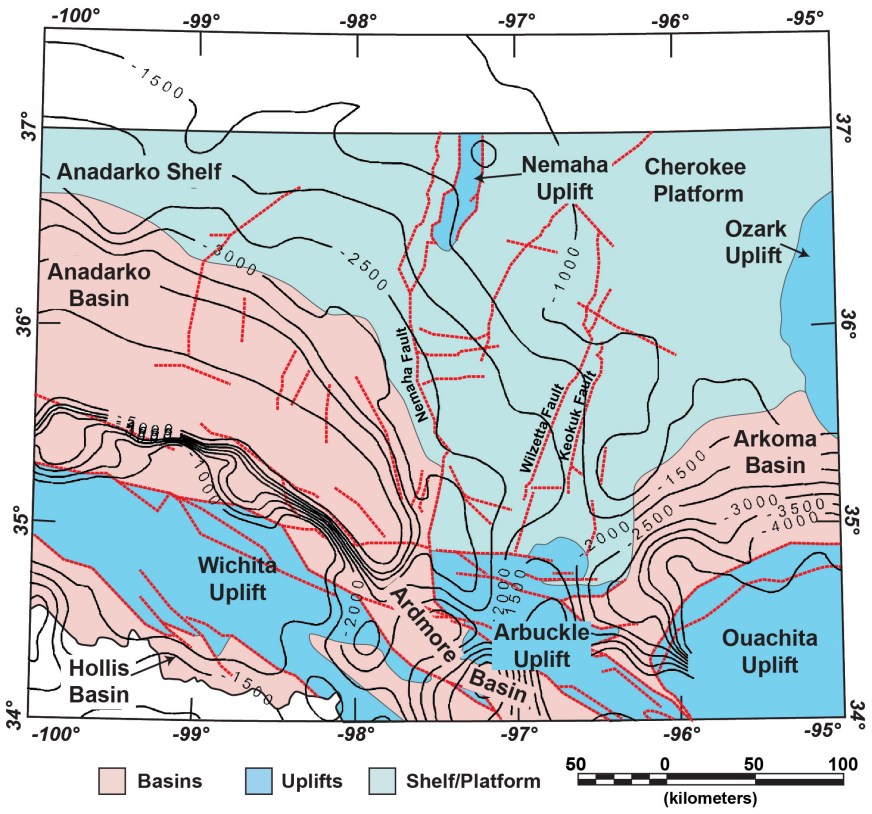


Figure 2.2: Major tectonic features in Oklahoma (adapted from Northcutt and Campbell (1996)). Red dashed lines: major fault systems. Black solid lines: depth-to-basement contours (meters) computed from basement well information as given by (Campbell and Weber, 2006). Areas beyond the state of Oklahoma are in white.

tectonic units (Figure 2.3). Based on recordings of multiple shots from two locations (Chelsea in NE and Manitou in SW) at 26 seismometers, they interpreted a homogeneous three-layer crustal model and provided depth of Moho and crustal velocity variations in Oklahoma. The same 2D line was re-processed and integrated with other datasets by Mitchell and Landisman (1970) who derived a more detailed cross-section. They used seismic refraction and reflections observed from the Tryggvason and Qualls (1967) - 2D profile, gravity anomaly data, basement depth data, and well-log data. Their final velocity model showed homogeneous crustal layers below an upper crust of 18 km thickness. They modelled the shallow upper crust in much greater detail as

compared to the earlier model and observed discontinuities related to known fault zones. Crustal thickness is interpreted to be 46 km with lower crustal P-wave velocities up to 7.39 km/s.

In the late 1970s, deep seismic reflection profiles were acquired by the Consortium for Continental Reflection Profiling (COCORP), as well as a 2-D wide angle reflection/refraction survey by University of Texas at El-Paso (UTEP) and University of Texas at Dallas (UTD) in 1985. Both of these surveys aimed to understand the deeper structure of Wichita Uplift and characterize structural features at the boundary of Southern Oklahoma Aulacogen and the Anadarko Basin. Several authors worked on developing a 2D velocity structure across Wichita uplift and Anadarko basin using these data (e.g. Agena et al., 1989; Brewer et al., 1983, 1984; Brewer and Oliver, 1980; Phinney and Jurdy, 1979; Zhu and McMechan, 1989, and others.). These investigations revealed a layered basement about 12 km thick and a thick crust with depth to Moho varying from 40-45 km (Lynn et al., 1981; Pratt et al., 1992). The UTEP-UTD seismic survey was reanalyzed by Buckey (2012), who obtained a more detailed velocity and geologic model for the upper - mid crust up to 20 km depth. Figure 2.3 shows the locations of the deep seismic sounding surveys in Oklahoma.

There have been a few passive seismic studies targeting large scale crustal structure in Oklahoma. Local earthquake tomography by Chen (2016) and Toth (2014) obtained upper crustal (up to 15-20 km) seismic P- and S-wave velocity distribution. Velocity anomalies observed in these models show close correlation to the major tectonic features like the Nemaha Fault Zone and the Wilzetta Fault Zone in Oklahoma. A high resolution but shallow anisotropic Pg velocity was developed for central Oklahoma by Pei et al. (2018). Receiver function analysis and Pn tomography by Tave (2013) using the data

from US Transportable Array network revealed Moho between 36 km and 42 km throughout the state. McGlannan and Gilbert (2016) reported a crustal depth variation from 30-55 km across Oklahoma based on the the Earthscope Automated Receiver Survey using the US Transportable Array. In general, these passive seismic studies either do not have the necessary depth of investigation to image the deeper crustal structures (Chen, 2016; Toth, 2014), lack the resolution required to be able to comment on the regional crustal structure (Evanzia et al., 2014; McGlannan and Gilbert, 2016), or provide shear wave velocities only based on ambient noise tomography (Shen and Ritzwoller, 2016; Zhu, 2018). Likewise, gravity and magnetic data can provide some information on the crust (Bickford et al., 1986; Van Schmus et al., 1996; Sims et al., 2005), but non-uniqueness of these methods require constraints such as seismic data to infer robust interpretations. The lack of rock samples from deeper crust in Oklahoma further limits our understanding of this part of the crust.

Our approach aims to address these issues and obtain a robust, deep-reaching P-wave velocity model that can highlight the regional crustal features in central Oklahoma.

2.4 Data and Methodology

Local earthquakes are commonly used for imaging in seismically active regions. Local earthquake tomography (LET) uses travel times of Pg and Sg earthquake phases to invert for the velocity structure, while often simultaneously (re-)locating the earthquake source (e.g., Thurber, 1993; Kissling et al., 1994; Eberhart-Phillips and Michael, 1998; Rawlinson and Sambridge, 2003). The term 'local' refers to a spatial overlap between sources and receivers, e.g. the receiver array should enable the recording of crossing rays at all incidence

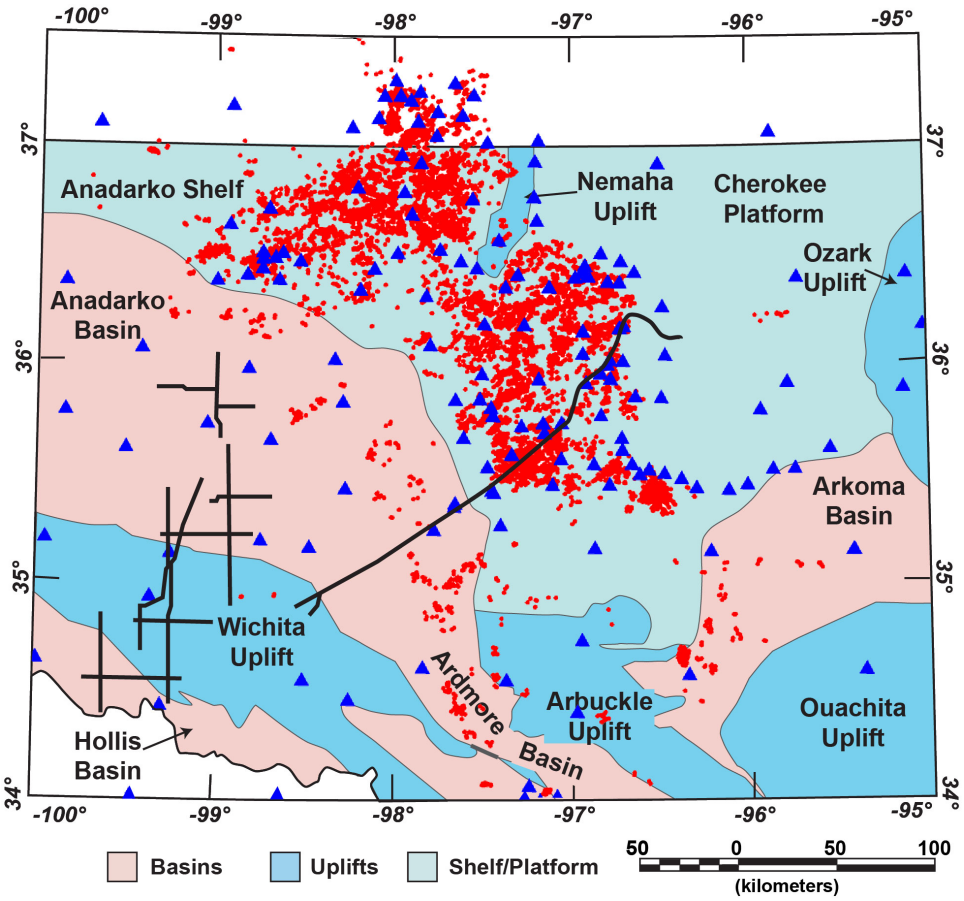


Figure 2.3: Black thick lines: previous active seismic studies conducted in Oklahoma for crustal investigations. Red dots: location of earthquakes used in this study. Blue triangles: recording stations used in this study. Areas beyond the state of Oklahoma are in white.

angles, and therefore allow for a tomographic inversion for both velocity structure and hypocenters.

Earthquake depths play a crucial role for the depth of investigation in LET. For a given velocity gradient, waves from shallow earthquakes recorded at large offsets reveal information from the deeper crust, while deep earthquakes can record deep crustal information at short offsets due to their sub-vertical ray paths (Braeuer et al., 2012; Tong et al., 2017). The signal-to-noise (S/N) ratio also decreases with offset (source-receiver distance) which ultimately leads to a lower depth of investigation when using only shallow earthquakes. The

traditional LET approach involves identifying and picking Pg and Sg seismic phases across different stations. Sparse distribution of recording stations is common in passive seismic network geometries and makes correct phase correlation and identification difficult. Estimating robust travel times at large offsets is challenging, particularly for small magnitude events. Consequently, traditional LET methods in Oklahoma where the earthquake depths are shallow (∼2-7 km depth, Figure S2.14) can only represent velocity variations in the upper crust (Chen, 2016; Toth, 2014). Correlation and correct interpretation of individual travel times requires high quality data, and in the case of many observations, (semi-)automated phase correlation and picking routines (Chen, 2016; Thybo et al., 2006).

To overcome the issues of low S/N ratio and uncertainties in phase correlations, we propose to stack waveforms and apply specifically designed processing and inversion routines. This approach has been successfully applied to active source 3-D wide-angle refraction/reflection data as well as to earthquake sources for both P- and S-wavefields (Behm et al., 2007; Behm, 2009; Buehler and Shearer, 2013; Loidl et al., 2014). We use existing localizations of the events (Schoenball and Ellsworth, 2017) and consider the data set as an active 3-D acquisition with irregular geometry. Using the principle of reciprocity, the small number of recording stations is compensated by a large number of events. We aim for stacking and inversion of Pg (refractions from the crust) phases to derive a 3-D P-wave velocity model of the crust. Stacking is preceded by sorting to common-mid-point (CMP) gathers, as wide-angle refractions best approximate the seismic structure at the common-midpoint location where the ray travels horizontally. Pre-stack processing aims at enhancing and simplifying the wavelets such that the under-sampled wavefields can stack constructively. Stacking has a tendency to favor robust models, i.e.

it has the natural property of being less sensitive to randomly distributed data outliers (Behm et al., 2007). CMP regionalization leads to a set of local 1-D travel time curves approximating the crustal structure at the CMP location. Those travel time curves are picked and inverted, and the derived set of local 1-D velocity models is eventually combined into a smooth 3-D Pg velocity field.

2.4.1 Data

We use 27,568 local earthquakes recorded at 165 broadband stations belonging to 6 different networks across Oklahoma (Figure 2.3). The earthquake events were recorded between the time period January 2010 to September 2017. We use a catalogue which combines relocation from Schoenball and Ellsworth (2017) and a HypoDD corrected catalogue (pers. comm. with Dr. Jefferson Chang). Hypocenter solutions (including origin time) in those catalogs are associated with uncertainties, which will be addressed in section 2.4.2.4 Earthquake depths vary from 2-7 km (Figure S2.14) and we select the maximum epicentral distance for P-wave velocity evaluation to be 250 km. Finally, we have 1,214,112 individual vertical component seismic traces that are used for further processing.

2.4.2 Pg Processing

The workflow to derive a 3-D crustal P-wave velocity from the Pg phase comprises six steps:

1. Geometric and kinematic corrections to account for varying source depths and sedimentary thickness at the receiver locations.

2. Pre-stack signal processing to increase the S/N ratio and to facilitate

constructive interference.

3. CMP sorting and stacking in offset bins to derive local 1-D travel time curves.

4. Manual picking of the 1-D travel time curves.

5. Inversion of 1-D picked travel time curves for local 1-D velocity-depth functions representing the CMP location.

6. Combination of all 1-D velocity models into a 3-D velocity model.

2.4.2.1 Geometric and Kinematic Corrections (Datuming)

Time and geometric corrections are required to account for the different earthquake depths and sedimentary thickness at the receiver locations. First, to correct for the elevation difference between source and receiver of each earthquake-receiver pair, we choose the corresponding earthquake depth as datum and apply time and offset corrections to shift the receiver to this datum. Second, stacking of different source-receiver pairs requires all data to be at the same reference level. We choose a depth of 5 km as our final datum since most of the earthquakes in Oklahoma are within the ∼5-7 km depth range (Figure S2.14). This introduces further time corrections and offset shifts for both the source and receiver locations.

Datum corrections for wide-angle refractions depend on the earthquake depth, source-receiver offset, basement structure at source and receiver, and the regional velocity structure. As opposed to simple static corrections for steep-angle reflections, the combined effects of velocity structure, basin geometry and velocities, and offset dependency introduce a high degree of nonlinearity. Calculation of exact time and geometric corrections would require a

3-D velocity model of the crust, which we do not have at this stage. As an approximation for the purpose of those corrections, we use a 1-D velocity model for the crust below the sediment-basement interface based on the Christensen and Mooney (1995) model for continental shields. A 1-D velocity model for the sedimentary cover above the basement is taken from the OGS velocity model for Oklahoma (Darold et al., 2015). An extrapolated basement depth map calculated from basement penetrating wells and regional gravity data (Campbell and Weber, 2006) is used to derive the basement depths at each source and receiver location. We calculate offset-dependent time and offset corrections for a range of earthquake depths, and basement depths at the earthquake and receiver location using the ray tracing code ANRAY (Gajewski and Pšenčik, 1987; Gajewski and Pšenčík, 1989). Finally, those corrections are interpolated for the actual earthquake and receiver locations for each source-receiver pair. The corrections are largest for shallow offsets and deep earthquakes (Figure S2.15).

2.4.2.2 Pre-stack Signal Processing

We apply a minimum phase Ormsby bandpass filter with corner frequencies of 2-4-6-8 Hz to increase the S/N ratio. To facilitate constructive interference of the Pg phase, we convert the data to their envelope (modulus of the complex trace). Bandpass filtering and envelope calculation also lifts the requirement of instrument response removal. This step is crucial since the receiver spacing is large, and wavelets from different events cannot be expected to be in phase after CMP sorting. We further increase the visibility of the Pg phases, in particular at larger offsets, by applying STA (short-term average) to LTA (long-term average) ratio signal detection (Astiz et al., 1996). The averaging windows used for STA and LTA are 0.1 s and 10 s respectively and have been

decided after testing. These processing steps effectively remove the source signatures and in turn facilitate stacking of waveforms from different earthquakes. Figure 2.4 shows the result of pre-stack signal processing on one event gather.

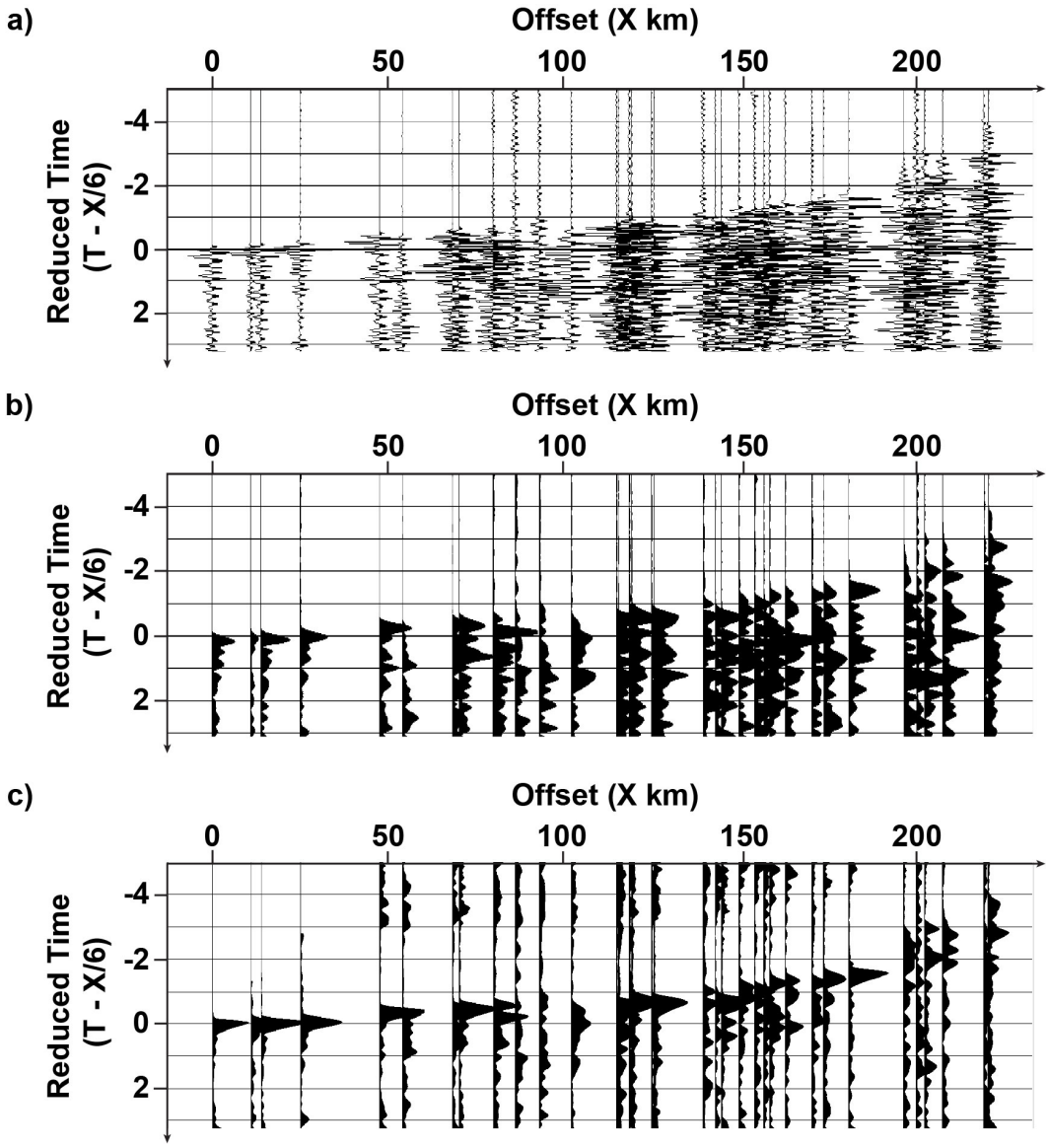


Figure 2.4: Example of preprocessing on one datum-corrected event gather with a linear move-out for a velocity of 6 km/s. a) bandpass filtered (2-4-6-8 Hz), b) signal converted to envelope, c) STA/LTA applied.

2.4.2.3 CMP Sorting and Stacking

The signal-processed traces are sorted into common mid-point (CMP)-gathers and stacked in offset bins. The study area is divided into cells such that the traces whose mid-points (of respective offsets) fall into a particular defined cell, are then sorted into one gather. The offset-sorted Pg phases in this gather represent the travel time curve for the velocity-depth function at the cell location (Behm et al., 2007). Rectangular cells are centered on a regular grid with 10 km lateral spacing, and the cell size is automatically varied between 10-70 km throughout the study area depending on the number of traces which fall into each CMP gather. The variable cell size accounts for the irregular geometry and is smallest in the central part of the study area (Figure 2.5). Due to the sparse receiver geometry, larger cell sizes can be required to collect enough near-offset traces. Figure 2.5(a) provides a measure of (relative) lateral resolution. However, lateral resolution will also vary with depth as large-offset rays travel longer horizontal distances in similar depths. The final location of the cell is calculated as the average location of all the trace mid-point locations in the CMP gather.

In each CMP gather, the traces are subjected to a linear move-out (LMO) correction with a velocity of 6 km/s and are stacked in 5 km offset bins. The absolute offset of each stacked trace is calculated as an average of all traces in the offset-bin. The collection of these stacked traces along their absolute offset is referred to as 'CMP stack' in the subsequent sections. Prior to sorting and stacking, we calculate a relative quality value for each event which depends on source depth and the hypocenter errors in both depth and lateral position. A large quality value is obtained for shallow earthquakes and small errors, and the events are sorted by descending quality value. Sorting and stacking are performed on (1) the first 10% of the events (high-quality data only), (2) the

first 50% of the events (high to medium quality data), and (3) to all events (high to low quality data). Figure 2.6 shows the difference between using a small number of high-quality events vs. a larger number of low-quality events. E.g. non-physical humps in the 1-D travel time curve and overall low S/N ratio are more effectively mitigated in the 50% dataset, which includes earthquakes in the depth range 5 to 7 km. Consequently, we chose this data subset for CMP-sorting and stacking.

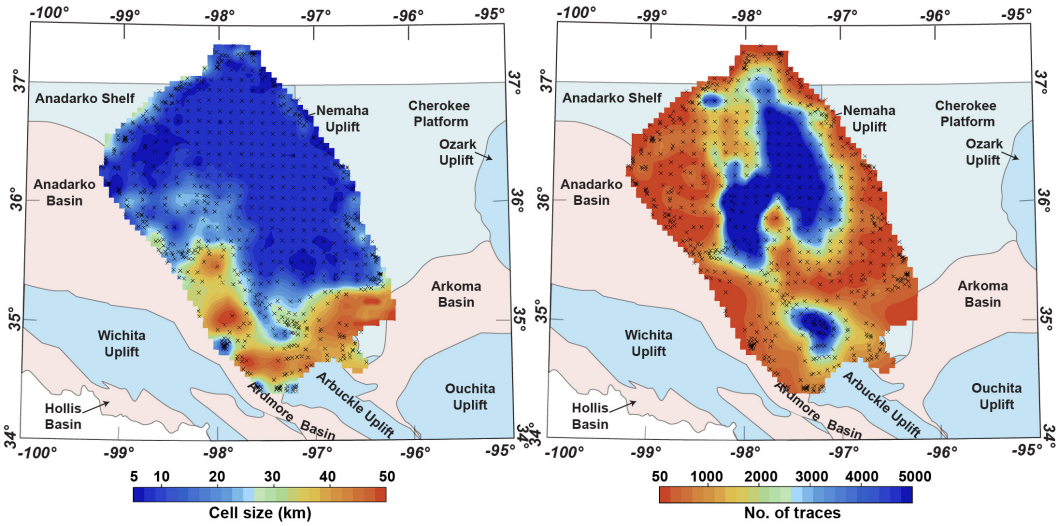


Figure 2.5: Measures of lateral resolution and trace fold for the CMP bins (a) bin size, (b) number of traces in each bin. CMP bin center locations are shown as "x".

2.4.2.4 Travel Time Curve Picking

In traditional local earthquake tomography (LET), accurate travel time picks provide the arrival times for seismic phases and are inverted to determine the subsurface velocity structure. In contrast, we pick 1-D travel time curves instead of arrivals on individual traces. All stacked gathers are band-pass filtered with a 0.04-0.08-0.5-0.8 Hz Ormsby filter prior to picking. The stacked gathers have high S/N ratios but due to the process of envelope cal-

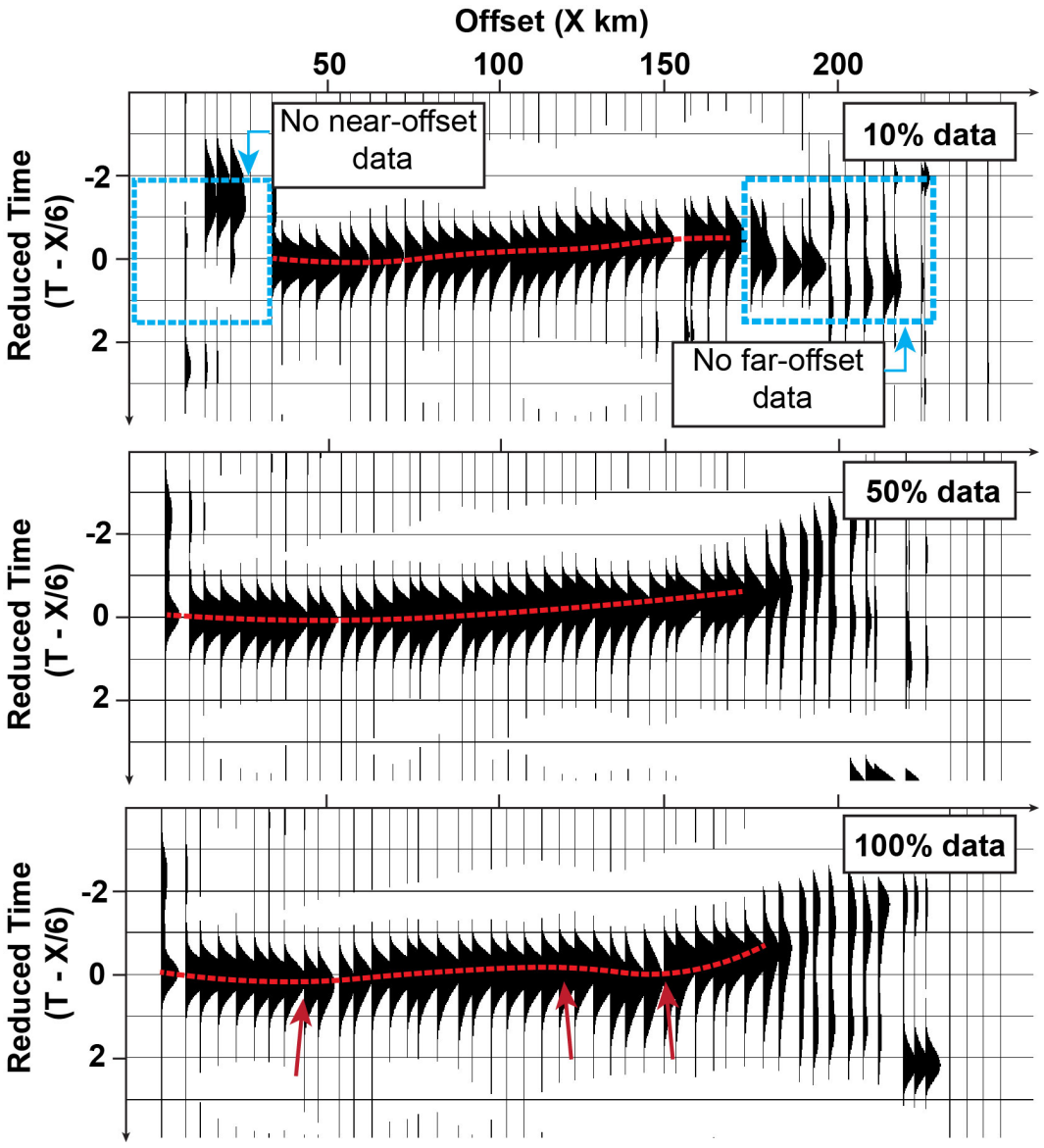


Figure 2.6: Comparison of CMP stacks for 10%, 50%, and 100% data sets (see text for details). Red arrows indicate non-physical deviations from a 1-D travel time curve.

culation, stacking and low-pass filtering, the phase of the waveform is lost. At short offsets, the maximum of the filtered envelope wavelet corresponds to a theoretical travel-time curve based on a 1-D velocity model for continental shields (Christensen and Mooney, 1995) (Figure 2.7). We therefore pick smooth travel time curves along the maximum amplitude of the stacked traces.

A systematic shift of the first arrival phase would not alter the velocity estimation significantly, as the subsequent 1-D inversion is primarily based on the variation of the slope of the 1-D travel time curve. 1-D travel time curves have to represent a simple layer-cake earth model, and as such are more constrained than 3-D travel time curves. This implies that humps or similar irregularities in the travel time curve cannot be picked. Such deviations may be caused by localized gross errors in hypocenter and/or origin time solutions, and we avoid picking such arrivals (Figure 2.7, location 3,4). Continuity and smoothness of the travel-time curve is a requirement for the assumption of a layer-cake earth model, and introduction of irregularities in the curve will not be representative of geologic structures. Finally, we manually inspect our picks for lateral consistency across the CMP gathers and picks are removed and/or corrected if required. We finally obtain 1-D travel time curves representing the velocity-depth function at each CMP location. We only pick CMP stacks with a sufficient number of near-offset traces to ensure a stable inversion. Finally, we manually inspect our picks for lateral consistency across the CMP stacks and picks are removed and/or corrected if required. Overall, we obtain 1-D travel time curves representing the velocity-depth function for 1167 CMP locations. Figure 2.7 shows examples of selected CMP stacks.

2.4.2.5 1-D Travel Time Inversion and Combination into a 3-D Model

The 1-D travel time curve of an individual CMP stack represents a 1-D velocity-depth function at that CMP location. Assuming an initial 1-D velocity model for the crust, the 1-D travel time curves are inverted to obtain the velocity information using a ray parameter weighted scheme (Behm et al., 2007). Our initial velocity model is derived from the shields and platforms ve-

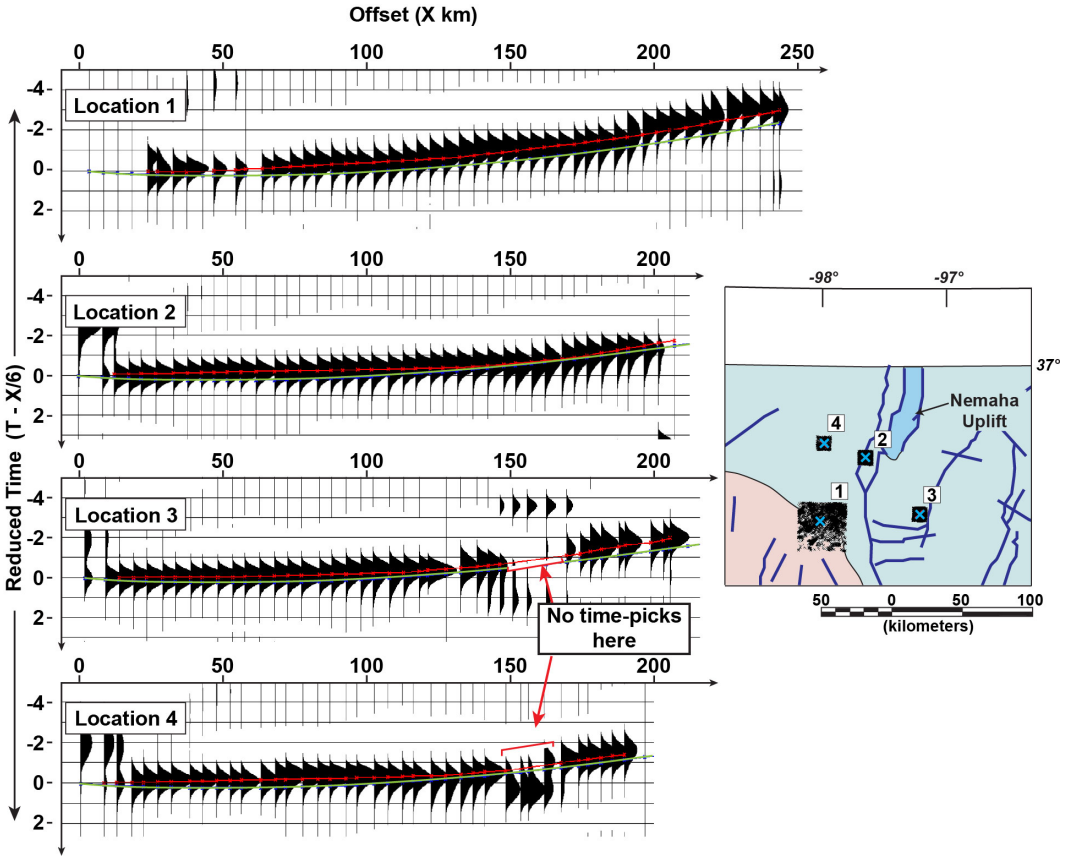


Figure 2.7: Examples of CMP stacks from different locations. The map on the right shows the location and size of the CMP bin for each of the stacked gathers. Small black dots: location of individual trace midpoints within one CMP bin. Blue cross: CMP bin center locations. Red line (on stacks): picked travel times. Green line (on stacks): theoretical travel-time curve based on 1-D velocity model for continental shields.

locity model as given by (Christensen and Mooney, 1995) for the basement and below. The inversion provides a 1-D velocity-depth function at each location along with corresponding resolution elements as the output. The resolution elements define the confidence on each of the final computed velocity elements (Figure S2.16) and vary from 0 (undetermined) to 1 (uniquely determined). It shows that on average the upper and lower crustal velocities are uniquely determined in the 1-D inversion. Lower values are associated with a lack of observed offsets related to that depth range, and are more prominent in depths

between 15 and 25 km. We also test the dependency of the inversion on different initial velocity models (Figure S2.17) and compare the travel time residuals before and after the inversion (initial model vs. final model, Figure S2.18). Overall, it shows that there is negligible influence of the initial model as a 5-15% perturbation in initial velocity model resulted in deviations of only about +/- 0.2% for the final inverted velocities. The RMS travel time residuals were also significantly reduced from a range of ∼0.004 s - ∼0.5 s with a mean of ∼0.18 s for the initial model to a range of ∼0.001 s -∼0.04 s with a mean of ∼0.01 s for the final model (Figure S2.18). The entire workflow (CMP sorting, stacking and travel time picking, inversion) is illustrated in Figure 2.8.

We finally combine the 1-D velocity models derived at each of the CMP locations into a 3-D velocity model using a Kriging interpolation approach. Prior to interpolation, we discard any velocity element with a resolution element value less than 0.5 and further exclude all CMP locations with an RMS travel time residual greater than 20 ms. This results in a reduction of 37% of the calculated velocity data points to construct the final 3-D velocity model. The resulting 3-D velocity model (Figure 2.9) captures regional crustal structures up to depths of ∼40 km. Average velocities vary from 5.96 km/s at 5 km depth to 7.24 km/s at 40 km depth with overall minimum and maximum velocities of 5.56 km/s and 7.39 km/s, respectively. Average velocities for upper-to-middle crust (10-25 km) are very similar to the 1-D global velocity model as given by Christensen and Mooney (1995) for shields and platform. We observe higher average velocities for the uppermost crust (5-10 km) and the lower crust (>25 km).

Figure 2.9 shows the combined velocity model as depth slices at a 5 km interval starting from 5 km to 40 km. Our velocity model starts at 5 km depth, where we have assumed our processing datum. Due to velocity increase with

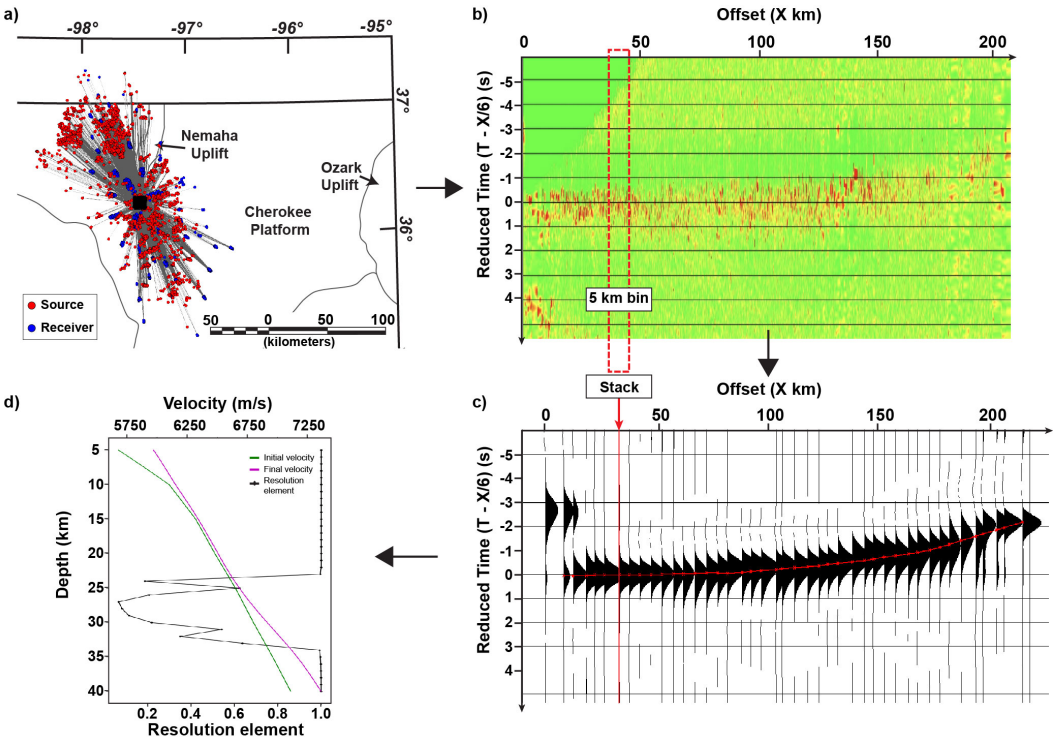


Figure 2.8: Processing steps illustrated for one CMP bin. (a) All source-receiver pairs (grey lines) shown for the CMP bin (black square); (b) Pre-processed earthquake waveforms in this CMP gather with a linear move-out correction of 6 km/s; (c) Stacked gather obtained from 5 km offset-bin stacking of sorted gather in b), red dashed line shows the picked travel time curve; (d) Initial and inverted 1-D velocity model, and resolution elements obtained for the CMP bin location.

depth, we chose a depth-dependent color scale in Figure 2.9 to emphasize lateral variations at each depth. To analyze the velocity model in more detail we have highlighted regions (Figure 2.9, regions A, B, C) which show velocity anomalies which are discussed in more detail in section 2.5.

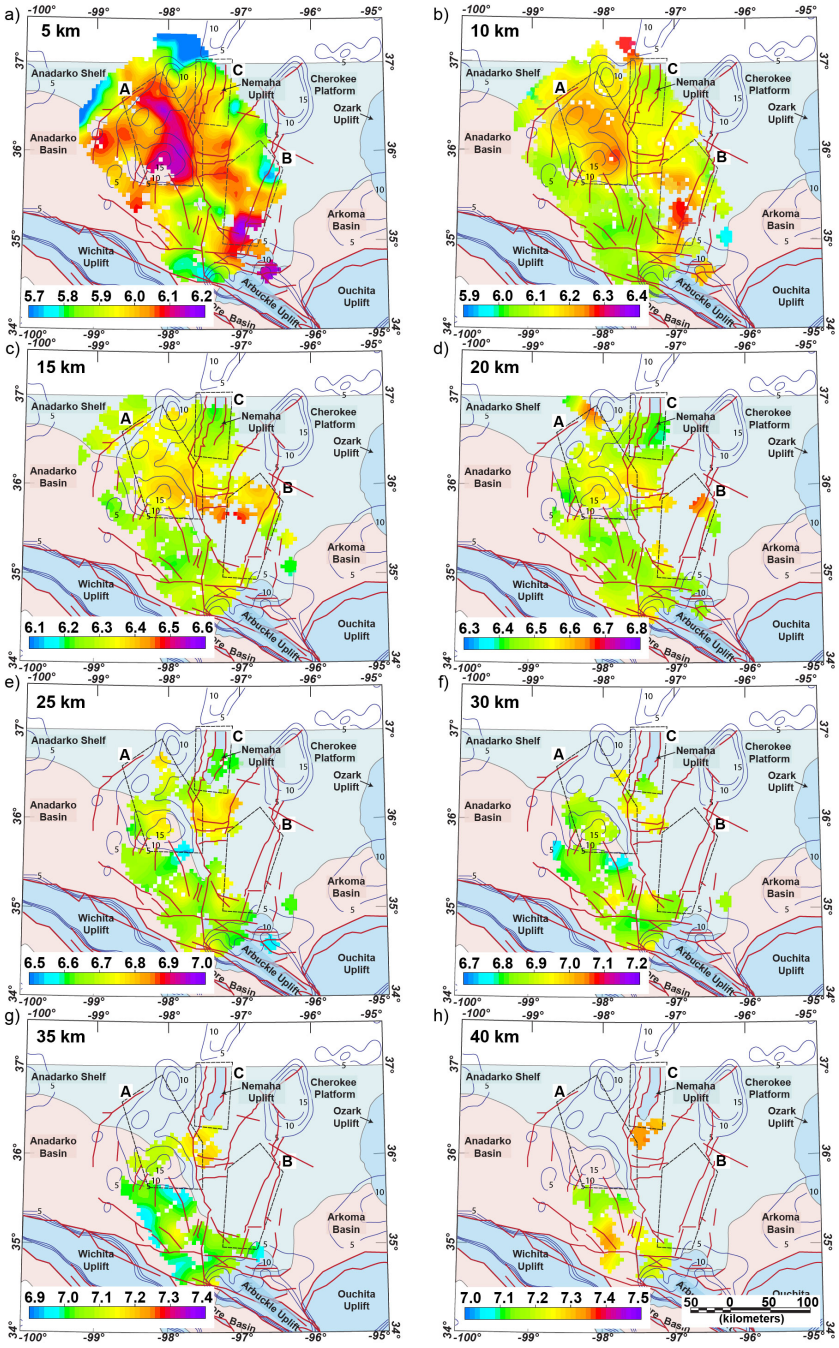


Figure 2.9: Horizontal slices through the 3-D Pg wave velocity model superimposed on the geologic provinces map. Note the varying color scale for each depth slice (same range of 500 m/s). Black contour lines show the Bouguer Gravity anomaly [mGal]. Regions A, B and C are discussed in the text.

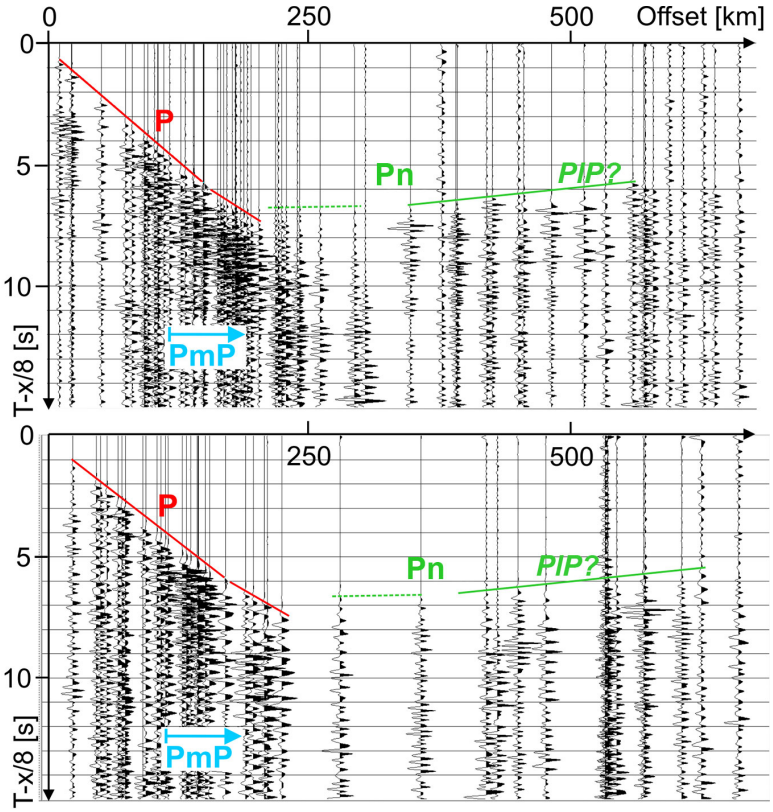


Figure 2.10: Examples of event gathers with interpreted Pg and Pn phases. The expected offset range for over-critical PmP arrivals is indicated by the blue arrow. Long offsets result from inclusion of US Array stations outside the investigated area. Strong Pn amplitude at large offsets might also represent a reflection from within the lithospheric mantle (PlP).

2.4.3 Other Crustal Phases (PmP, Pn, Reflections/Refractions from within the Uppermost Mantle)

In contrast to Pg waves, reflections (PmP) from the Mohorovičić discontinuity (Moho) are more challenging to interpret in the dataset (Figure 2.10). This is partly caused by the complexity and long duration of the source-time functions of the events, where the long Pg coda interferes with the following PmP arrivals. Furthermore, correlation of phases which are not first arrivals is hampered by the irregular and sparse recording geometry. Dynamic ray

tracing (Figure S2.19) shows that the critical offset can be expected about 110 - 120 km offset, and that the overcritical PmP amplitudes are not significantly stronger than Pg amplitudes for a model with a high-velocity/high-gradient lower crust. This is in accordance with the lack of observation of a generally weakly distinct PmP phases in the data. E.g. in Figure 2.10 we indicate the expected overcritical PmP offset range (110 - 180 km). While we find increased amplitudes in this range, it is not possible to discern a hyperbolic move-out. Ray tracing also shows that the predicted travel times of Pg and PmP phases are virtually identical at offsets larger than 160 km (Figure S2.19).

In active source seismology data from regions with comparable expected Moho depths and similar seismic crustal structure, the refracted wave from the upper mantle (Pn) may appear at offset range between ca. 180 and 400 km (Stratford and Thybo, 2011). The amplitude of the Pn phase increases with the velocity contrast at the lower crust - mantle boundary and the velocity gradient in the uppermost mantle. Consequently, a weak or absent Pn phase hints at high-velocity lower crust and/or low-velocity / low gradient uppermost mantle. Unambiguous correlation of a weak Pn phase requires dense station spacing, which is not a feature of our dataset. Nonetheless, a visual inspection of the event gathers shows a pronounced upper mantle phase at offset ranges 300 - 700 km (Figure 2.10). At shorter offsets (200 - 300 km), Pn phase appears of weak amplitude and with velocities around 8.0 km/s, while at large offsets the average velocity moveout increases to ca. 8.2 km/s with strong amplitudes. This might indicate a reflection from within the upper mantle at larger depths (Majdański et al., 2006; Oeberseder et al., 2011, e.g.), or a refraction arrival from a deeper high-velocity/high-gradient upper mantle layer. However, the sparse recording geometry challenges a firm interpretation of these long offset arrivals.

2.5 Discussion and Interpretation

2.5.1 Assessment of the 3-D Velocity Model

We assess the validity of our velocity model by calculating selected Pg arrival travel times and comparing them to pre-stack data. We define our 3-D raytracing model space as two layers separated by a basement interface derived from basement depth data from wells (Campbell and Weber, 2006). A 1-D velocity model for the sedimentary layer (Darold et al., 2015) and our final 3-D velocity model are used to populate the layers with P-wave velocities. The Pg travel time field at the surface is calculated for selected events using the ANRAY raytracing code (Gajewski and Pšenčik, 1987; Gajewski and Pšenčík, 1989). Figure 2.11 shows the calculated travel times superimposed on bandpass filtered event gathers. Since the origin time errors of the individual events are not known, we apply bulk time shifts to the events in order to visually align the first arrival phase with the calculated travel time curve. Overall, we find that the shape and move-out of the travel time curves agree well with the observed first arrival-phase, in particular at large offsets (>180 km) which represent the high-velocity lower crust. A quantitative and localized analysis of the travel time misfit would require picking of individual traces in the event gathers, consideration of (unknown) hypocenter locations and origin time errors, and updates to the basement depth map and sediment velocities. Our qualitative assessment indicates that main features in our model, such as high-velocity lower crust and the lateral velocity distribution in the upper crust, can explain the data well, and that the model would provide a robust initial model for LET inversion based on individually picked travel times. In conventional travel time tomography studies, checkerboard tests are commonly applied to assess the resolution capability of a specific data set. Our methodology invokes stacking

and goes beyond travel time picking, and as such would require the creation of several synthetic wavefield data sets which in turn would rely on assumptions on the earthquake source characteristics. This challenge is again aggravated by the unknown hypocenter locations and origin time errors. Taking these major assumptions and uncertainties into account, we find it unfeasible to run conclusive checkerboard or similar resolution tests for the entire area. However, we perform a simplified resolution test to address the imaging capability for the MCR region (cf. section 2.5.4; supplemental material figures S2.20, S2.21).

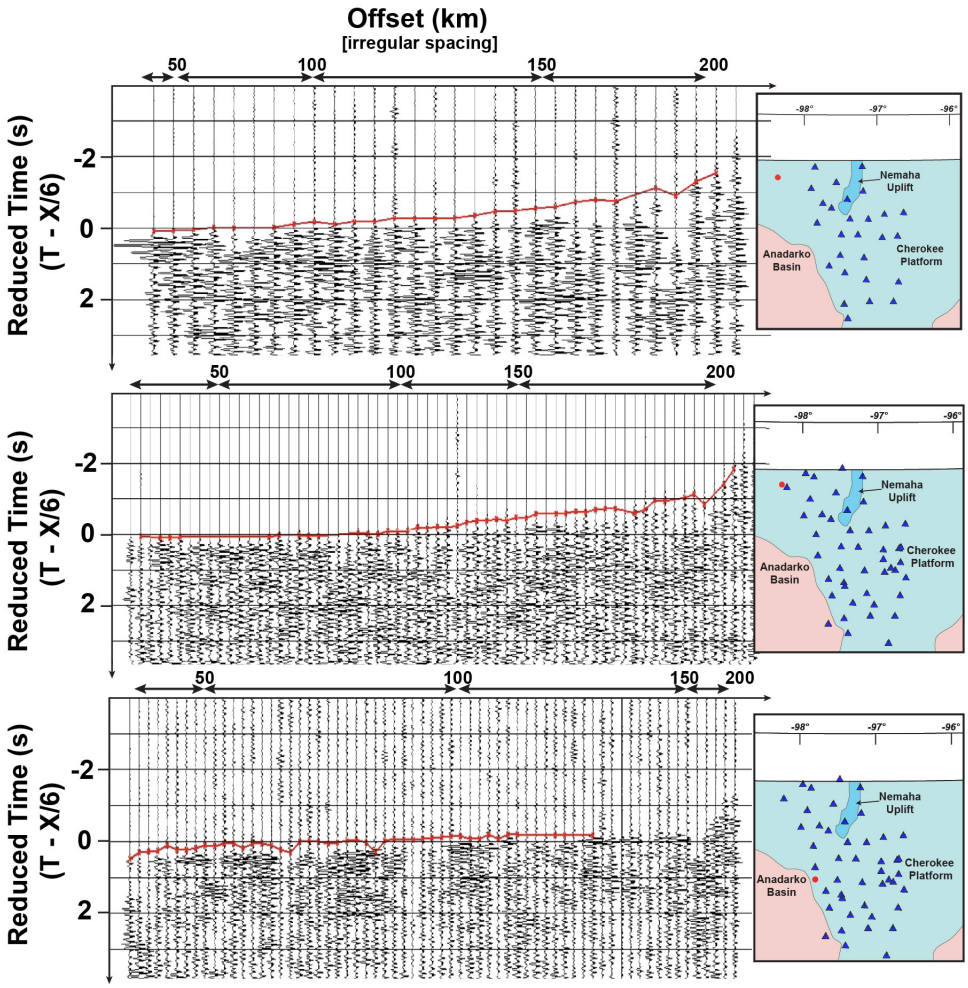


Figure 2.11: Three bandpass filtered, LMO corrected, and bulk-shifted event gathers with respective event locations (red dot) and receiver locations (blue triangles) shown in map insets. The red curve plotted on each of the event gathers represents the calculated first arrival travel time for our final 3-D velocity model.

2.5.2 Comparison with Existing Velocity Models

Regional crustal models available for Oklahoma based on ambient noise interferometry (Shen and Ritzwoller, 2016; Zhu, 2018) provide the S-wave velocity distribution and thus are not directly comparable to our model. Shen and Ritzwoller (2016) show S-wave velocities for the crust and upper mantle for the entire continental US with comparably low resolution. However, it is worth noting that central Oklahoma shows up as a lower crustal high velocity feature (4.15 - 4.2 km/s) in their model. Given an average lower crust P-wave velocity of 7.2 km/s in our model, this would translate to an average lower crustal V_P/V_S ratio of ca. 1.73. Since ambient noise inversion smears out velocities between the lower crust and the upper mantle, and therefore increases the apparent lower crustal S-wave velocity, we suggest that the actual V_P/V_S ratio is higher. The model by Zhu (2018) has finer resolution, and also images high velocities associated with region A and lower velocities below the Anadarko basin in the upper and middle crust.

There have been two major studies that have developed regional P-wave velocity models for the crust in Oklahoma. Chen (2016) developed a 3-D velocity model for the upper crust (up to $\sim$15 km depth) using traditional travel time tomography applied to local earthquake waveforms. We correlate the velocity regions A, B, and C with similar velocity anomalies observed in the cross-sections A4 and A5 (Figure S2.22) from Chen (2016)'s model. They interpret the high velocity anomalies of region A as the Midcontinent Rift and regions B and C as intrusions in the crust. The depth of investigation for their model is limited to about 15 km.

The second regional velocity model was developed by Pei et al. (2018) who used a 2-D lateral tomographic technique (Pei et al., 2013) to obtain high-resolution anisotropic velocities for the uppermost crust. Their model

represents a depth-averaged velocity model for 5-10 km in the upper crust. They pick first arrival travel-times for waveforms with offsets up to 130 km. We observe significant differences in some areas when comparing our results to this model. The high velocity anomaly in region A (Figure 2.9) is not observed in their model, but they interpret a high velocity anomaly just south-east of region A. They also observe less prominent positive velocity anomalies west of region A (Figure 2.9). These differences might be related to the different methodologies used in calculating the velocity models. Pei et al. (2018) chose a data set with epicentral distances varying from ∼32 km to ∼130 km and assume a head wave ray path for all the travel times irrespective of the epicentral distance. As the Pg phase dives down with increasing offset, the head wave path assumption for offsets as far as 130 km is becoming increasingly inaccurate which may lead to artifacts in velocity imaging. Our calculations show that the curved ray paths at 120 km offset penetrates down to 15 km depth (Figure S2.23). Assuming a head wave geometry, the velocities in the mid-crustal depth range between the hypocenters and 15 km will be projected to the shallow part of the basement. Another point of difference is the model assumption of isotropic crust in our model whereas Pei et al. (2018) considers anisotropy.

2.5.3 Crustal Structures

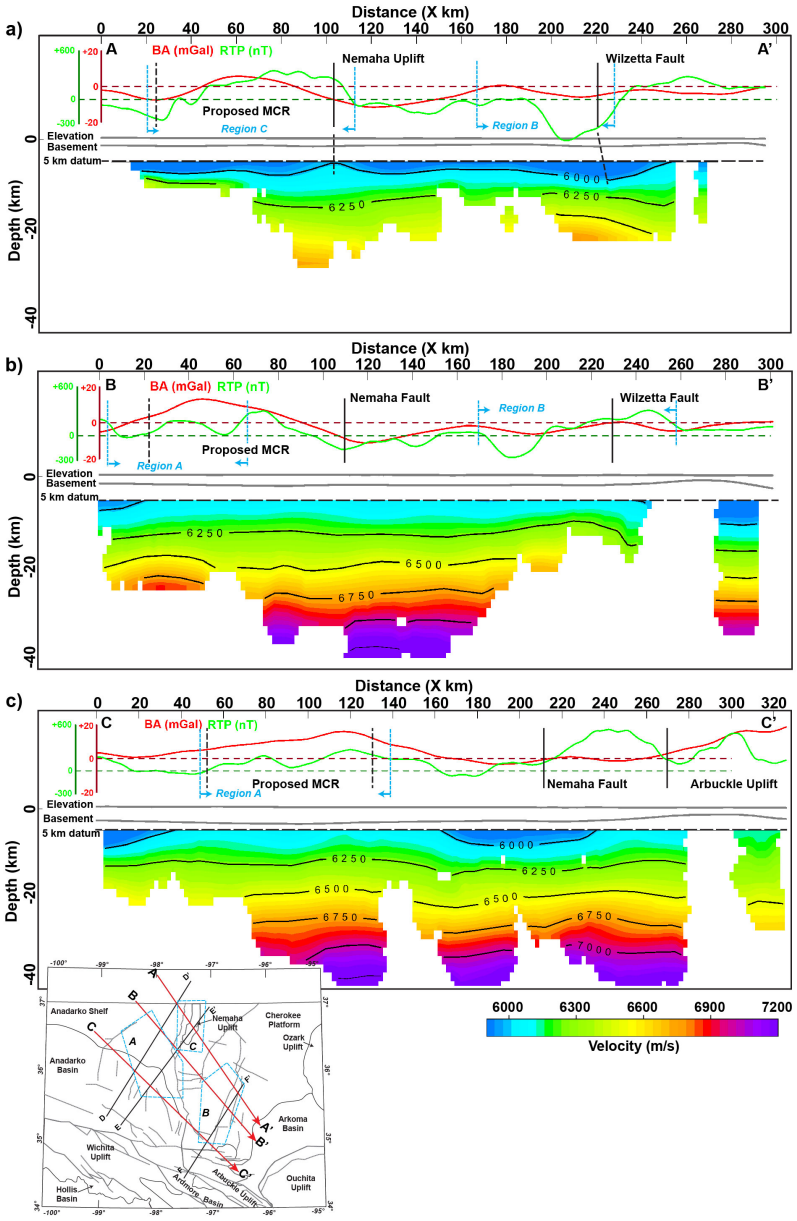
The upper crust in Oklahoma shows significant lateral velocity variations implying that the upper crustal structure is more complex than an overall granitic basement may suggest. We observe high velocity anomalies at 5 km depth (Figure 2.9a; regions A and B) in roughly NW-SE direction. This prominent high velocity region extends down to depths of ∼15 km (Figure 2.9b, c; Region A) but decreases in intensity and lateral extent as the depth increases.

Region A appears to be bounded at its eastern side by the Nemaha fault system. Cross-sections CC', DD' and EE' (Figure 2.12 c, d, e) show these high velocity anomalies in the upper crust as well. These high velocity anomalies correlate with gravity anomalies. Chen (2016) interpreted this anomaly as evidence for the extension of the Midcontinent Rift into northern Oklahoma. Our model extends deeper in this region and we observe that the velocity anomaly is only present in the upper-middle crust extending down to about 20 km in depth (Figure 2.9, Figure 2.12c). A high velocity shear wave anomaly is also observed for region A by Shen and Ritzwoller (2016) in their middle crust and in depths between 10 and 20 km in the model by Zhu (2018). Several authors (Chopra et al., 2018; Kolawole et al., 2020) have mapped intra-basement reflectors in 3-D (industry) active seismic data in depths between 8 to 10 km and have interpreted them as mafic sill intrusions (Kolawole et al., 2020). We correlate the high velocity anomaly observed with the occurrence of intra-basement reflectors in this region. The mafic nature of these intra-basement reflectors may explain the anomalously high velocity and suggests mafic layering over a significantly larger depth range.

We observe another high velocity anomaly in south-central Oklahoma (Figure 2.9 a, b, c, d; Region B) which appears more complex. We observe a decreasing intensity in the southern part with depth while the anomaly in the north seems to be stronger in the middle crust. The southern anomaly corresponds to a magnetic high (Figure 2.12f) while the northern anomaly corresponds to a magnetic low. The different magnetic signatures of the two high velocity anomalies indicate differences in lithological composition of the shallow to mid crust. However, we also note that this area has larger cell size and comparatively lower number of rays (Figure 2.5). Subsequently, the velocities here are less well constrained compared to other parts in our model.

The high velocity anomaly in the northern part of region B in the middle crust is overlain by a low velocity anomaly in the upper crust (Figure 2.12a), which could explain the absence of a distinct gravity anomaly. As gravity data represent the integrated crustal structure in the subsurface, the combination of this low and high velocity anomaly may lead to an absence of a pronounced gravity anomaly.

We observe lower velocities in the north-east corner (Figure 2.9b-e; region



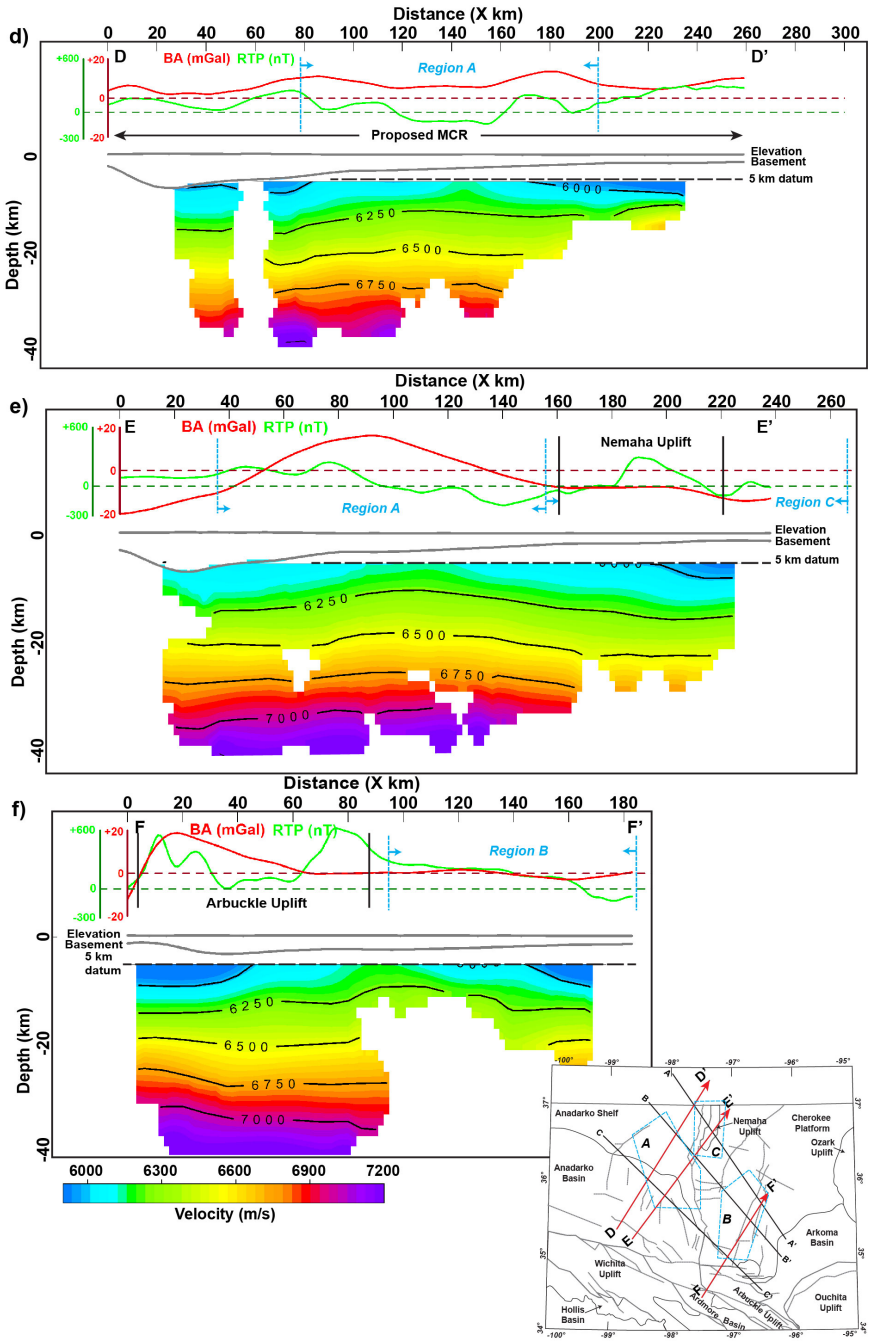


Figure 2.12: Pg-velocity model cross-sections. Bouguer gravity anomaly (red curve) and magnetic anomalies (green curve) are plotted above corresponding cross sections. On cross sections, black vertical lines show fault locations and blue vertical lines show extent of regions (A,B,C). Inset maps show the fault locations (grey lines), location of regions A,B,C (blue polygons) overlain on geologic province map. "Proposed MCR" indicates the tentative continuation of the Midcontinent Rift as suggested by previous studies. See text for discussion.

C) in the velocity-depth cross-sections up to depths of at least ∼25 km. These low velocity anomalies can be correlated with the Nemaha uplift in this area. AA' and EE' (Figure 2.12) show a decrease in mid-crustal P-wave velocity associated with the Nemaha uplift and northern part of the Nehama fault system in cross sections that run both across and along this fault zone. The lower velocities are observed up to 25 - 30 km depth, which suggests that the Nemaha fault zone has a deep root in the crust. The Wilzetta fault zone is also observed as a low velocity anomaly in the upper crust in the AA' cross-section (Figure 2.12a). The Anadarko basin region in the west is represented with generally lower velocities in the upper, mid, and lower crust (Figure 2.9).

P-wave velocities in the lower crust range from 7-7.3 km/s which are higher than the global average for shields and platform tectonic regime (Christensen and Mooney, 1995). Our velocity model therefore is in agreement with the assumption of a mafic lower crust in Oklahoma, as suggested by several crustal evolution models. High lower crustal velocities were also observed in the vintage 2-D active seismic survey in Oklahoma (Brewer and Oliver, 1980; Buckey, 2012; Mitchell and Landisman, 1970; Tryggvason and Qualls, 1967). The presence of a high velocity lower crust throughout the investigated area provides strong evidence for the formation of granite-rhyolite province through crustal melting of older crust. Similar high velocity lower crustal layers have been found in other parts of the world and are considered to be a result of underplating (Meissner et al., 1986; Snelson et al., 1998; Thybo and Artemieva, 2013). Velocities in the lower crust as seen in BB', DD' and EE' (Figure 2.12) are mostly homogeneous and do not show significant lateral variations. We do not observe variation across the "Nd-line" in Oklahoma either. The "Nd-line" is regarded as a suture-zone based on model age studies of the mid-continent's basement rocks (Nelson and DePaolo, 1985). Lack of velocity variations across

the assumed suture zone does not confirm or deny its existence, as episodic accretion could have created a more complex terrane with the possibility of several sutures over time. Also, a variation in age does not necessarily imply a strong variation of velocity.

2.5.4 Implications on the Midcontinent Rift (MCR) Structure

In general, rifts are associated with low gravity anomalies due to the accommodation space created by the rift being filled by sedimentary rocks which have lower densities (Stein et al., 2015, 2018b). The MCR is unique in that the rift is filled with voluminous basalts and volcanic sequences that give it the characteristic strong positive gravity anomalies. There is no clear evidence for surface and/or subsurface structural expression of the MCR in Oklahoma so far. Positive gravity anomalies in northern Oklahoma (Figure 2.1) have been used to postulate the existence of the MCR in Oklahoma (Kolawole et al., 2020; Stein et al., 2014) but the actual magnitudes of these anomalies are smaller by factors of 3 to 15 compared to the MCR in Kansas and Minnesota. Our model shows that positive but still moderate velocity anomalies can be associated with the gravity highs in the upper crust ($\sim$5-20 km). As discussed before, these anomalies are interpreted as intrusive sills in the basement. These high-velocity anomalies do not extend deeper which questions the presence of a rift structure in northern Oklahoma. Cross section CC' (Figure 2.12) shows velocity variations across the proposed MCR. The high V_P anomaly associated with the gravity high is more prominent in the upper crust-middle crust in this cross-section. EE' cross-section cuts through the same gravity high as CC' but in an orientation parallel to the proposed rift structure (Figure 2.12). It is more evident in the profile EE' that the velocity anomaly associated with the

gravity high is related to the structure of the upper crust. DD' cross-section runs along the longitudinal axis of the proposed MCR. We also perform synthetic tests with an assumed velocity model for a rift structure in Oklahoma (supplementary material figures S2.20, S2.21) to evaluate if the source-receiver geometry and CMP sorting and inversion methodology is sufficient to detect a high-velocity rift structure. Although the source-receiver geometry shows not to be optimal for illuminating a NE-SW trending rift structure, the test reveals that a high-velocity intrusion comparable to the northern part of the MCR would still show up in the inverted velocity models. The lateral variation in P-wave velocity in the upper crust (lower velocities in the south and comparatively high velocities in the north) can also be correlated with the basement below the Anadarko Basin structure which exhibits overall lower crustal velocities in both our model and the S-wave model by Zhu (2018).

The geology of the mid-continent region has been influenced by several tectonic events, including the episodic emplacement of the Southern Granite-Rhyolite province (1.5-1.3 Ga), the midcontinent rifting event (∼1.1 Ga), the Grenville orogeny which led to the final assembly of Rodinia (∼1.3-1.09 Ga), and the intermittent breakup of Rodinia (∼0.78-0.53 Ga) which also led to the formation of the Southern Oklahoma Aulacogen. Mafic intrusions and high velocity anomalies in the upper and middle crust are present not only in the proposed MCR region, but are also observed in several active seismic studies throughout central Oklahoma as well as in the granite-rhyolite terrane in the Southern Oklahoma Aulacogen, Osage county, and in northwest Texas (Buckey, 2012; Brewer et al., 1981, 1983, 1984; Elebiju et al., 2011; Mitchell and Landisman, 1970; McBride et al., 2018). We also interpret high velocity anomalies in the region "B" in our velocity model as similar intrusive structures. The widespread presence of such structures across the Southern

Granite-Rhyolite terrane suggests that the intrusions could be a result of a large-scale tectonic episode, and are not necessarily related to the MCR.

2.5.5 Seismic Velocities and Spatial Distribution of Seismicity

The spatio-temporal distribution of seismicity in the investigated area is related to factors such as the presence of injection wells, injection volume, optimal fault orientations, porosity and permeability, and basement rock lithology (Ellsworth, 2013; Keranen et al., 2014; Qin et al., 2018, 2019). Many of the earthquakes in Oklahoma have occurred on previously unmapped faults, thus a lack of mapped faults cannot be used to argue for the lack of seismicity in this area. Figure 2.13 illustrates the location of earthquakes, injection wells, and injection volumes in the area (Murray, 2014). We have considered only the wells classified as salt-water disposal wells for this analysis, as the seismicity in Oklahoma has been connected to the waste water injection wells (Keranen et al., 2014; Weingarten et al., 2015). We observe a pronounced lack of seismicity in the high-velocity region A (Figure 2.13). In this area, the number of injection wells is still significant, and the injection volumes are similar to areas with high seismicity. We therefore argue that the lack of earthquakes in this area is related to the variable basement lithology as indicated by the velocity distribution. Lithologic control on seismicity is observed in eastern Oklahoma, where high-volume injection wells have not caused an increase in seismicity (Shah and Keller, 2017). We suggest that the rocks associated with the high velocity anomalies are likely to have higher strength and thus would require higher stress conditions for fault rupture, and/or the basement lithology of this region is less prone to faulting and fracturing. A lesser degree of fracturing would also imply low permeability and less vertical fluid migration,

which would eventually lead to comparably low pore pressure buildup in the region. Basement lithology can influence the pore space distribution, permeability and deformation capability, all of which in turn could control seismicity.

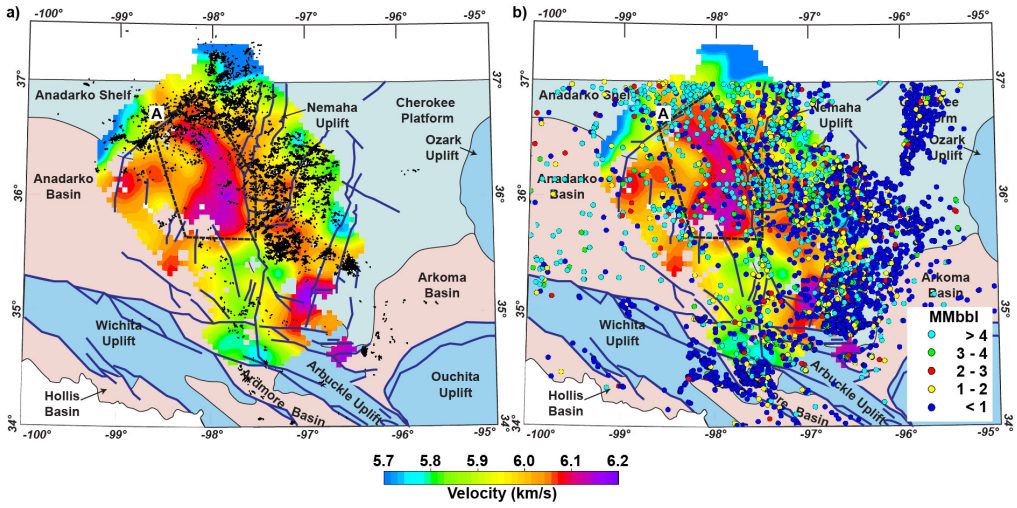


Figure 2.13: a) Earthquake locations; b) Total injection volume (MMbbl) for saltwater disposal wells from 2011-2017, overlain on the velocity slice at 5 km depth. The absence of seismicity in the high-velocity regions is discussed in section 2.5.5.

2.6 Conclusions

In this study, common-mid-point sorting, stacking, and inversion techniques are applied to local earthquake waveform data in the central part of the mid-continent. In contrast to traditional local earthquake tomography (LET) studies from Oklahoma that have imaged the upper crust, our methodology results in a 3-D P-wave velocity model for significantly larger depths. Our results suggest a more heterogeneous upper and middle crust and a relatively homogeneous lower crust. These observations are interpreted to reflect a complex geologic history including deformations in the upper and mid-crustal depths and a possible homogenization of the lower crust through melting. The

high velocity (>7 km/s) lower crust is indicative of mafic composition. This provides strong evidence for the evolution of the Southern Granite-Rhyolite province from basaltic underplating and crustal melting. Our model does not suggest the extension of the Midcontinent Rift (MCR) structure in Oklahoma similar to as observed in the northern segment of the rift. Several (possibly mafic) intrusions are interpreted in the upper to middle crust from high velocity anomalies which have previously been associated with the MCR extension in Oklahoma. However, the widespread occurrence of these intrusions in Oklahoma may suggest their derivation from a regional tectonic event. Our results also suggest lithologic control on induced seismicity in Oklahoma.

The suggested workflow is potentially applicable to other areas with similar datasets. Robust 3-D velocity models derived by this methodology can also be used for improved earthquake localization, and in particular as initial models for local high-resolution LET analysis. Future work will focus on applying the methodology to obtain a comparable S-wave velocity model for central Oklahoma, as integration of S- and P-wave velocities can provide a strong basis for mineralogical and geochemical interpretation of the entire crustal column.

2.7 Supplementary Materials

2.7.1 Introduction

The supporting information consists of ten figures and two data sets. The text below describes the simplified synthetic test performed in order to assess the capability of our data and methodology to image a rift structure in Oklahoma. The figures provide additional information about data used in the study, processing steps and a more detailed comparison of the final velocity model to the velocity model by Chen (2016) (Figure S2.14-S2.22). Figure S2.23 adds more detail to our discussion with regards to (Pei et al., 2018) in the main text.

2.7.2 Resolution Assessment

We assess the resolution capability of the CMP sorting and inversion methods for a potential MCR structure through simplified synthetic modelling. In a first step, we create a 3D velocity model for an assumed rift structure based on previous studies from the northern part of the MCR ((Chichester et al., 2018; Stein et al., 2016; Zhang et al., 2016), Figures S2.20a-f). The location and strike direction of the rift aligns with the proposed continuation into Oklahoma (Stein et al., 2014). Since there is limited robust information on the seismic P-wave velocity structure of the MCR, our model captures just the main characteristics such as a general positive velocity anomaly and a broadening of the high-velocity feature at its base (e.g., mafic underplating). The background velocity model is a linear gradient approximation to the average of all our 1D velocity depth functions and as such is assumed to represent "regular" Oklahoma crust. Next, we chose two CMP bin locations (blue dots/rectangles in Figure S2.20a,b) and their according downward-continued source/receiver

pairs from the data set (red and green dots in Figure S2.20a,b). Travel times for all receiver pairs are calculated with an Eikonal solver (Hole, 1992). Those travel times are grouped and averaged into 5 km offset bins (Figures S2.21a,c), which aims at simulating the corresponding picked first arrival in the offset-stacked CMP gathers. Offset bins with less than 10 arrivals are rejected. The resulting travel time curves (blue lines in Figures S2.21a,c) are inverted for 1D velocity models (blue lines in Figures S2.21b,d). It can be shown that the true velocities are underestimated but there is still a significant velocity increase in the inverted models. This in particular applies to long-offset data which travel through the broadest (deepest) part of the rift. The velocity underestimation is attributed to the unfavorable azimuthal coverage, e.g. the source/receiver pairs are mostly aligned perpendicular to the rift structure and the seismic rays sample both the outside "regular" crust and the rift. Four the given source-receiver geometry, bins with short-offset coverage are less likely to show evidence of the rift, while bins with long-offset coverage should successfully illuminate a high-velocity rift structure.

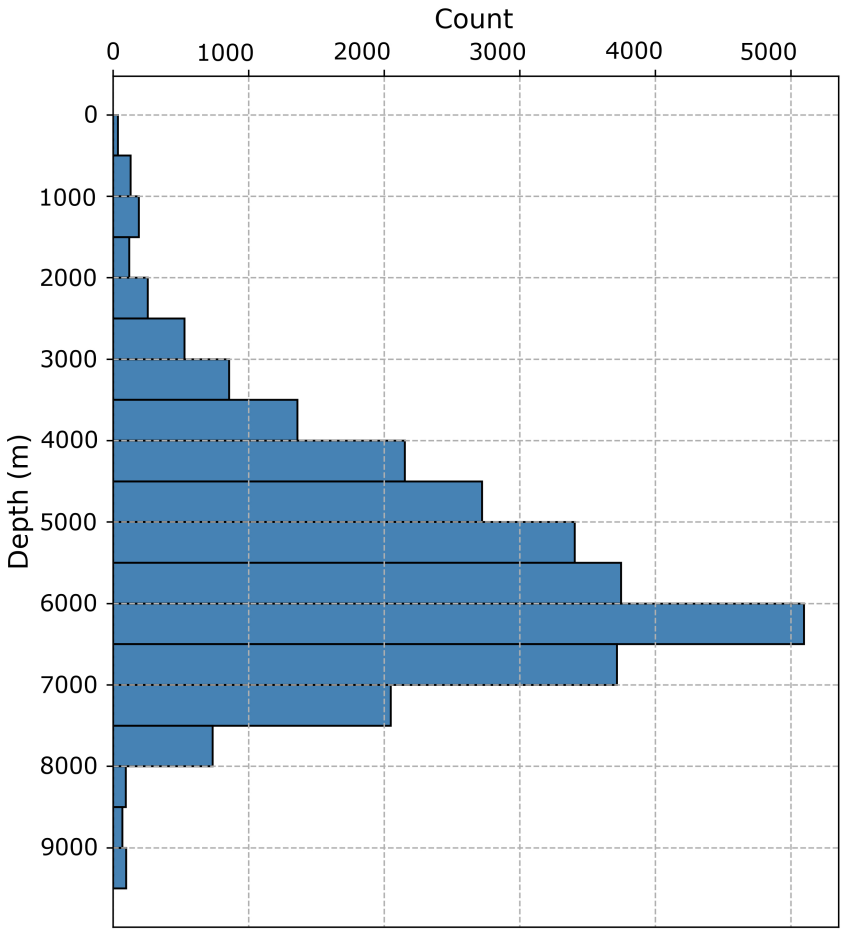


Figure S2.14: Depth distribution of earthquakes used in this study.

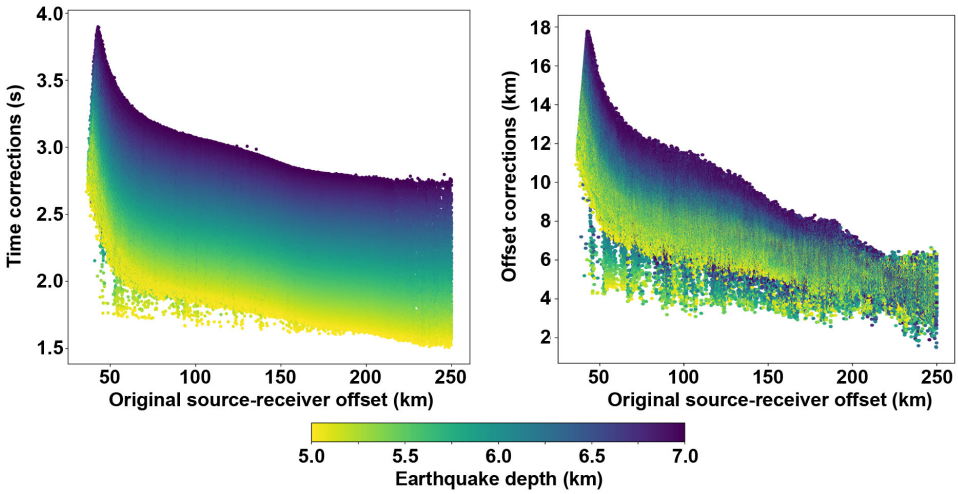


Figure S2.15: Range of time and offset corrections for raytracing-based redatuming to a reference level Z=5 km as a function of source-receiver offset and earthquake depth. Each point on the graphs represent one source-receiver pair. The scatter is caused by the non-linear relationships between ray geometry, basement depths, earthquake depths, velocity distribution, and source-receiver offset. Colors represent earthquake depth (km).

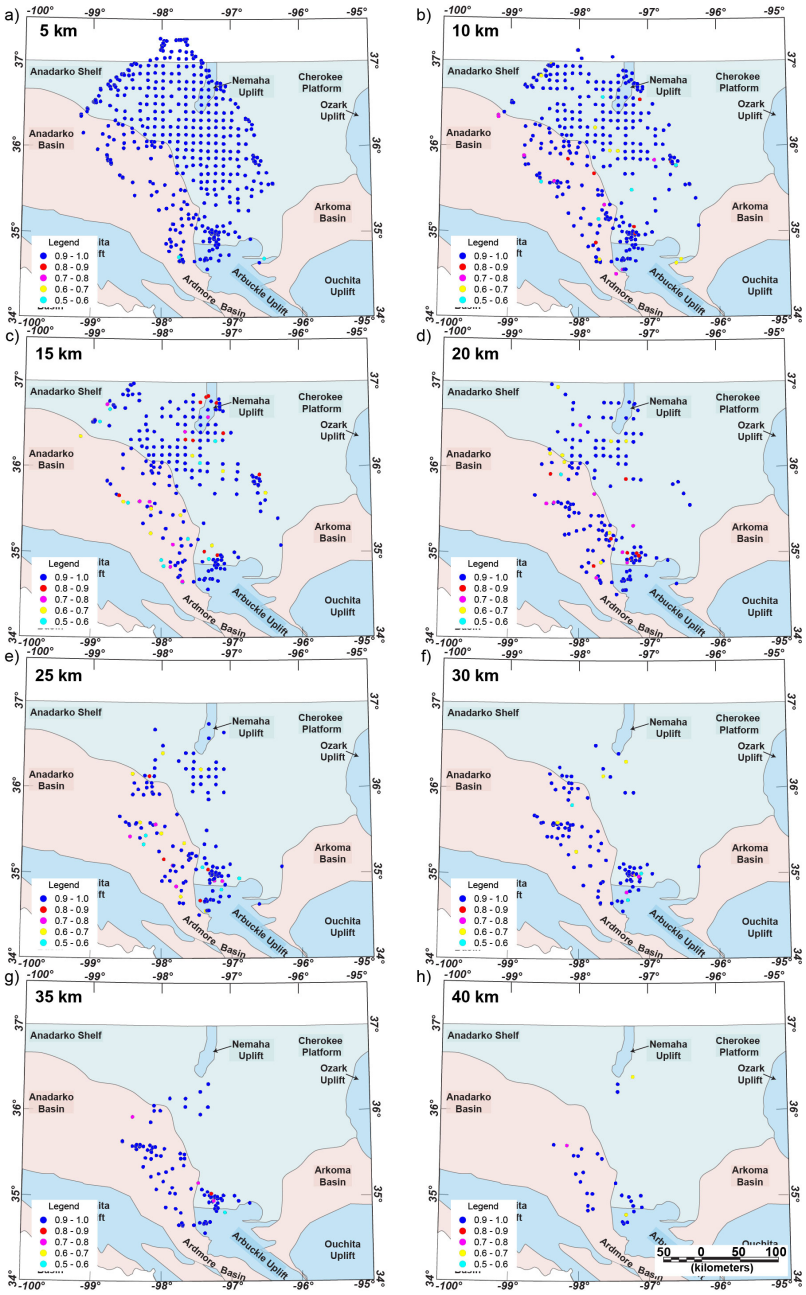


Figure S2.16: Resolution elements for each velocity element at a given depth and CMP location shown for 5-40 km depth slices.

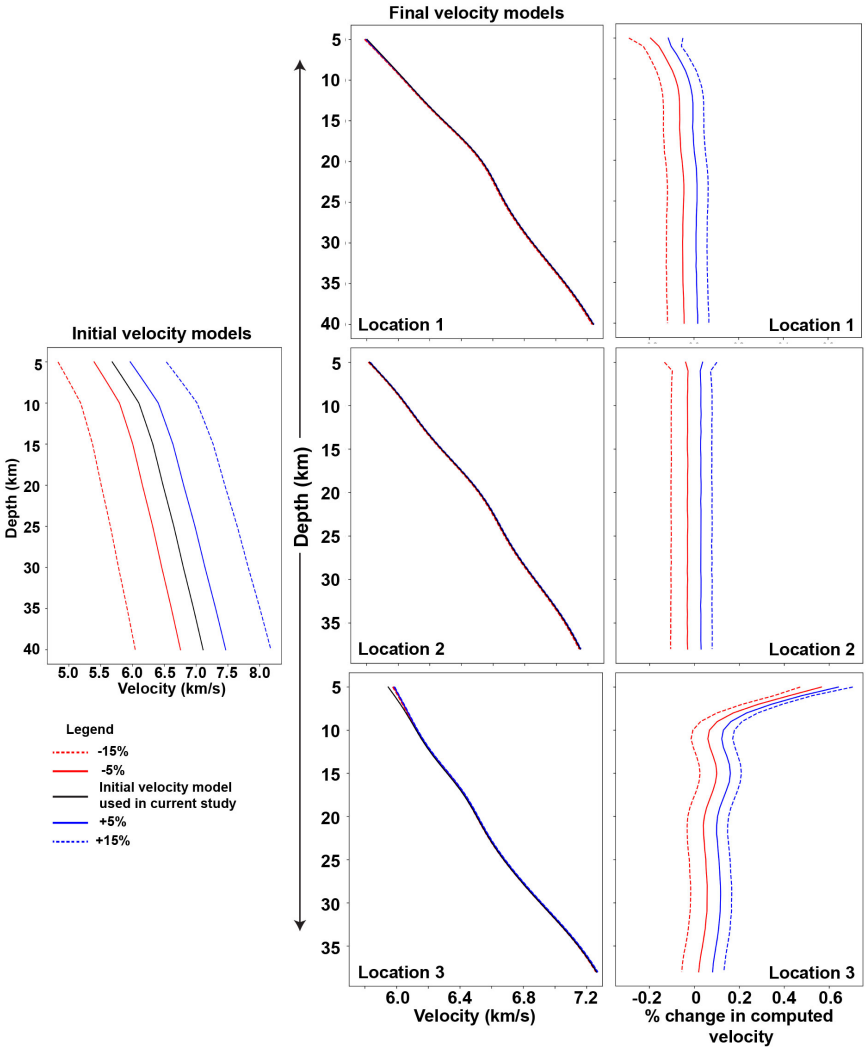


Figure S2.17: We test for dependency on initial model during inversion by inverting for different initial models. Left panel: Initial velocity models used for inversion. The black line shows initial velocity model used in this study. Coloured lines show perturbations introduced to the initial model (in black). Middle panel: Examples of 1-D velocity model computed using the perturbed models as initial models for real travel times from three different locations in this study. Right panel: Corresponding percentage change for each of the final velocity models computed from modified initial models when compared to final velocity model reported in the study. For up to 15% perturbations in the initial model we only observe deviations of $\sim$ +/-0.2% with a maximum deviation of $\sim$1%.

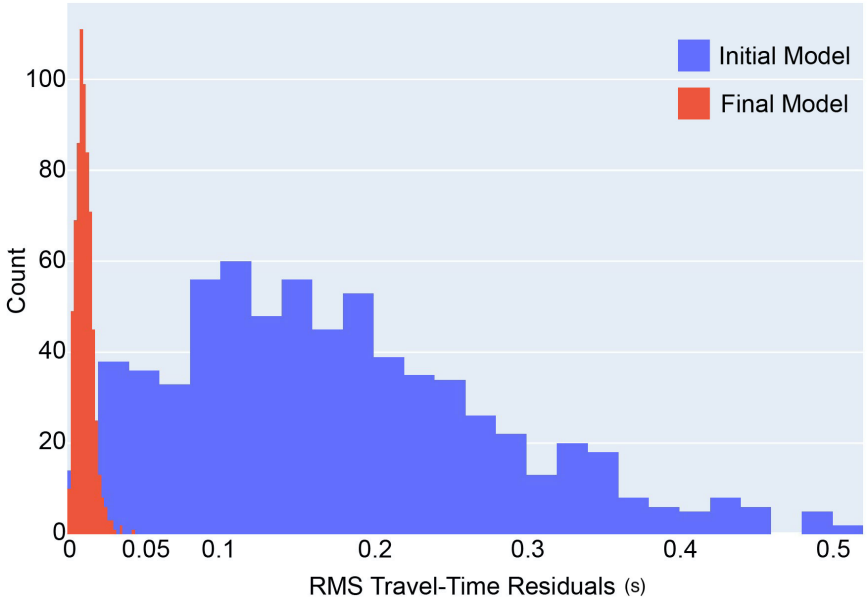


Figure S2.18: Histograms for RMS travel time residuals before (blue) and after (red) 1-D travel time inversion. Used data points are the RMS residuals of all 1-D inversions (n=686).

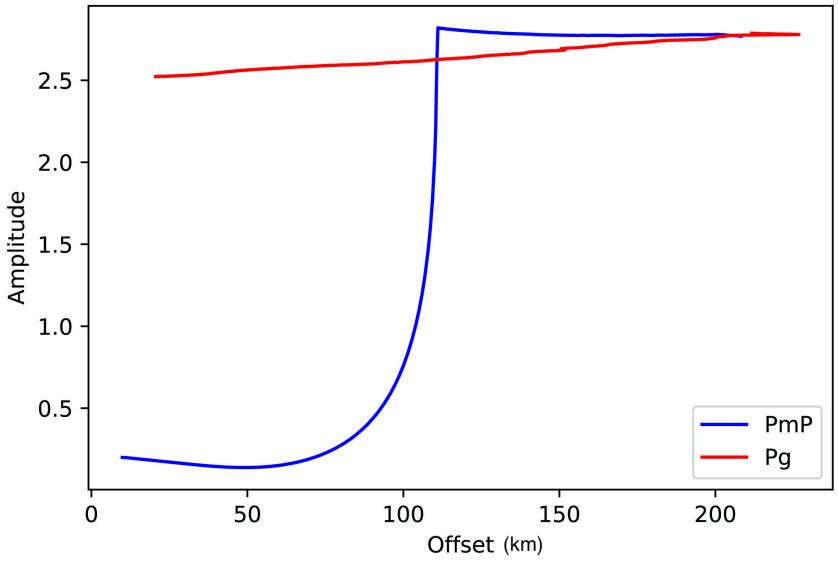


Figure S2.19: Relative Pg and PmP amplitudes without spherical spreading, calculated for a representative 1-D crustal model, a Moho depth of 42 km, and an event depth of 5.5 km. The strong Pg amplitude in the critical PmP offset range as well as similar travel times of the two phases illustrates the difficulty of identifying a clear PmP phase in the data.

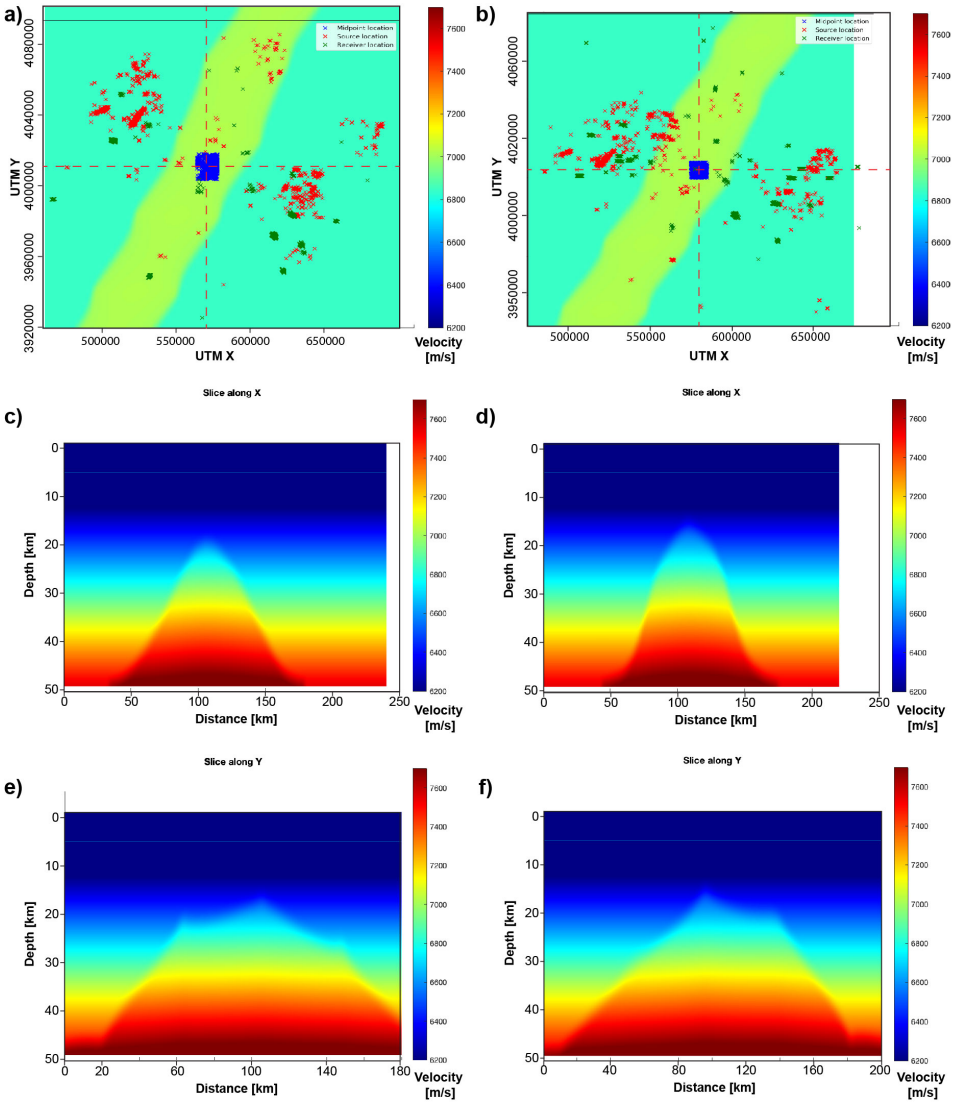


Figure S2.20: (a,c,e) show velocities in Z, X and Y directions respectively for bin#1. (b,d,f) show velocities in Z, X and Y directions respectively for bin#2. Source, receiver and mid-point locations for each of the bins are shown in (a,b).

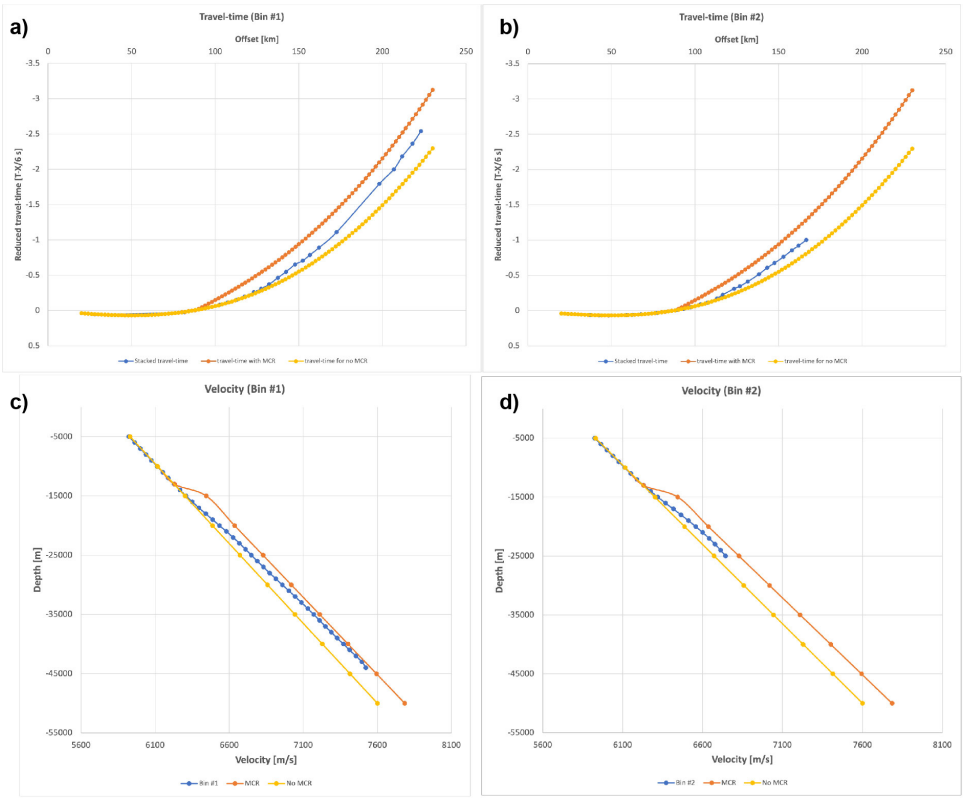


Figure S2.21: Modeled travel times and corresponding inverted velocity model for bin#1 are shown in blue in a) and b) respectively. Modeled travel times and corresponding inverted velocity model for bin#2 are shown in blue in c) and d) respectively. Orange and yellow lines in (a,c) show the corresponding 1D travel time curves for locations at the rift axis and outside the rift, respectively. Higher velocity estimates as compared to velocity model with no MCR, are obtained for both the bins using the source-receiver geometry used in this model. This implies that the source-receiver geometry used in the model is sufficient to estimate velocity anomalies that may result from highly mafic structure of the MCR.

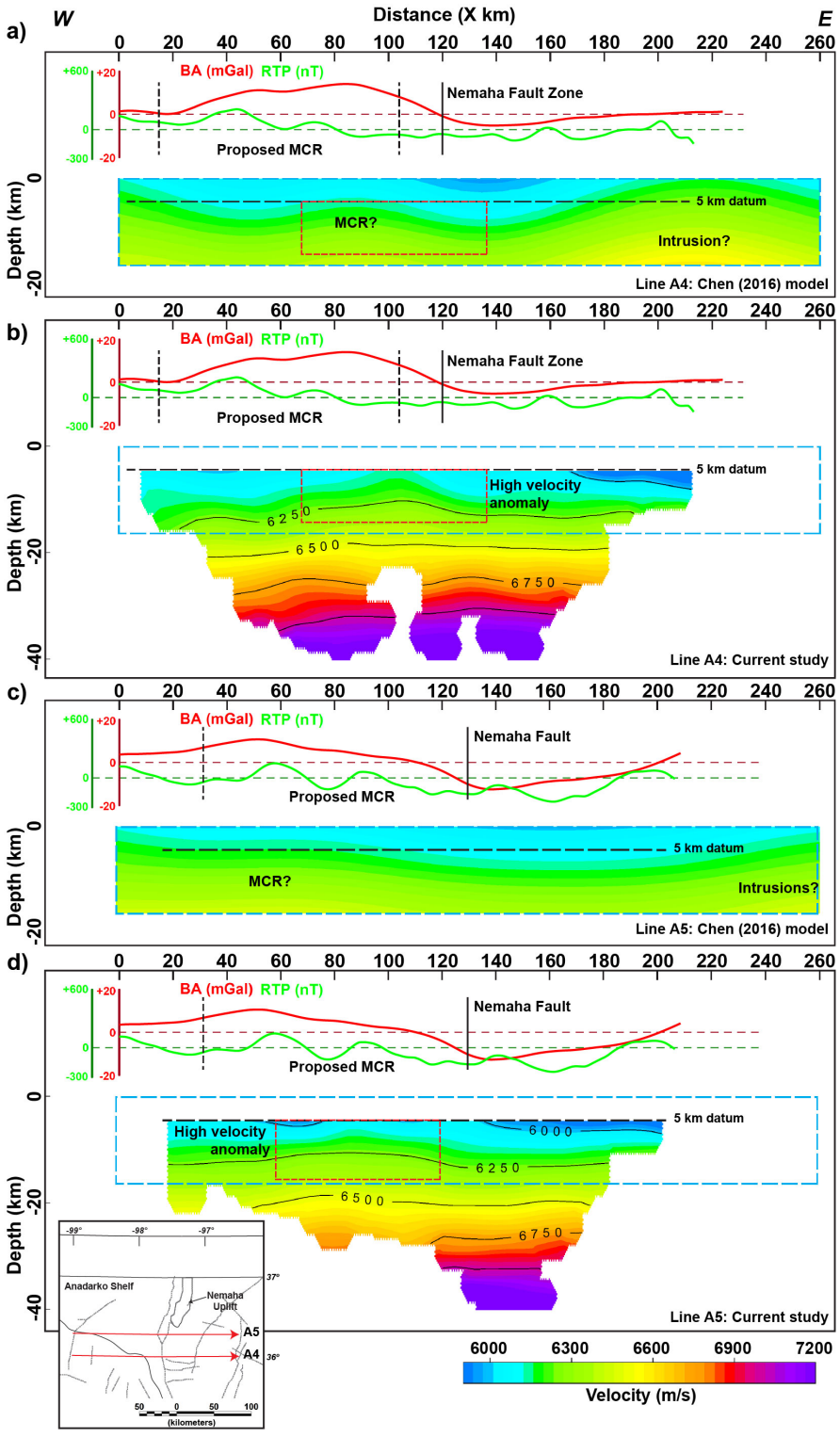

a)
W
Distance (X km)
E
0 20 40 60 80 100 120 140 160 180 200 220 240 260
BA (mGal) RTP (nT)
+600 +20 0 -300 -20
Nemaha Fault Zone
Proposed MCR
Depth (km)
0
-20
5 km datum
MCR?
Intrusion?
Line A4: Chen (2016) model
b)
BA (mGal) RTP (nT)
Nemaha Fault Zone
Proposed MCR
0
-20
-40
5 km datum
High velocity anomaly
6250
6500
6750
Line A4: Current study
c)
BA (mGal) RTP (nT)
Nemaha Fault
Proposed MCR
5 km datum
MCR?
Intrusions?
Line A5: Chen (2016) model
d)
BA (mGal) RTP (nT)
Nemaha Fault
Proposed MCR
5 km datum
High velocity anomaly
6000
6250
6500
6750
Line A5: Current study
-99° -98° -97°
37°
36°
Anadarko Shelf
Nemaha Uplift
A5
A4
50 0 50 100
(kilometers)
6000 6300 6600 6900 7200
Velocity (m/s)

Figure S2.22: A comparison of velocity model from Chen (2016) and current study. 2-D velocity profiles A4 and A5 refer to figures 2.17d and 2.17e in Chen (2016) thesis. a) and c) show lines A4 and A5 respectively, adapted from Chen (2016); and b) and d) show lines A4 and A5 respectively as computed in current study. Blue box shows the extent of velocity model by Chen (2016) for respective profiles. They interpret high velocity anomalies shown in red box, to be correlated to Midcontinent rift as shown in a) and c). Here we observe that in deeper sections, the high velocity anomaly either disappears (as in b)) or becomes less prominent (as in d)). This lends to the interpretation that these velocity anomalies are present mostly in the upper crust and may not be related to a lower crustal rift structure. They also interpret intrusions on the eastern side of profiles A4 and A5 (a) and c)). We observe similar high velocity anomalies in the same area (ref. Figure 2.9 region B in main text).

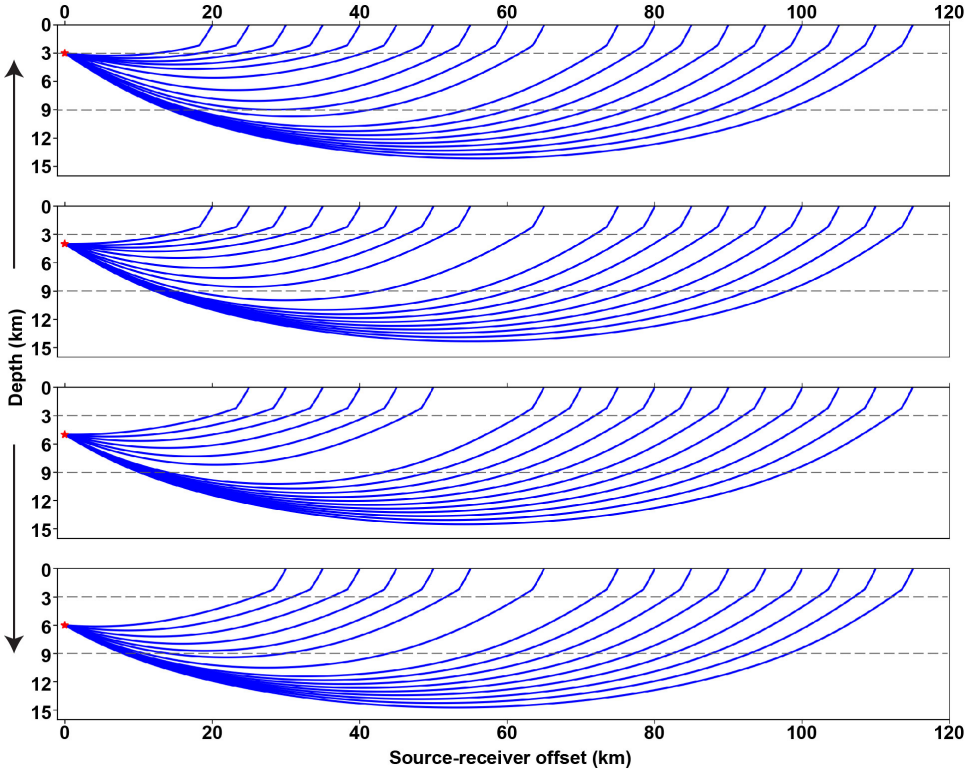


Figure S2.23: Ray paths computed for earthquake depth of 3km, 4km, 5km, and 6km (top to bottom), for an averaged 1-D velocity model of the crust. For this model basement depth is assumed at 2.2 km. It is evident from the ray path geometries that for source-receiver offset greater than ∼65km, ray paths sample depths greater than 10km. So, the assumption of Pei et al. (2018) to average velocities for 5-10 km depth, derived from offsets as far as 120-130 km could introduce a bias in their model.

Bibliography

Agena, W. F., Lee, M. W., and Grow, J. A. (1989). Reprocessing of the CO-CORP data recorded across the Wichita Mountain uplift and the Anadarko basin in southern Oklahoma. Technical report.

Amato, J. M., Heizler, M. T., Boullion, A. O., Sanders, A. E., Toro, J., McLemore, V. T., and Andronicos, C. L. (2011). Syntectonic 1.46 Ga magmatism and rapid cooling of a gneiss dome in the southern Mazatzal Province: Burro Mountains, New Mexico. *Geological Society of America Bulletin*, 123(9-10):1720–1744.

Anderson, J. and Bender, E. (1989). Nature and origin of Proterozoic A-type granitic magmatism in the southwestern United States of America. *Lithos*, 23(1-2):19–52.

Astiz, L., Earle, P., and Shearer, P. (1996). Global Stacking of Broadband Seismograms. *Seismological Research Letters*, 67(4):8–18.

Behm, M. (2009). 3-D modelling of the crustal S -wave velocity structure from active source data: application to the Eastern Alps and the Bohemian Massif. *Geophysical Journal International*, 179(1):265–278.

Behm, M., Brückl, E., Chwatal, W., and Thybo, H. (2007). Application of stacking and inversion techniques to three-dimensional wide-angle reflection and refraction seismic data of the Eastern Alps. *Geophysical Journal International*, 170(1):275–298.

Bickford, M. E., Harrower, K. L., Hoppe, W. J., Nelson, B. K., Nusbaum, R. L., and Thomas, J. J. (1981). Rb-Sr and U-Pb geochronology and distribution of rock types in the Precambrian basement of Missouri and Kansas. *Geological Society of America Bulletin*, 92:323–341.

Bickford, M. E. and Lewis, R. D. (1979). U-Pb geochronology of exposed basement rocks in Oklahoma. *Geological Society of America Bulletin*, 90(6):540.

Bickford, M. E., Van Schmus, W., Karlstrom, K., Mueller, P., and Kamenov, G. (2015). Mesoproterozoic-trans-Laurentian magmatism: A synthesis of continent-wide age distributions, new SIMS U–Pb ages, zircon saturation temperatures, and Hf and Nd isotopic compositions. *Precambrian Research*, 265:286–312.

Bickford, M. E., Van Schmus, W. R., and Zietz, I. (1986). Proterozoic history of the midcontinent region of North America. *Geology*, 14(6):492.

Braeuer, B., Asch, G., Hofstetter, R., Haberland, C., Jaser, D., El-Kelani, R., and Weber, M. (2012). High-resolution local earthquake tomography of the southern Dead Sea area. *Geophysical Journal International*, 191(3):881–897.

Brewer, J. A., Brown, L. D., Steiner, D., Oliver, J. E., Kaufman, S., and Denison, R. E. (1981). Proterozoic basin in the southern Midcontinent of the United States revealed by COCORP deep seismic reflection profiling. *Geology*, 9(12):569.

Brewer, J. A., Good, R., Oliver, J. E., Brown, L. D., and Kaufman, S. (1983). COCORP profiling across the Southern Oklahoma aulacogen: Overthrusting of the Wichita Mountains and compression within the Anadarko Basin. *Geology*, 11(2):109.

Brewer, J. A., Good, R., Oliver, J. E., Brown, L. D., and Kaufman, S. (1984). COCORP deep seismic reflection traverse across the southern Oklahoma Aulacogen. *Technical Proceedings of the 1981 AAPG Mid-Continent Regional Meeting, 1984*, pages 191–194.

Brewer, J. A. and Oliver, J. E. (1980). Seismic reflection studies of deep crustal structure. *Annual Review of Earth and Planetary Sciences*, 8(205-230).

Buckey, A. (2012). An integrated geophysical analysis of crustal structure in the Wichita Uplift region of southern Oklahoma. *The Shale Shaker*, 62(6):432–452.

Buehler, J. S. and Shearer, P. M. (2013). Sn propagation in the Western United States from common midpoint stacks of USArray data. *Geophysical Research Letters*, 40(23):6106–6111.

Campbell, J. A. and Weber, J. L. (2006). Wells drilled to basement to basement in Oklahoma. *Oklahoma Geological Survey Special Publication 2006-1.*

Chen, C. (2016). *Comprehensive analysis of Oklahoma earthquakes: from earthquake monitoring to 3D tomography and relocation.* PhD thesis, University of Oklahoma.

Chichester, B., Rychert, C., Harmon, N., Lee, S., Frederiksen, A., and Zhang, H. (2018). Seismic Imaging of the North American Midcontinent Rift Using S -to- P Receiver Functions. *Journal of Geophysical Research: Solid Earth*, 123(9):7791–7805.

Chopra, S., Marfurt, K. J., Kolawole, F., and Carpenter, B. M. (2018). Nemaha Strike-Slip Fault Expression on 3-D Seismic Data in SCOOP Trend. *AAPG Explorer*, (June):18–19.

Christensen, N. I. and Mooney, W. D. (1995). Seismic velocity structure and composition of the continental crust: A global view. *Journal of Geophysical Research*, 100(B6):9761–9788.

Darold, A. P., Holland, A. A., Jennifer, K., and Gibson, A. R. (2015). Oklahoma Earthquake Summary Report 2014. Technical report.

Denison, R. E., Lidiak, E. G., Bickford, M. E., and Kisvarsanyi, E. B. (1984). Geology and geochronology of Precambrian rocks in the Central Interior region of the United States. *US Geological Survey Professional Paper*, 1241 C:1–13.

Eberhart-Phillips, D. and Michael, A. J. (1998). Seismotectonics of the loma prieta, california, region determined from three-dimensional v p, v p/v s, and seismicity. *Journal of Geophysical Research: Solid Earth*, 103(B9):21099–21120.

Elebiju, O. O., Matson, S., Randy Keller, G., and Marfurt, K. J. (2011). Integrated geophysical studies of the basement structures, the Mississippi chert, and the Arbuckle Group of Osage County region, Oklahoma. *AAPG Bulletin*, 95(3):371–393.

Ellsworth, W. L. (2013). Injection-Induced Earthquakes. *Science*, 341(6142):1225942–1225942.

Evanzia, D., Pulliam, J., Ainsworth, R., Gurrola, H., and Pratt, K. (2014). Seismic Vp & Vs tomography of Texas & Oklahoma with a focus on the Gulf Coast margin. *Earth and Planetary Science Letters*, 402(C):148–156.

Frost, C. D. and Frost, B. R. (2011). On Ferroan (A-type) Granitoids: their Compositional Variability and Modes of Origin. *Journal of Petrology*, 52(1):39–53.

Frost, C. D. and Frost, B. R. (2013). Proterozoic ferroan feldspathic magmatism. *Precambrian Research*, 228:151–163.

Gajewski, D. and Pšenčik, I. (1987). Computation of high-frequency seismic wavefields in 3-D laterally inhomogeneous anisotropic media. *Geophysical Journal International*, 91(2):383–411.

Gajewski, D. and Pšenčík, I. (1989). Ray synthetic seismograms in 3-d laterally inhomogeneous anisotropic structures-program anray89. *LBL Center for Computational Seismology, Berkeley, CA*.

Garner, D. L. and Turcotte, D. L. (1984). The thermal and mechanical evolution of the Anadarko basin. *Tectonophysics*, 107(1-2):1–24.

Gilbert, M., Denison, R., Reed, J., Bickford, M., Houston, R., Link, P., Rankin, D., Sims, P., and Van Schmus, W. (1993). Late proterozoic to early cambrian basement of oklahoma. *Reed JC, Bickford ME, Houston RS, and four others, eds., Precambrian: Conterminous US: Boulder, Colorado, Geological Society of America, The Geology of North America*, 2:303–314.

Goodge, J. W. and Vervoort, J. D. (2006). Origin of Mesoproterozoic A-type granites in Laurentia: Hf isotope evidence. *Earth and Planetary Science Letters*, 243(3-4):711–731.

Hinze, W. J., Allen, D. J., Braile, L. W., and Mariano, J. (1997). The Mid-continent Rift System: A major Proterozoic continental rift. In *Middle Proterozoic to Cambrian rifting, central North America*, volume 312, pages 7–35. Geological Society of America.

Hole, J. (1992). Nonlinear high-resolution three-dimensional seismic travel time tomography. *Journal of Geophysical Research: Solid Earth*, 97(B5):6553–6562.

Johnson, K. (2008). Geologic History of Oklahoma. *Educational Publication*, 9:3–8.

Karlstrom, K. E., Whitmeyer, S. J., Dueker, K., Williams, M. L., Bowring, S. A., Levander, A. R., Humphreys, E. D., and Keller, G. R. (2005). Synthesis of results from the CD-ROM Experiment: 4-D image of the lithosphere beneath the Rocky Mountains and implications for understanding the evolution of continental lithosphere. In *Geophysical Monograph Series*, volume 154, pages 421–441.

Karlstrom, K. E., Åhäll, K.-I., Harlan, S. S., Williams, M. L., McLelland, J., and Geissman, J. W. (2001). Long-lived (1.8–1.0 ga) convergent orogen in southern laurentia, its extensions to australia and baltica, and implications for refining rodinia. *Precambrian Research*, 111(1):5 – 30.

Keller, G., Lidiak, E., Hinze, W., and Braile, L. (1983). The Role of Rifting in the Tectonic Development of the Midcontinent, U.S.A. In *Tectonophysics*, volume 94, pages 391–412.

Keranen, K. M., Weingarten, M., Abers, G. A., Bekins, B. A., and Ge, S. (2014). Sharp increase in central Oklahoma seismicity since 2008 induced by massive wastewater injection. *Science*, 345(6195):448–451.

Kissling, E., Ellsworth, W. L., Eberhart-Phillips, D., and Kradolfer, U. (1994). Initial reference models in local earthquake tomography. *Journal of Geophysical Research: Solid Earth*, 99(B10):19635–19646.

Kolawole, F., Simpson Turko, M., and Carpenter, B. M. (2020). Basement-controlled deformation of sedimentary sequences, Anadarko Shelf, Oklahoma. *Basin Research*, (August 2019):bre.12433.

Lidiak, E. G. (1996). Geochemistry of subsurface Proterozoic rocks in the eastern Midcontinent of the United States: Further evidence for a within-

plate tectonic setting. In *Basement and basins of eastern North America*, volume 308, pages 45–66. Geological Society of America.

Loidl, B., Behm, M., Thybo, H., and Stratford, W. (2014). Three-dimensional seismic model of crustal structure in Southern Norway. *Geophysical Journal International*, 196(3):1643–1656.

Lynn, H. B., Hale, L. D., and Thompson, G. A. (1981). Seismic reflections from the basal contacts of batholiths. *Journal of Geophysical Research: Solid Earth*, 86(B11):10633–10638.

Majdański, M., Grad, M., Guterch, A., Group, S. . W., et al. (2006). 2-d seismic tomographic and ray tracing modelling of the crustal structure across the sudetes mountains basing on sudetes 2003 experiment data. *Tectonophysics*, 413(3-4):249–269.

McBride, J. H., William Keach, R., Leetaru, H. E., and Smith, K. M. (2018). Visualizing Precambrian basement tectonics beneath a carbon capture and storage site, Illinois Basin. *Interpretation*, 6(2):T257–T270.

McGlannan, A. J. and Gilbert, H. (2016). Crustal signatures of the tectonic development of the North American midcontinent. *Earth and Planetary Science Letters*, 433:339–349.

Meissner, R., Marshall, J., and Plumb, R. A. (1986). *The continental crust: a geophysical approach*, volume 34. Academic Press.

Mitchell, B. and Landisman, M. (1970). Interpretation of a crustal section across Oklahoma. *Geological Society of America Bulletin*, 81:2647–2656.

Muehlberger, W. R., Denison, R. E., and Lidiak, E. G. (1967). Basement Rocks in Continental Interior of United States. *AAPG Bulletin*, 51(12):2351–2380.

Muehlberger, W. R., Hedge, C. E., Denison, R. E., and Marvin, R. F. (1966). Geochronology of the midcontinent region, United States: 3. Southern area. *Journal of Geophysical Research*, 71(22):5409–5426.

Murray, K. E. (2014). Class ii underground injection control well data for 2010–2013 by geologic zones of completion, oklahoma. *Oklahoma Geological Survey Open File Report OF1*, 32.

Nelson, B. K. and DePaolo, D. J. (1985). Rapid production of continental crust 1.7 to 1.9 b.y. ago: Nd isotopic evidence from the basement of the North American mid-continent. *Geological Society of America Bulletin*, 96(6):746.

Northcutt, R. A. and Campbell, J. A. (1996). Geologic Provinces of Oklahoma. *Shale Shaker*.

Oeberseder, T., Behm, M., Kovács, I., and Falus, G. (2011). A seismic discontinuity in the upper mantle between the eastern alps and the western carpathians: Constraints from wide angle reflections and geological implications. *Tectonophysics*, 504(1):122 – 134.

Pei, S., Chen, Y. J., Feng, B., Gao, X., and Su, J. (2013). High-resolution seismic velocity structure and azimuthal anisotropy around the 2010 Ms=7.1 Yushu earthquake, Qinghai, China from 2D tomography. *Tectonophysics*, 584:144–151.

Pei, S., Peng, Z., and Chen, X. (2018). Locations of Injection-Induced Earthquakes in Oklahoma Controlled by Crustal Structures. *Journal of Geophysical Research: Solid Earth*, 123(3):2332–2344.

Phinney, R. A. and Jurdy, D. M. (1979). Seismic imaging of deep crust. *Geophysics*, 44(10):1637–1660.

Pratt, T. L., Hauser, E. C., and Nelson, K. D. (1992). Widespread buried precambrian layered sequences in the midcontinent- evidence for large proterozoic depositional basins. *AAPG Bulletin*, 76(9):1384–1401.

Qin, Y., Chen, X., Carpenter, B. M., and Kolawole, F. (2018). Coulomb Stress Transfer Influences Fault Reactivation in Areas of Wastewater Injection. *Geophysical Research Letters*, 45(20):059–11.

Qin, Y., Chen, X., Walter, J. I., Haffener, J., Trugman, D. T., Carpenter, B. M., Weingarten, M., and Kolawole, F. (2019). Deciphering the Stress State of Seismogenic Faults in Oklahoma and Southern Kansas Based on an Improved Stress Map. *Journal of Geophysical Research: Solid Earth*, 124(12):12920–12934.

Rawlinson, N. and Sambridge, M. (2003). Seismic traveltime tomography of the crust and lithosphere. In *Advances in Geophysics*, volume 46, pages 81–198.

Schoenball, M. and Ellsworth, W. L. (2017). Waveform-Relocated Earthquake Catalog for Oklahoma and Southern Kansas Illuminates the Regional Fault Network. *Seismological Research Letters*, 88(5):1252–1258.

Shah, A. K. and Keller, G. R. (2017). Geologic influence on induced seismicity: Constraints from potential field data in Oklahoma. *Geophysical Research Letters*, 44(1):152–161.

Shaw, C. A., Heizler, M. T., and Karlstrom, K. E. (2005). 40Ar/39Ar thermochronologic record of 1.45–1.35 Ga intracontinental tectonism in the southern Rocky Mountains: Interplay of conductive and advective heating with intracontinental deformation. In *Geophysical Monograph Series*, volume 154, pages 163–184.

Shen, W. and Ritzwoller, M. H. (2016). Crustal and uppermost mantle structure beneath the United States. *Journal of Geophysical Research: Solid Earth*, 121(6):4306–4342.

Shen, W., Ritzwoller, M. H., and Schulte-Pelkum, V. (2013). Crustal and uppermost mantle structure in the central U.S. encompassing the Midcontinent Rift. *Journal of Geophysical Research: Solid Earth*, 118(8):4325–4344.

Sims, P. K., Saltus, R. W., and Anderson, E. D. (2005). Structure Map of the Continental United States – An Interpretation of Geologic and Aeromagnetic Data of the Continental United States — an Interpretation of Geologic and Aeromagnetic Data. *U.S. Geological Survey Open-file report 2005-1029*, page 29.

Slagstad, T., Culshaw, N. G., Daly, J. S., and Jamieson, R. A. (2009). Western Grenville Province holds key to midcontinental Granite-Rhyolite Province enigma. *Terra Nova*, 21(3):181–187.

Snelson, C. M., Henstock, T. J., Keller, G. R., Miller, K. C., and Levander, A. (1998). Crustal and uppermost mantle structure along the Deep Probe seismic profile. *Rocky Mountain Geology*, 33(2):181–198.

Stein, C. A., Kley, J., Stein, S., Hindle, D., and Keller, G. R. (2015). North America's Midcontinent Rift: When rift met LIP. *Geosphere*, 11(5):1607–1616.

Stein, C. A., Stein, S., Elling, R., Keller, G. R., and Kley, J. (2018a). Is the "grenville front" in the central united states really the midcontinent rift? *GSA Today*, 28(5):4–10.

Stein, C. A., Stein, S., Merino, M., Randy Keller, G., Flesch, L. M., and

Jurdy, D. M. (2014). Was the Midcontinent Rift part of a successful seafloor-spreading episode? *Geophysical Research Letters*, 41(5):1465–1470.

Stein, S., Stein, C., Kley, J., Keller, R., Merino, M., Wolin, E., Wiens, D., Wysession, M., Al-Equabi, G., Shen, W., Frederiksen, A., Darbyshire, F., Jurdy, D., Waite, G., Rose, W., Vye, E., Rooney, T., Moucha, R., and Brown, E. (2016). New Insights into North America's Midcontinent Rift. *Eos*, 97(August):1–8.

Stein, S., Stein, C. A., Elling, R., Kley, J., Keller, G. R., Wysession, M., Rooney, T., Frederiksen, A., and Moucha, R. (2018b). Insights from north america's failed midcontinent rift into the evolution of continental rifts and passive continental margins. *Tectonophysics*, 744:403–421.

Stratford, W. and Thybo, H. (2011). Seismic structure and composition of the crust beneath the southern scandes, norway. *Tectonophysics*, 502(3):364 – 382.

Tave, M. A. (2013). *Imaging of the crust and Moho beneath Oklahoma using receiver functions and Pn tomography; with emphasis on the Southern Oklahoma Aulacogen*. PhD thesis.

Thomas, W. A. (1991). The appalachian-ouachita rifted margin of southeastern north america. *Geological Society of America Bulletin*, 103(3):415–431.

Thurber, C. (1993). Local earthquake tomography: velocities and v_p/v_s-theory. *Seismic tomography: theory and practice*, pages 563–583.

Thybo, H. and Artemieva, I. (2013). Moho and magmatic underplating in continental lithosphere. *Tectonophysics*, 609:605–619.

Thybo, H., Sandrin, A., Nielsen, L., Lykke-Andersen, H., and Keller, G. (2006). Seismic velocity structure of a large mafic intrusion in the crust of central Denmark from project ESTRID. *Tectonophysics*, 420(1-2):105–122.

Tong, P., Yang, D., Li, D., and Liu, Q. (2017). Time-evolving seismic tomography: The method and its application to the 1989 loma prieta and 2014 south napa earthquake area, california. *Geophysical Research Letters*, 44(7):3165–3175.

Toth, C. R. (2014). *Separation of the Earthquake Tomography Inverse Problem to Refine Hypocenter Locations and Tomographic Models: A Case Study from Central Oklahoma*. PhD thesis, University of Oklahoma.

Tryggvason, E. and Qualls, B. R. (1967). Seismic refraction measurements of crustal structure in Oklahoma. *Journal of Geophysical Research*, 72(14):3738–3740.

Van Schmus, W. R., Bickford, M. E., and Turek, A. (1996). Proterozoic geology of the east-central Midcontinent basement. In *Basement and basins of eastern North America*, volume 308, pages 7–32. Geological Society of America.

Van Schmus, W. R. and Hinze, W. J. (1985). The Midcontinent Rift System. *Annual Review of Earth and Planetary Sciences*, 13(1):345–383.

Weingarten, M., Ge, S., Godt, J. W., Bekins, B. A., and Rubinstein, J. L. (2015). High-rate injection is associated with the increase in u.s. midcontinent seismicity. *Science*, 348(6241):1336–1340.

Whitmeyer, S. J. and Karlstrom, K. E. (2007). Tectonic model for the Proterozoic growth of North America. *Geosphere*, 3(4):220–259.

Woelk, T. S. and Hinze, W. J. (1991). Model of the midcontinent rift system in northeastern Kansas. *Geology*, 19(3):277.

Zhang, H., Lee, S., Wolin, E., Bollmann, T. A., Revenaugh, J., Wiens, D. A., Frederiksen, A. W., Darbyshire, F. A., Aleqabi, G. I., Wysession, M. E., Stein, S., and Jurdy, D. M. (2016). Distinct crustal structure of the North American Midcontinent Rift from P wave receiver functions. *Journal of Geophysical Research: Solid Earth*, 121(11):8136–8153.

Zhu, H. (2018). Crustal wave speed structure of North Texas and Oklahoma based on ambient noise cross-correlation functions and adjoint tomography. *Geophysical Journal International*, 214(1):716–730.

Zhu, X. and McMechan, G. A. (1989). 2-D tomographic imaging of velocities in the Wichita uplift-Anadarko basin region of southwestern Oklahoma. *Bulletin of the Seismological Society of America*, 79(3):873–887.

Chapter 3

Shear wave velocity structure and compositional analysis of the crustal structure in Oklahoma

3.1 Abstract

Induced seismicity in Oklahoma along with the extensive seismic networks installed for earthquake monitoring turned out to be an unintended but unique large-scale seismic experiment. We use the rich catalog of local earthquake waveforms to obtain a S-wave crustal velocity model for Oklahoma. In combination with a recently established P-wave velocity model, our study informs the processes that led to the Mesoproterozoic lithospheric expansion of Laurentia and provides insights on local crustal structures. We use the data recorded for 27,582 earthquake events at 10 seismic networks across Oklahoma spanning a period of 2010 to 2017. To focus on the deeper crustal features, we use an alternative approach to process horizontal component data. Processing includes band-pass filtering, conversion to envelope, and STA/LTA detection. Common-mid-point sorted data are stacked in offset bins and are representa-

tive of local 1D velocity-depth functions. This approach results in a significant increase in S/N ratio which allows for picking of Sg 1-D travel time curves for larger offset ranges. The 1-D travel time curves are then inverted and combined to obtain a 3-D S-wave crustal velocity model. We combine the Sg velocity model with the Pg velocity model to obtain Poisson's ratio. Our results are integrated with regional gravity data and we discuss the geologic implications of our model in terms of crustal composition and evolution.

3.2 Introduction

Precambrian rocks in the North American midcontinent contain a wealth of information regarding the processes that led to the assembly of the North American continental lithosphere. The basement rocks of Oklahoma belong to the Southern Granite-Rhyolite Province (SGRP) and were formed ∼1.35 Ga ago. Petrological studies of the Precambrian rocks in Oklahoma have been limited to samples obtained through drill cuttings and the two known exposures (Spavinaw, (northeast) OK and Arbuckle mountains, (southeast) OK) (Bickford et al., 1981; Bickford and Lewis, 1979; Denison et al., 1984; Lidiak, 1996; Nelson and DePaolo, 1985). These studies have been crucial in understanding the composition and age of the rocks. However, these studies only provide observations for the upper crust in Oklahoma and with the lack of exposures of deeper crustal rocks, we are limited in our understanding of the crustal composition in Oklahoma.

Compressional and shear wave velocities are some of the fundamental properties of rocks. At given pressure-temperature conditions, both compressional (P) and shear (S) wave velocities are largely controlled by the mineral composition of the rock (Christensen, 1996). Several new S-wave velocity models

are available for Oklahoma based on ambient noise recorded at the Earthscope US Transportable Array stations (Evanzia et al., 2014; Marsh, 2018; Shen and Ritzwoller, 2016; Zeng and Nowack, 2021; Zhu, 2018). These S-wave velocity models focus on imaging large scale crustal features in Oklahoma but lack the resolution needed to investigate local anomalies in the region. The vast majority of the seismic studies in Oklahoma focus on the development of either P or S wave velocity models and subsequently lack discussion of the crustal composition in Oklahoma. P or S wave velocities alone are not deterministic to establish rock types, but the V_P/V_S ratio or Poisson's ratio can provide better constraints on crustal composition (Christensen, 1996; Holbrook et al., 1992b; Musacchio et al., 1997). In Oklahoma, a few studies have calculated V_P/V_S ratios through receiver function and Moho reflection based studies. These provide an average V_P/V_S ratio at a given location for the entire crust which does not provide enough constraints to determine crustal composition.

In this study we present a 3-D S wave velocity model for central Oklahoma for the entire crust using a nonstandard methodology. We use the local induced earthquake data recorded at the broadband stations across the state of Oklahoma, including both regional monitoring stations and the Earthscope US Transportable Array stations. These local earthquake waveforms are processed using common mid-point (CMP) based stacking and inversion technqiue. This methodology has been successfully applied to develop a 3-D P wave velocity model for central Oklahoma (Ratre and Behm, 2021). We combine the two velocity models to determine the V_P/V_S and Poisson's ratio to infer the crustal composition in Oklahoma. Utilizing models from the same data sets and identical methodologies reduces uncertainty in the final V_P/V_S model. Our results indicate a K - rich felsic upper crust that transitions into intermediate and mafic rocks dominant in plagioclase and pyroxene.

3.3 Previous Seismic Studies

There is a long history of geophysical studies in Oklahoma to understand the shallow crustal structures. Some of the earliest studies that provide an insight into the crustal features were 2-D deep crustal active seismic surveys (e.g. Tryggvason and Qualls, 1967; Mitchell and Landisman, 1970; Agena et al., 1989; Brewer et al., 1983, 1984; Brewer and Oliver, 1980; Phinney and Jurdy, 1979; Zhu and McMechan, 1989, and others). These studies focused on 2-D P-wave velocity structure featuring a high velocity (V_P >7.0 km/s) lower crust and provided an early estimate of the Moho depth to be about 46 km in Oklahoma. In recent years, increased seismicity in Oklahoma has led to several passive seismic studies that explore P and S velocity structures in Oklahoma (Chen, 2016; Toth, 2014; Pei et al., 2018; Marsh, 2018). Marsh (2018) performed ambient noise tomography to obtain a shear wave velocity model for Oklahoma up to depths of 20 km. These studies have increased our understanding of the upper crustal structure but lack significant information about the deeper crust in Oklahoma. Evanzia et al. (2014) performed teleseismic tomography to explore the P and S wave velocity structures in the crust and upper mantle for Oklahoma and Texas. They are one of the few studies that highlight the tectonic features preserved in the upper mantle but lack information about crustal-scale features due to low resolution of their model. Shen and Ritzwoller (2016) obtained shear wave velocity structure for the crust and uppermost mantle for the contiguous United States based on measurements from ambient noise, earthquakes, receiver functions, and Rayleigh wave ellipticity measurements. Zhu (2018) developed a deeper crust 3-D shear wave velocity model for Oklahoma and north Texas using ambient noise cross-correlation and adjoint tomography representing the shear wave velocities up to depths of 40 km. While Zhu (2018)'s model provides more details with regards to the

crustal structures present in Oklahoma, there are significant discrepancies between Zhu (2018) and Shen and Ritzwoller (2016) with regards to the average shear wave velocities observed in their models which could be attributed to the differences in their data and methodologies. More recently Tan et al. (2021) produced a crustal scale 3-D shear wave velocity model through joint inversion of ambient noise dispersion and P to S receiver functions. They compared their model with both Zhu (2018) and Shen and Ritzwoller (2016) and showed an improvement on the shear wave velocity estimates. Wang et al. (2019) developed V_P/V_S ratio and Moho depth map using P to S receiver functions and H-k stacking of teleseismic earthquakes recorded across Oklahoma. Zeng and Nowack (2021) also provide V_P/V_S ratio estimates for crust in northern Oklahoma. Both of these studies show a V_P/V_S ratios >1.75 for Oklahoma indicating a faster, more mafic crust.

A new 3-D P-wave velocity model was developed using the same methodology as applied here in this study (Ratre and Behm, 2021). A high velocity (> 7 km/s) lower crust was reported for Oklahoma. This study will incorporate the P wave velocities from the previous study to infer the crustal composition and determine Poisson's ratio for the crust in Oklahoma.

3.4 Data and Methodology

3.4.1 Data

The exponential increase in the induced seismicity in Oklahoma in the past decade led to extensive installation of broadband monitoring stations across the state along with the coincidental deployment of the Earthscope US Transportable Array network. The local and transportable array recorded 27,568 events between January 2010 to September 2017 that occured in Oklahoma.

Details about the station and events used are given in Data set S1 and Data set S2 that can be downloaded from `https://github.com/pranshuratre/Oklahoma_station_event_data`. Figure 3.1 shows the locations of the stations and events used in this study. The earthquake catalogue used in this study is a combination of relocated catalogue by Schoenball and Ellsworth (2017) and HypoDD corrected catalogue (pers. comm. with Dr. Jefferson Chang). Most of the earthquakes in Oklahoma occur in the uppermost crust between 2-7 km. We select seismic traces from both horizontal components with a maximum epicentral distance of 250 km.

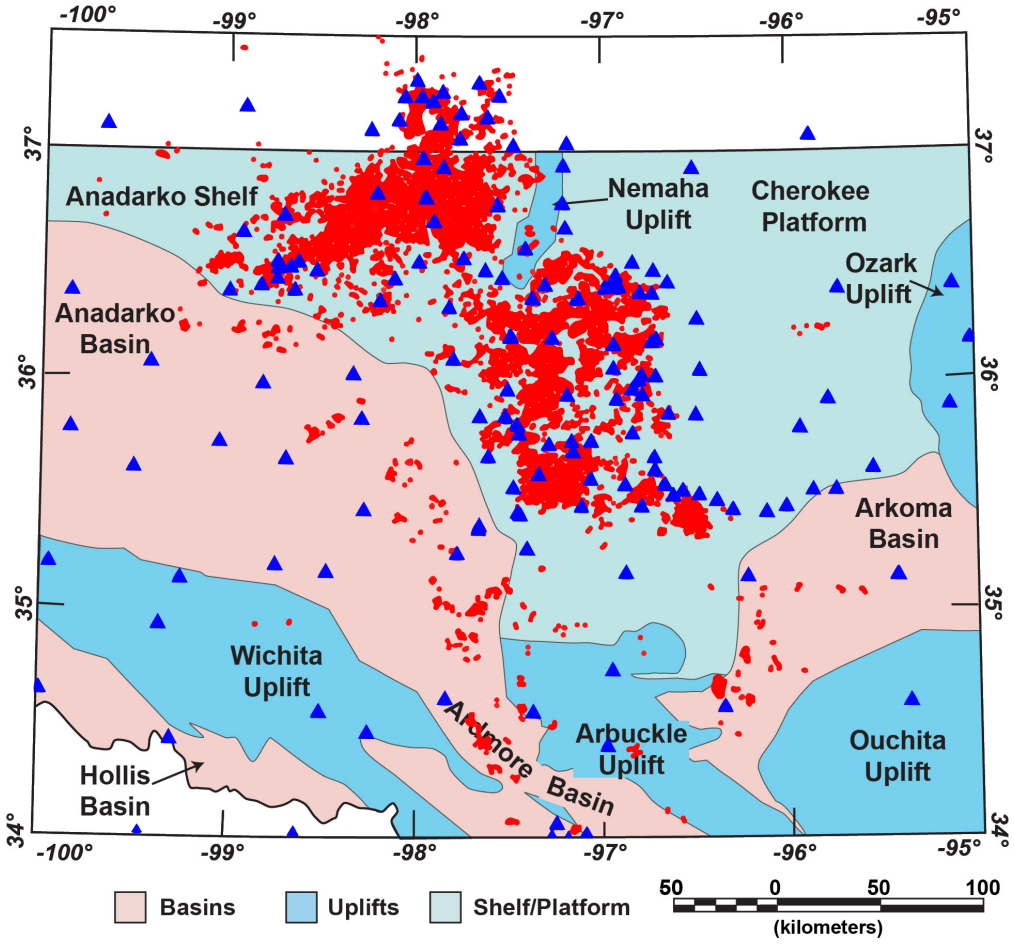


Figure 3.1: Red dots: location of earthquakes used in this study. Blue triangles: recording stations used in this study. Areas beyond the state of Oklahoma are in white.

3.4.2 Methodology

Our methodology is based on common-midpoint sorting and stacking of Sg waves, as has been applied to Pg waves in the same region by Ratre and Behm (2021). In the following, we only summarize the principal processing steps and specific processing parameter selections. The reader is referred to Ratre and Behm (2021) to a more detailed description and discussion of the methodology. Local earthquake tomography is contingent upon correct phase identification and correlation, which can be difficult in case of low signal-to-noise ratio especially for far-offset data. Our approach relies on simplifying the wavefield to reduce the uncertainties in phase correlation and increase the signal-to-noise ratio to obtain a deeper depth of investigation. This methodology involves an inherent assumption of laterally isotropic crust. We regard the earthquake source-receiver geometry as a 3-D active seismic dataset with an irregular geometry and apply active seismic processing techniques of common-mid point sorting and stacking to derive a 3-D S-wave velocity model. Since the data are recorded on three-component seismic stations, S wave arrivals are recorded at both the north and east components. Figure 3.2 shows bandpass filtered, LMO corrected horizontal components for two event gathers. Sg arrivals can be easily identified but the presence of noise and intermediate phases for some stations would increase the uncertainty in picking accurate phase arrival times. We combine the data from both north and east components to obtain 1,719,923 traces. To achieve a constructive interference while combining the two components, the traces are bandpass filtered with a wide frequency band (1-2-12-15 Hz) Ormsby filter, followed by conversion to envelope (modulus of the complex trace). The two component data for each event are stacked at each station to obtain a combined dataset.

Prior to any further processing, static and geometric corrections are ap-

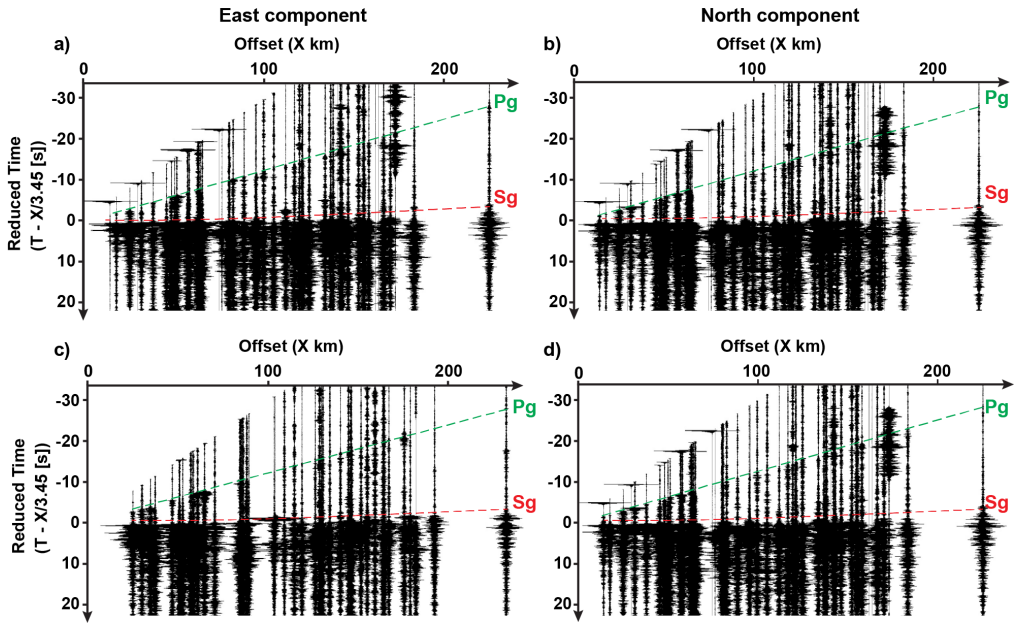


Figure 3.2: a,b) and c,d) show East and North component for two events respectively. The traces are bandpass filtered (4-6-10-12 Hz) and LMO corrected with a velocity of 3.45 km/s. (Note: These values are only used for visualization and not part of processing routine).

plied. Generally for active seismic data processing where the sources and receivers are located close to the surface, static corrections are applied to remove time delays caused by elevation differences, near-surface weathering effects, and/or the upper-most sedimentary layers. Passive seismic data derived from earthquakes adds variability in time delays due to differing earthquake depths. We apply time and geometric corrections to each trace based on the earthquake depth, source-receiver offset, basement structure at source and receiver, and the regional velocity structure. Final datum corrections move each source-receiver pair to an assumed datum level of 5 km. Datum level of 5 km is selected as majority of the earthquakes occur in the depth range of ∼5-7 km. We select data with high quality location estimates and cap the source-receiver offset of the new geometry to 250 km, which gives us a total of 688,000 traces. A top mute is applied to remove the Pg phases. The data are further

processed by applying minimum phase Ormsby filter with [0.5-2-4-6 Hz] corner frequencies to increase the S/N ratio of the data and to improve stacking. We further enhance the Sg phase arrivals through application of STA/LTA (short term average/long term average) ratio signal detection technique and apply a linear move-out (LMO) correction with a 3.45 km/s velocity. The averaging windows used for STA and LTA are 0.5 s and 5 s respectively. These pre-stack processing steps aim at minimizing the source and path effects and simplify the wavefield, thus facilitating a constructive stack of traces. Figure 3.3 shows an example of event gather after bandpass filter and STA/LTA application.

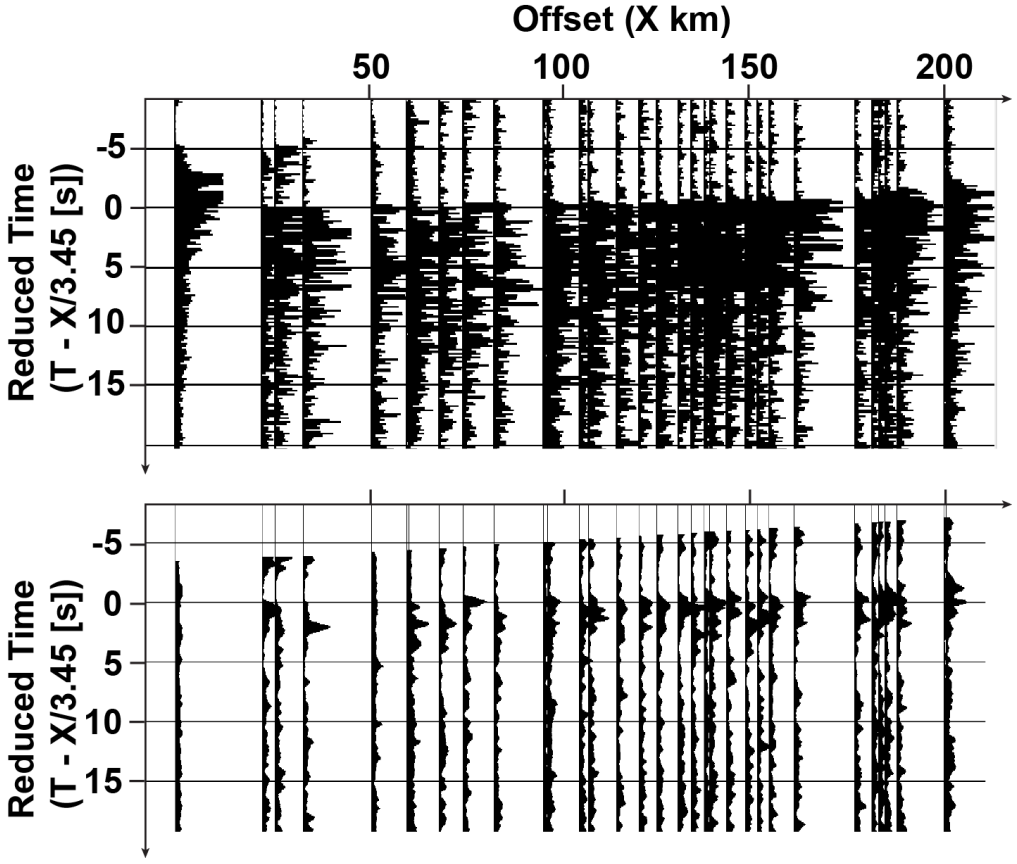


Figure 3.3: Example of preprocessing on one datum-corrected event gather with LMO correction applied for a velocity of 3.45 km/s. (a) Signal converted to envelope + bandpass filtered (0.5-2-4-6 Hz), (b) STA/LTA applied

The processed traces are sorted according to the source-receiver midpoint

locations into "common-mid-point" (CMP) cells and sorted according to offset within each cell to obtain a CMP gather. These cells occupy the study area such that the cell-centers form a regularly spaced grid with 20 km lateral spacing. The size of each individual cell depends on the number of traces in a particular cell and is varied between 20-70 km. We introduce a requirement of minimum 30 traces between 50-100 km in order to select a particular cell size. Appropriate cell sizes are selected when the above condition is met. The final location of each of these CMP cells are calculated as the mean location of all the trace mid-points that lie within the cell. The traces in each CMP bin are stacked in 5 km offset bins. Figure 3.4 shows the CMP cell size, number of traces in each cell, and the CMP bin center location. Each of the stacked traces are assigned an absolute offset value that is the average of the absolute offsets of all traces in each offset bin. Each offset-sorted stacked CMP gather represents 1-D travel time curve for the corresponding cell. The stacked traces in each CMP gather are manually picked to obtain 1-D travel time curves are picked for each stacked CMP gather and inverted to obtain a 1-D velocity-depth function at 116 CMP cell locations. Figure 3.5 shows the processing steps described above.

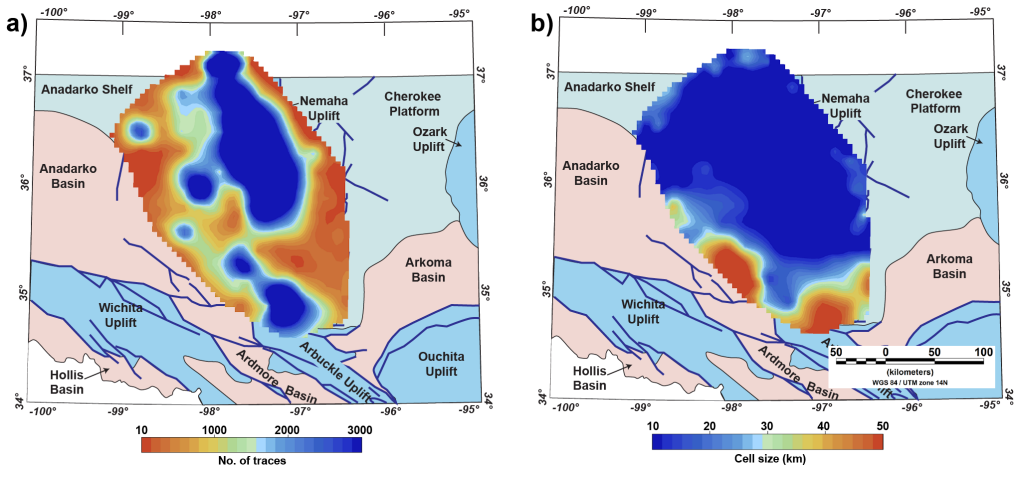


Figure 3.4: (a)Number of traces in each bin, (b)CMP bin size.

Initial velocity model for basement and below is derived from P-wave velocity model for shield and platform given by Christensen and Mooney (1995) using a V_P/V_S ratio of 1.73. We use a ray parameter weighted scheme Behm et al. (2007) to invert for the 1-D velocity - depth functions which also provides resolution elements as one of the outputs. Resolution elements provide confidence values to the corresponding velocity elements and vary between 0 (undetermined) to 1 (uniquely determined). The RMS travel time residuals are reduced from a range of 0.024 - 1 s with a mean of 0.25 for the initial velocity model to a range of 0.001 - 0.09 s with a mean of 0.026 for the final velocity model. Any velocity node with a resolution element value of less than 0.5 are discarded. We further exclude all CMP locations with an RMS travel time residual greater than 40 ms resulting in a combined reduction of 32% of the calculated velocity data points. We interpolate the 1-D velocity-depth functions from the remaining dataset to derive a 3-D velocity model for the study area through minimum-curvature interpolation method. The resulting 3-D velocity model (Figure 3.6) captures regional crustal structures up to depths of $\sim$35 km. Average velocities vary from 3.42 km/s at 5 km depth to 3.83 km/s at 39 km depth with overall minimum and maximum velocities of 3.16 km/s and 3.84 km/s, respectively. The average shear wave velocities for the crust in Oklahoma are lower than the shields and platform 1-D velocity model given by Christensen and Mooney (1995).

Figure 3.6 shows the combined velocity model as depth slices starting from 5 km to 30 km. Our velocity model starts at 5 km depth, where we have assumed our processing datum. Due to velocity increase with depth, we chose a depth-dependent color scale in Figure 3.6 to emphasize lateral variations at each depth. To analyze the velocity model in more detail we have highlighted regions (Figure 3.6, regions A, B, C) which show velocity anomalies that are

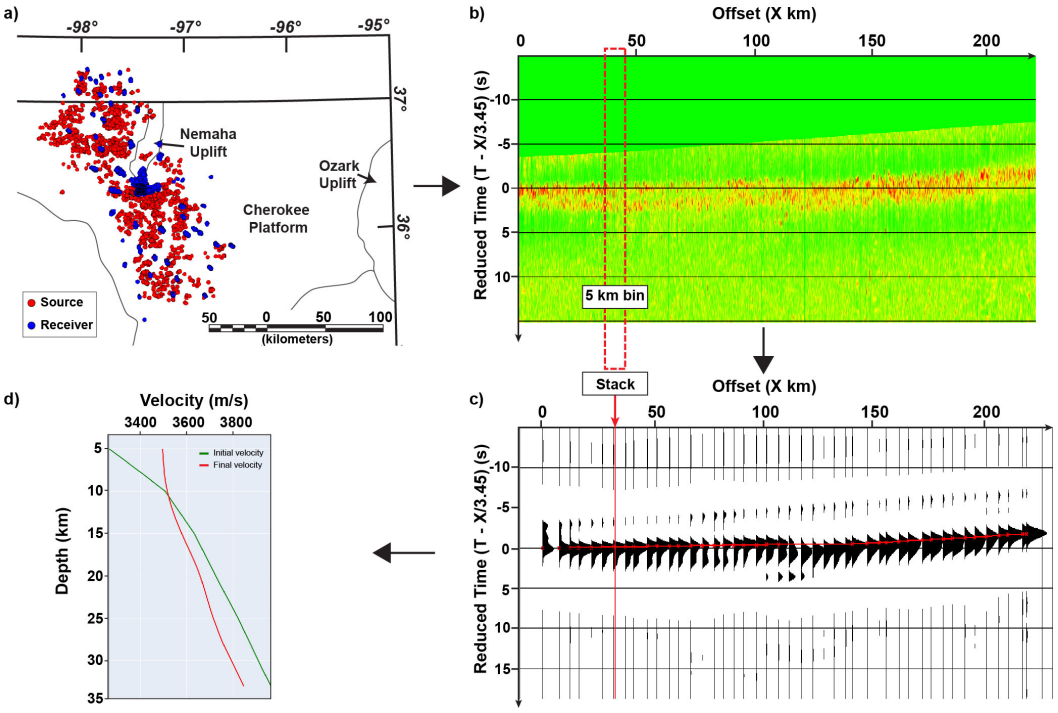


Figure 3.5: Processing steps illustrated for one CMP bin. (a) All source-receiver pairs shown for the CMP bin (black square); (b) Pre-processed earthquake waveforms in this CMP gather with a linear move-out correction of 3.45 km/s; (c) Stacked gather obtained from 5 km offset-bin stacking of sorted gather in (b), red dashed line shows the picked travel time curve; (d) Initial and inverted 1-D velocity model for the CMP bin location.

discussed in more detail in the next section. We also compute depth slices for V_P/V_S ratios (Figure 3.7) using the P-wave velocity model computed using using the same methodology as this study (Ratre and Behm, 2021). The average V_P/V_S for Oklahoma across the crust is greater than 1.77±1.

3.5 Discussion and Interpretation

3.5.1 Comparison with Existing Velocity Model

Recently, several shear wave velocity models have been published for the crust of Oklahoma that primarily utilize ambient noise data recorded at sta-

tions across the state of Oklahoma (Shen and Ritzwoller, 2016; Zhu, 2018; Tan et al., 2021). We compare our velocity model to the two existing local shear wave velocity models developed by Zhu (2018) and Tan et al. (2021). Figure 3.8 shows the average velocity variation for each of the velocity models with depth. Since the lateral coverage for our model only covers central Oklahoma, we only use velocity data points that represent the extent of our model. Ambient noise investigation relies on surface wave velocities to invert for shear wave velocities in the subsurface. Surface wave velocities are a function of data frequency, P- and S-wave velocities, and rock densities. Surface wave velocities are predominantly influenced by the S-wave velocities in the region. In case of short period surface waves, shallow crustal density plays a significant role and an incongruous density estimate can cause geologically unfit shear wave anomalies for middle to lower crustal depths (Xing et al., 2016). Depending on the frequency of data used one can determine the depth of investigation for ambient noise investigation. The frequency content of the data would also be influential in assessing the accuracy of shear wave velocities for the deeper crust derived from surface wave inversion.

Both Zhu (2018) and Tan et al. (2021) have low S-wave velocity estimates for the upper crust-middle crust (upto $\sim$12 km). As discussed above, this could be an effect of improper density estimates for the sedimentary basin that is causing anomalously low velocity estimates for these depths. Large station separation for deriving these velocity models also leads to a comparatively lower resolution than the velocity model presented in this study. Evidence for mafic intra-basement layers in the upper crust in Oklahoma is presented by various studies in the region (Elebiju et al., 2011; Kolawole et al., 2020; McBride et al., 2018; Ratre and Behm, 2021) but the ambient noise based velocity models (Zhu, 2018; Tan et al., 2021) do not give indication for such

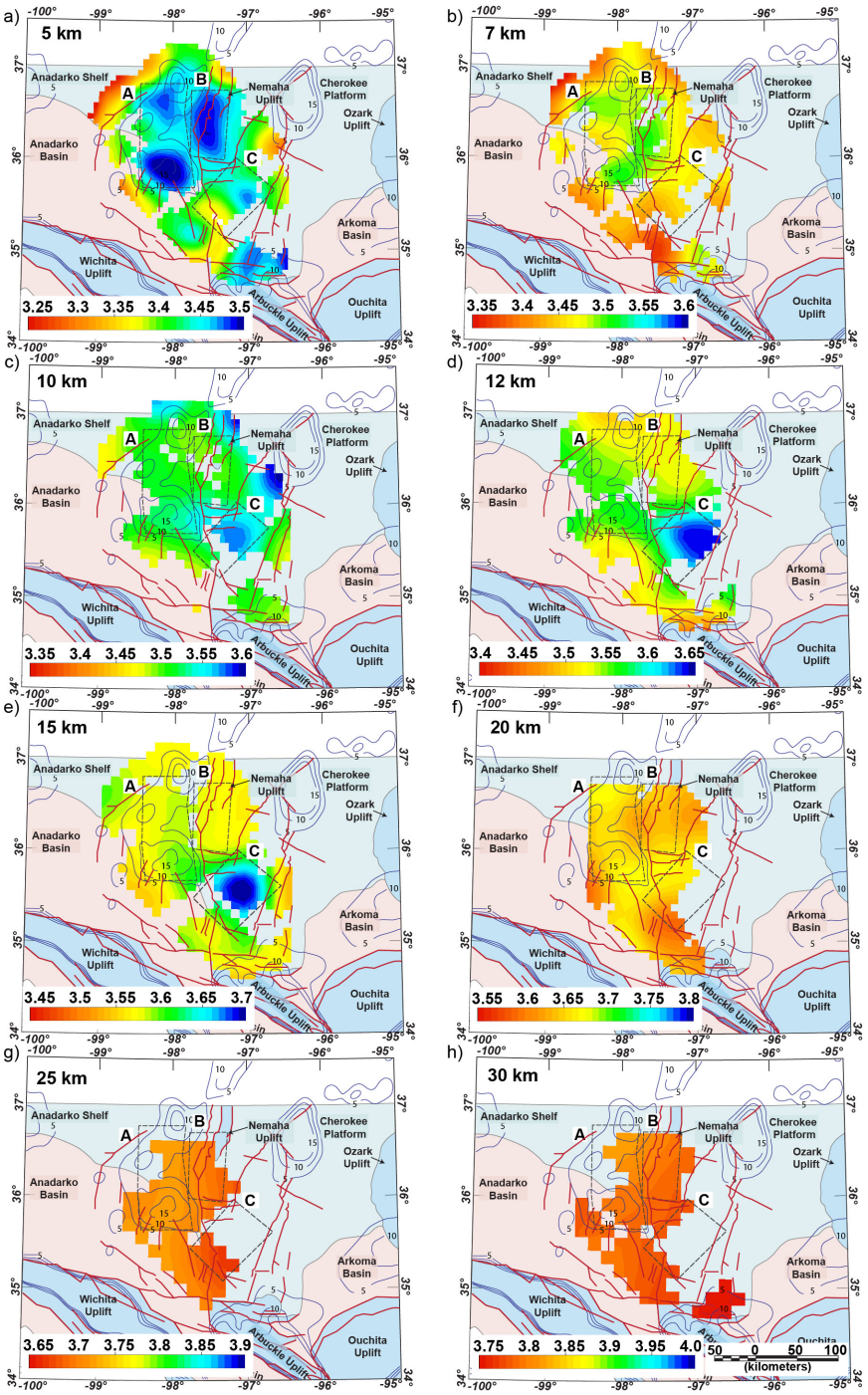


Figure 3.6: Horizontal slices through the 3-D Sg wave velocity model superimposed on the geologic provinces map. Note the varying color scale for each depth slice (same range of 250 m/s). Black contour lines show the Bouguer Gravity anomaly [mGal]. Regions A, B, and C are discussed in the text.

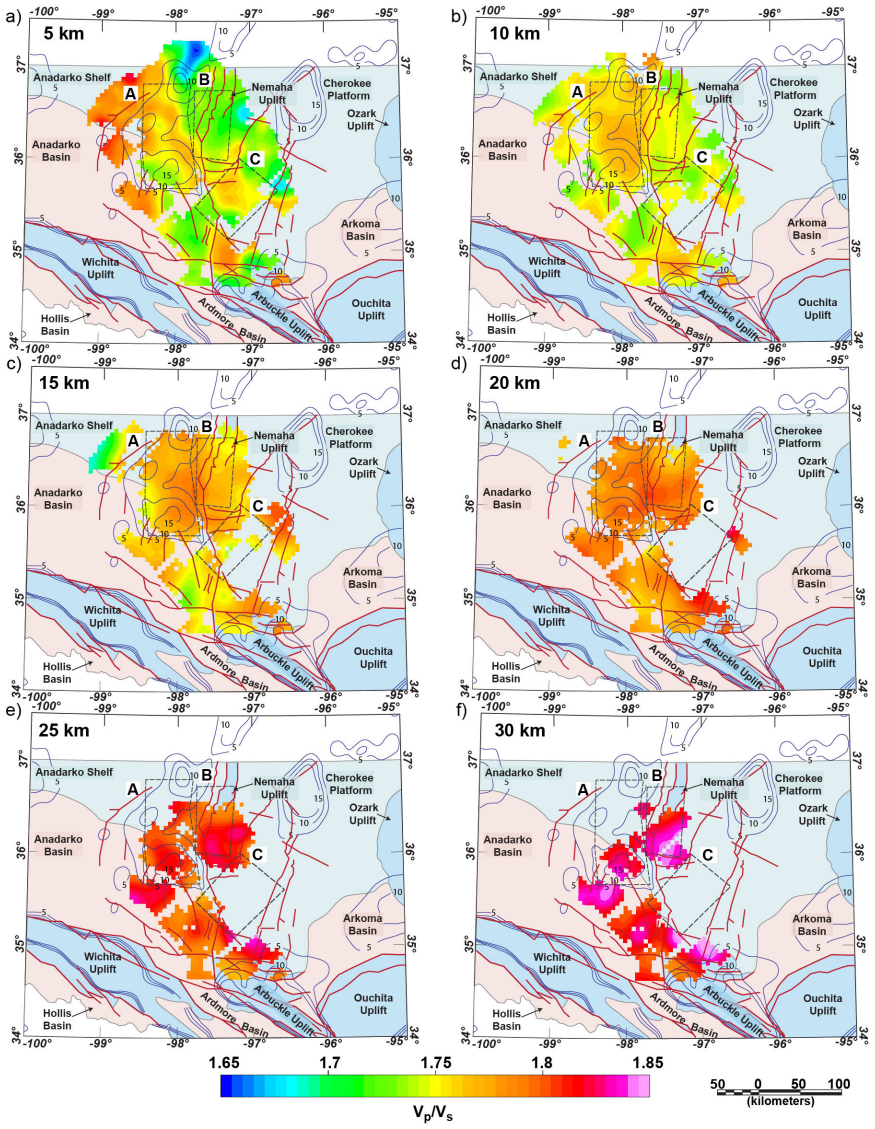


Figure 3.7: Horizontal slices through the 3-D Vp/Vs model superimposed on the geologic provinces map. Black contour lines show the Bouguer Gravity anomaly [mGal]. Regions A, B, and C are discussed in the text.

anomalies. Another point of deviation is the consistently high lower crustal velocities ($>$ 4.0 km/s) observed in shear wave velocity models by Shen and Ritzwoller (2016), Zhu (2018), and Tan et al. (2021) (Figure 3.6, 3.8). High shear wave velocities would imply V_P/V_S ratios of $<$ 1.75 which contradicts V_P/V_S estimates ($>$ 1.77) from Moho reflection and receiver function studies (McGlannan and Gilbert, 2016; Wang et al., 2019; Zeng and Nowack, 2021).

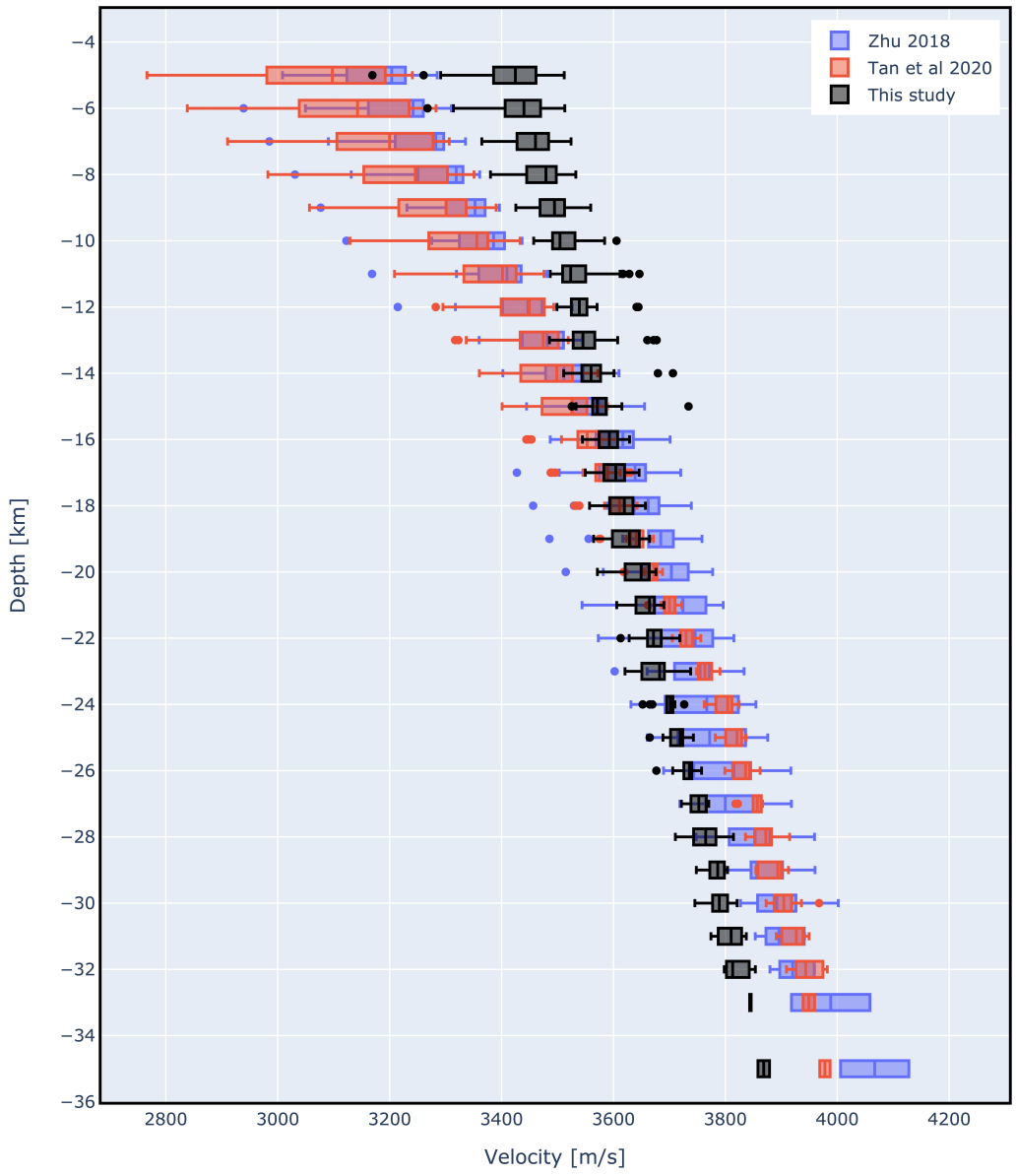


Figure 3.8: Box plot depicting the variation of Sg velocity with depth for central Oklahoma. Light blue: Zhu (2018), red: Tan et al. (2021), black: this study

Further, several studies have interpreted a mafic lower crust in Oklahoma based on high (> 7.0 km/s) P wave velocities observed in the region (Tryggvason and Qualls, 1967; Mitchell and Landisman, 1970; Brewer et al., 1984; Ratre and Behm, 2021). Velocities derived from ambient noise data inversion smears the velocities in lower crust and upper mantle which likely leads to the increased apparent shear wave velocities observed in the lower crust. The shear wave velocity model presented in this study shows less variation with increasing depth as compared to Zhu (2018)'s model. Tectonically, a homogeneous lower crust is more plausible as the crust is Oklahoma belongs to a stable shield and platform regime (Christensen and Mooney, 1995). As the stacking method inherently suppresses any outliers in the data, the shear wave velocity model for the crust developed in this study is a robust model without significant systematic biases.

3.5.2 Crustal Structures

S-wave velocity structure for the upper crust in Oklahoma depicts a heterogeneous crust. High S-wave velocity anomalies are observed in the upper crust in Region A (Figures 3.6,3.9). They appear to diminish in their intensity with depth and are non-existent by $\sim$15 km depth (Figure 3.9). Figures 3.6 show the correlation of these anomalies with the regional gravity highs in the region. We observe V_P/V_S ratio of > 1.75 in this region (Figure 3.7) which corroborates the presence of mafic intra-crustal layering in the basement rocks as suggested by previous studies in the region (Brewer et al., 1981, 1983, 1984; Buckey, 2012; Elebiju et al., 2011; Kolawole et al., 2020; McBride et al., 2018; Mitchell and Landisman, 1970; Ratre and Behm, 2021). A similar high velocity anomaly is reported by Shen and Ritzwoller (2016) in their mid-crustal ($>$ 5 km depth) shear wave velocity structure. While the region A anoma-

lies (Figure 3.6a,b,d,e, Region A) visually correlate with the gravity data, it is important to note that the variation in the velocities at 5 km depth layer is moderate with the minimum and maximum velocities being 3135 m/s and 3512 m/s, and mean and median values of 3403 m/s and 3414 m/s. This can also be seen in the cross section Figure 3.9a,b where the variation in the upper crustal layers is not as pronounced as it may appear in the depth slices.

Region B shows a significant high velocity anomaly close to the Nemaha fault zone at 5 km depth (Figure 3.6,a). The Vp/Vs ratio for Region B in the upper crust (5-10 km) are close to 1.73 (Figure 3.7) which suggests that the S wave velocity anomaly is not related to the presence of mafic material as mafic rocks have a higher V_P/V_S ratio ($>\sim$1.8). Cross-section in Figure 3.9a also suggests that the velocity anomaly is present in the upper most crust and its strength decreases rapidly with depth. Region C in the south-eastern part of our velocity model shows a high velocity anomaly that gets stronger with depth (Figure 3.6,3.9c). The sudden jump in velocity seem to coincide with the boundary between the Anadarko Basin and Cherokee Platform (Figure 3.9c). Similar high shear wave velocity anomalies are also observed at 15 km depth by Tan et al. (2021) that extend further south-east (outside the bounds of our data). To understand the origin of this anomaly we also compare our data to the local temperature - depth and heat flow maps (Blackwell et al., 2011). Low temperatures at mid-crustal depths and low heat flow to the surface is reported for the region where we see the high velocity anomaly. It is also noted that this positive Vs anomaly corresponds with a pronounced magnetic low (Figure 3.9a). The lower crust ($>$ 20km) in Oklahoma is more homogeneous as S-wave velocities show less variation through the study area (Figure 3.6f,g,h).

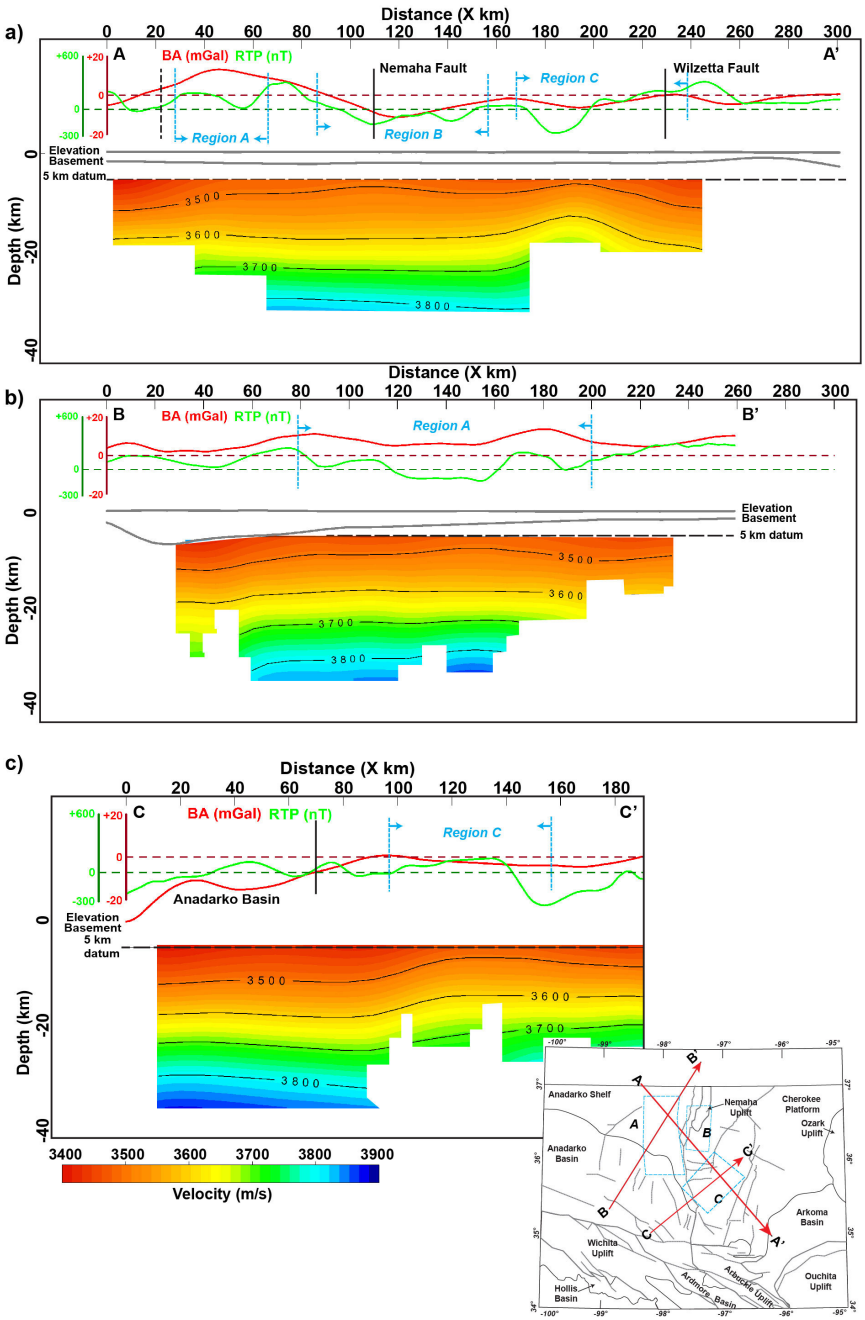


Figure 3.9: Sg velocity model cross sections. Bouguer gravity anomaly (red curve) and magnetic anomalies (green curve) are plotted above corresponding cross sections. On cross sections, black vertical lines show fault locations and blue vertical lines show extent of Regions (A, B, and C). Inset maps show the fault locations (gray lines), location of Regions A, B, and C (blue polygons) overlain on geologic province map. See text for discussion.

3.5.3 V_P/V_S Ratio and Compositional Analysis

Individually, P wave velocities and S wave velocities provide a non-unique interpretation for the composition of the rocks. Apart from the rock composition, P and S wave velocities are also affected by the pressure and temperature conditions of the crust. Instead, the V_P/V_S ratio or Poisson's ratio are widely used to constrain the crustal composition as they are largely unaffected by pressure temperature conditions at crustal depths (Christensen, 1996). We compute V_P/V_S ratio for Oklahoma using the P and S wave velocities obtained from the same methodology of stacking and inversion of local earthquake waveforms. This approach of calculating of V_P/V_S ratios minimizes any inherent potential biases introduced through systematic over- or under-estimation of P and S wave velocities. Unlike the V_P/V_S estimates from receiver functions, our approach does not require assumption of velocities or Moho depth, which further reduces sources of error. As the resolution of both the velocity data are comparable, we get reliable V_P/V_S estimates as a function of depth.

Figure 3.7 shows depth slices for V_P/V_S computed using the P wave velocities from Ratre and Behm (2021) and S wave velocities from this study. We consistently see a higher than surrounding V_P/V_S ratio for Region A which also corresponds to a high gravity anomaly. We observe a generally increasing V_P/V_S for the crust in Oklahoma going to a maximum of 1.85 at 39 km depth. A high V_P/V_S is a strong indication of a mafic material in the crust. This also corroborates the high average V_P/V_S reported by McGlannan and Gilbert (2016); Wang et al. (2019); Zeng and Nowack (2021). Figure 3.10a shows V_P/V_S vs V_P distribution for upper (average $V_P/V_S = 1.75$), middle (average $V_P/V_S = 1.77$), and lower (average $V_P/V_S = 1.80$) crust. We compare our data to the V_P and V_S empirical relationships derived by Brocher (2005). The "Mafic line" is derived based on measurements from calcium-rich

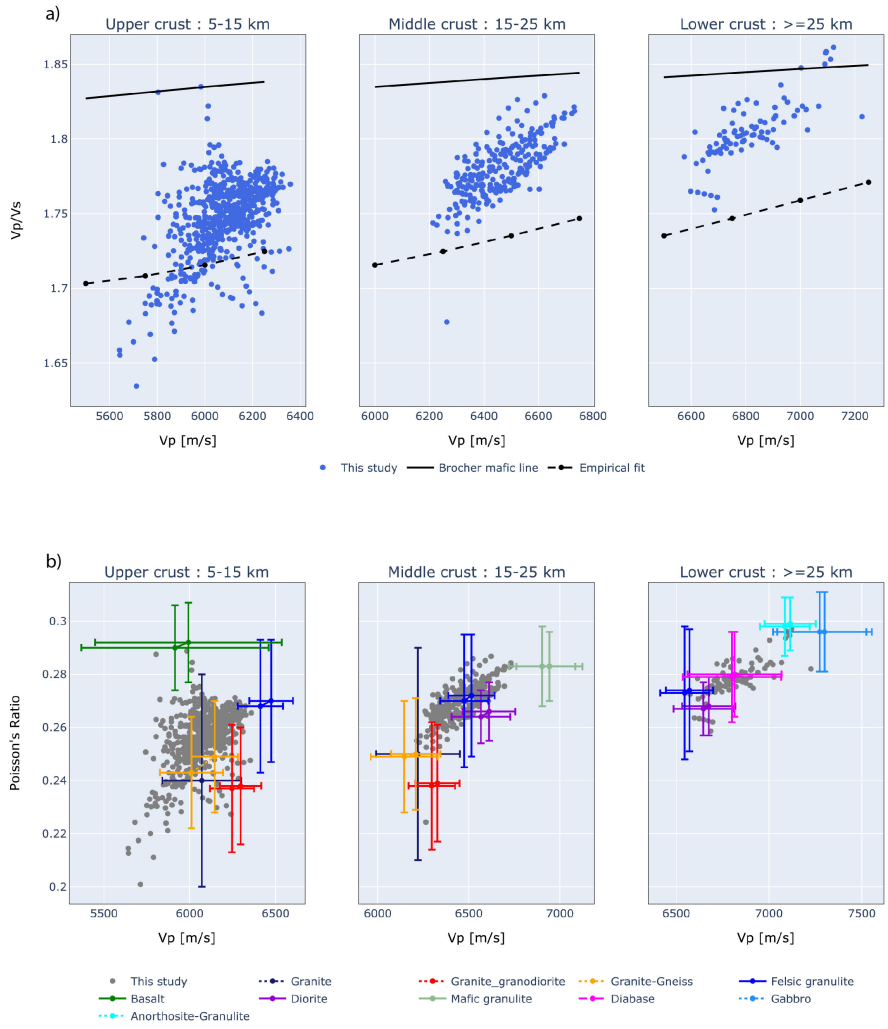


Figure 3.10: Plots of (a)V_P/V_S vs V_P and (b) Poisson's ratio vs V_P for upper, middle and lower crust of Oklahoma. Plots compare the data from this study to a) V_P and V_S relationships derived by Brocher (2005); b) Poisson's ratio and V_P values for different rock types compiled by Christensen (1996). Multiple values for the same rock type for the upper, middle and lower crust represent the values at two different lithostatic pressure that would correspond to the the specific layer [Upper crust : 200, 400 MPa, Middle crust : 400, 600 MPa, Lower crust : 800, 1000 MPa. Error bars for rock types represent one standard deviation.

rocks, mafic rocks, serpentinites, and gabbros. The empirical fit on the other hand excludes these rocks. These two lines represent average values for extreme cases for mafic and felsic rocks. Our data shows a clear trend favouring

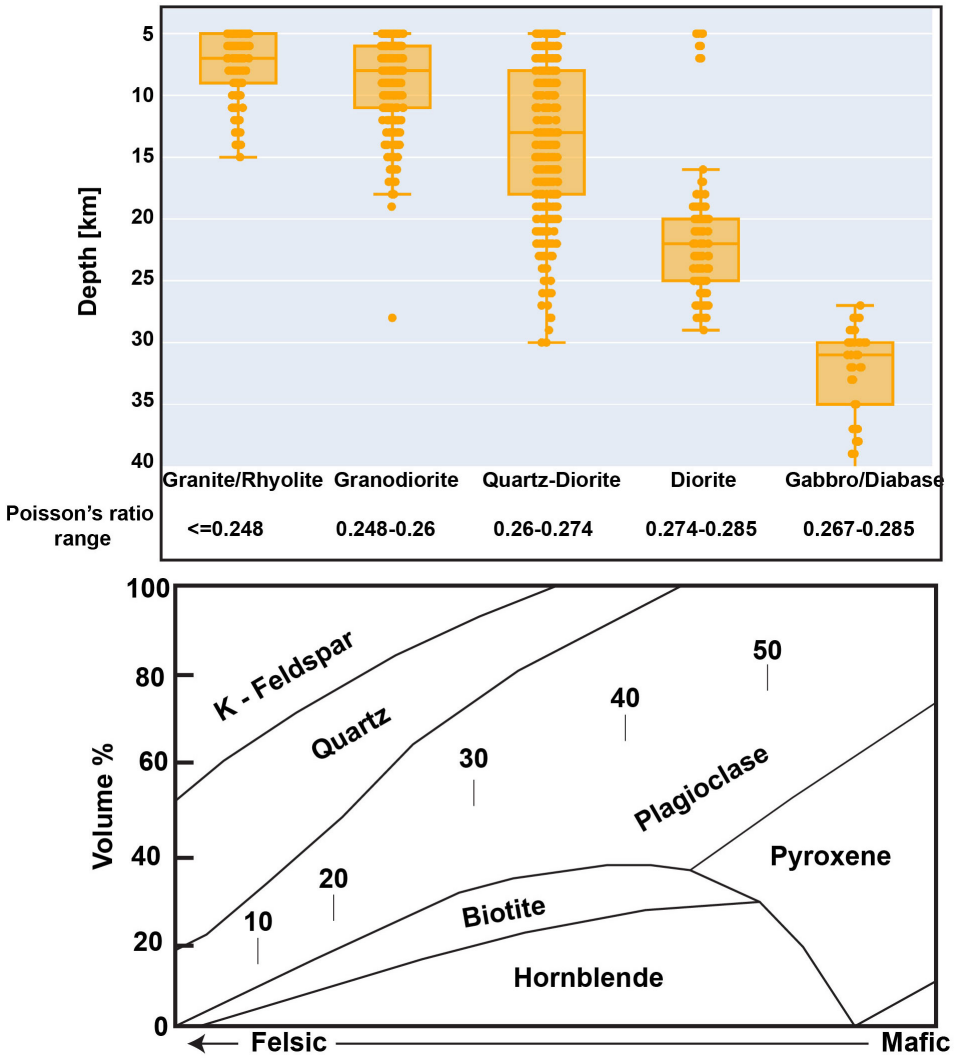


Figure 3.11: Box plot showing the distribution of Poisson's ratio data from this study across depth and mineral composition. Center horizontal line in each box plot diagram represents the median depth. The data are sorted according to Poisson's ratio and P wave velocity bounds of each of the rock types. Anorthite content shown within the plagioclase field.

the empirical fit consisting of majorly felsic rock types for upper crustal rocks and moves towards the mafic line approximation for the lower crustal rocks (Figure 3.10a). SGRP rocks are generally considered to have high K and low anorthite content (Bickford and Lewis, 1979; Barnes et al., 2002) which is possibly why the "Mafic line" as proposed by Brocher (2005) may not fit our

dataset.

Christensen (1996) and Holbrook et al. (1992a) compiled average V_P, V_S, and Poisson's ratio values for a variety of rock types and mineral assemblages at crustal lithostatic pressures ranging from 200-1000 MPa. These values for different rocks types are plotted in Figure 3.10b, along with our dataset. We also compare our data to basic mineral classification for felsic-mafic rocks in Figure 3.11. Upper crust in Oklahoma is dominated by high-K granite, followed by granodiorite, and granite gneiss (Figure 3.10b,3.11) as reported by several petrological studies for SGRP (Barnes et al., 2002; Bickford et al., 2015). High percentage of felsic igneous rocks also implies that the upper crust has not undergone a lot of deformation and is mostly unmetamorphosed. High alkali content is congruous with the presence of A-type granitic plutons found throughout the SGRP. The middle crust is dominated by metamorphic rock facies like felsic granulite followed by diabase (mafic), diorite (intermediate), and granite. These observations are consistent with the hypothesis that SGRP was formed through crustal melting possibly induced by basaltic underplating as the heat and temperatures would lead to most of the metamorphism in the middle crust. In the lower crust, our V_P/V_S estimates predict increasingly more mafic composition with depth. Comparison to the Christensen (1996) mineral assemblage data suggest that the lower crust is possibly dominated by diabase along with some gabbro, anorthosite, and diorite. A possible explanation for the presence of anorthosite in the deeper crust can be linked to the partial melting of magma that causes the crust to melt. Magma at the base of the crust without an outlet fractionates and crystallizes the mafic minerals leaving a plagioclase rich magma that can crystallizes to form anorthosites. A more detailed analysis is required to assess the mineral composition and rock type present in the deeper crust.

3.6 Conclusions

In this study, we apply CMP sorting, stacking, and inversion techniques to local earthquake waveforms to develop a 3-D save velocity model for central Oklahoma. We present a higher resolution shear wave velocity model compared to the ambient noise velocity models available for Oklahoma. We combine our model with the previously published P wave velocity model that was generated through similar methodology to obtain V_P/V_S and Poisson's ratio estimates. We compare our data with the published estimates of V_P, V_S and Poisson's ratio to perform compositional assessment for the crust in Oklahoma. Our results suggest that the upper crust in Oklahoma is dominated by felsic granite and granodiorite suites. We interpret the presence of basaltic compositions in the upper-middle crust as related to the mafic intra-basement layering in the upper crust. The Poisson's ratio and V_P/V_S estimates suggest that the bulk of middle crust is composed of metamorphic and intermediate rocks that gradually becomes more mafic as it transitions into lower crustal depths. Qualitative compositional assessment from Poisson's ratio for the lower crust suggests a mafic lower crust which strongly suggests partial melting and subsequent basaltic underplating as the primary process of formation of the SGRP.

The velocity model presented in this study can be used as initial models for high resolution tomography studies or to improve earthquake locations. Similarly, S wave velocity model and the V_P/V_S model can be used to improve upon the initial assumptions of the crustal parameters for ambient noise studies in the region. Future work will focus on inverting for major element oxide compositions using the P and S wave velocities generated in our study. Major element composition can provide more detail to the compositional analysis carried out in this study which will be used to further define the tectonic

processes that led to the formation of the SGRP.

Bibliography

Agena, W. F., Lee, M. W., and Grow, J. A. (1989). Reprocessing of the CO-CORP data recorded across the Wichita Mountain uplift and the Anadarko basin in southern Oklahoma. Technical report.

Barnes, M. A., Anthony, E. Y., Williams, I., and Asquith, G. B. (2002). Architecture of a 1.38–1.34 ga granite–rhyolite complex as revealed by geochronology and isotopic and elemental geochemistry of subsurface samples from west texas, usa. *Precambrian Research*, 119(1-4):9–43.

Behm, M., Brückl, E., Chwatal, W., and Thybo, H. (2007). Application of stacking and inversion techniques to three-dimensional wide-angle reflection and refraction seismic data of the Eastern Alps. *Geophysical Journal International*, 170(1):275–298.

Bickford, M. E., Harrower, K. L., Hoppe, W. J., Nelson, B. K., Nusbaum, R. L., and Thomas, J. J. (1981). Rb-Sr and U-Pb geochronology and distribution of rock types in the Precambrian basement of Missouri and Kansas. *Geological Society of America Bulletin*, 92:323–341.

Bickford, M. E. and Lewis, R. D. (1979). U-Pb geochronology of exposed basement rocks in Oklahoma. *Geological Society of America Bulletin*, 90(6):540.

Bickford, M. E., Van Schmus, W., Karlstrom, K., Mueller, P., and Kamenov, G. (2015). Mesoproterozoic-trans-Laurentian magmatism: A synthesis of continent-wide age distributions, new SIMS U–Pb ages, zircon saturation temperatures, and Hf and Nd isotopic compositions. *Precambrian Research*, 265:286–312.

Blackwell, D., Richards, M., Frone, Z., Batir, J., Ruzo, A., Dingwall, R., and Williams, M. (2011). Temperature-at-depth maps for the conterminous us

and geothermal resource estimates. Technical report, Southern Methodist University Geothermal Laboratory, Dallas, TX (United States).

Brewer, J. A., Brown, L. D., Steiner, D., Oliver, J. E., Kaufman, S., and Denison, R. E. (1981). Proterozoic basin in the southern Midcontinent of the United States revealed by COCORP deep seismic reflection profiling. *Geology*, 9(12):569.

Brewer, J. A., Good, R., Oliver, J. E., Brown, L. D., and Kaufman, S. (1983). COCORP profiling across the Southern Oklahoma aulacogen: Overthrusting of the Wichita Mountains and compression within the Anadarko Basin. *Geology*, 11(2):109.

Brewer, J. A., Good, R., Oliver, J. E., Brown, L. D., and Kaufman, S. (1984). COCORP deep seismic reflection traverse across the southern Oklahoma Aulacogen. *Technical Proceedings of the 1981 AAPG Mid-Continent Regional Meeting, 1984*, pages 191–194.

Brewer, J. A. and Oliver, J. E. (1980). Seismic reflection studies of deep crustal structure. *Annual Review of Earth and Planetary Sciences*, 8(205-230).

Brocher, T. M. (2005). Empirical relations between elastic wavespeeds and density in the earth's crust. *Bulletin of the seismological Society of America*, 95(6):2081–2092.

Buckey, A. (2012). An integrated geophysical analysis of crustal structure in the Wichita Uplift region of southern Oklahoma. *The Shale Shaker*, 62(6):432–452.

Chen, C. (2016). *Comprehensive analysis of Oklahoma earthquakes: from earthquake monitoring to 3D tomography and relocation.* PhD thesis, University of Oklahoma.

Christensen, N. I. (1996). Poisson's ratio and crustal seismology. *Journal of Geophysical Research: Solid Earth*, 101(B2):3139–3156.

Christensen, N. I. and Mooney, W. D. (1995). Seismic velocity structure and composition of the continental crust: A global view. *Journal of Geophysical Research*, 100(B6):9761–9788.

Denison, R. E., Lidiak, E. G., Bickford, M. E., and Kisvarsanyi, E. B. (1984). Geology and geochronology of Precambrian rocks in the Central Interior region of the United States. *US Geological Survey Professional Paper*, 1241 C:1–13.

Elebiju, O. O., Matson, S., Randy Keller, G., and Marfurt, K. J. (2011). Integrated geophysical studies of the basement structures, the Mississippi chert, and the Arbuckle Group of Osage County region, Oklahoma. *AAPG Bulletin*, 95(3):371–393.

Evanzia, D., Pulliam, J., Ainsworth, R., Gurrola, H., and Pratt, K. (2014). Seismic Vp & Vs tomography of Texas & Oklahoma with a focus on the Gulf Coast margin. *Earth and Planetary Science Letters*, 402(C):148–156.

Holbrook, W. S., Mooney, W. D., and Christensen, N. I. (1992a). The seismic velocity structure of the deep continental crust. *Continental lower crust*, 23:1–43.

Holbrook, W. S., Mooney, W. D., and Christensen, N. I. (1992b). The seismic velocity structure of the deep continental crust in Continental Lower Crust. *Continental Lower Crust*, pages 1–43.

Kolawole, F., Simpson Turko, M., and Carpenter, B. M. (2020). Basement-controlled deformation of sedimentary sequences, Anadarko Shelf, Oklahoma. *Basin Research*, (August 2019):bre.12433.

Lidiak, E. G. (1996). Geochemistry of subsurface Proterozoic rocks in the eastern Midcontinent of the United States: Further evidence for a within-plate tectonic setting. In *Basement and basins of eastern North America*, volume 308, pages 45–66. Geological Society of America.

Marsh, S. (2018). Development of a state-wide velocity profile in oklahoma using ambient noise seismic tomography.

McBride, J. H., William Keach, R., Leetaru, H. E., and Smith, K. M. (2018). Visualizing Precambrian basement tectonics beneath a carbon capture and storage site, Illinois Basin. *Interpretation*, 6(2):T257–T270.

McGlannan, A. J. and Gilbert, H. (2016). Crustal signatures of the tectonic development of the North American midcontinent. *Earth and Planetary Science Letters*, 433:339–349.

Mitchell, B. and Landisman, M. (1970). Interpretation of a crustal section across Oklahoma. *Geological Society of America Bulletin*, 81:2647–2656.

Musacchio, G., Mooney, W. D., Luetgert, J. H., and Christensen, N. I. (1997). Composition of the crust in the grenville and appalachian provinces of north america inferred from vp/vs ratios. *Journal of Geophysical Research: Solid Earth*, 102(B7):15225–15241.

Nelson, B. K. and DePaolo, D. J. (1985). Rapid production of continental crust 1.7 to 1.9 b.y. ago: Nd isotopic evidence from the basement of the North American mid-continent. *Geological Society of America Bulletin*, 96(6):746.

Pei, S., Peng, Z., and Chen, X. (2018). Locations of Injection-Induced Earthquakes in Oklahoma Controlled by Crustal Structures. *Journal of Geophysical Research: Solid Earth*, 123(3):2332–2344.

Phinney, R. A. and Jurdy, D. M. (1979). Seismic imaging of deep crust. *Geophysics*, 44(10):1637–1660.

Ratre, P. and Behm, M. (2021). Imaging the deep crustal structure of central oklahoma using stacking and inversion of local earthquake waveforms. *Journal of Geophysical Research: Solid Earth*, 126(5):e2020JB021368. e2020JB021368 2020JB021368.

Schoenball, M. and Ellsworth, W. L. (2017). Waveform-Relocated Earthquake Catalog for Oklahoma and Southern Kansas Illuminates the Regional Fault Network. *Seismological Research Letters*, 88(5):1252–1258.

Shen, W. and Ritzwoller, M. H. (2016). Crustal and uppermost mantle structure beneath the United States. *Journal of Geophysical Research: Solid Earth*, 121(6):4306–4342.

Tan, J., Langston, C. A., and Ni, S. (2021). Shallow shear-wave velocity structure in oklahoma based on the joint inversion of ambient noise dispersion and teleseismic p-wave receiver functions. *Bulletin of the Seismological Society of America*, 111(2):654–670.

Toth, C. R. (2014). *Separation of the Earthquake Tomography Inverse Problem to Refine Hypocenter Locations and Tomographic Models: A Case Study from Central Oklahoma*. PhD thesis, University of Oklahoma.

Tryggvason, E. and Qualls, B. R. (1967). Seismic refraction measurements of crustal structure in Oklahoma. *Journal of Geophysical Research*, 72(14):3738–3740.

Wang, Z., Persaud, P., and Behm, M. (2019). Investigation of the crust in oklahoma from broadband teleseismic receiver functions. In *AGU Fall Meeting Abstracts*, volume 2019, pages T21F–0401.

Xing, G., Niu, F., Chen, M., and Yang, Y. (2016). Effects of shallow density structure on the inversion for crustal shear wave speeds in surface wave tomography. *Geophysical Journal International*, 205(2):1144–1152.

Zeng, Q. and Nowack, R. L. (2021). Analysis of local seismic events near a large-n array for moho reflections. *Seismological Society of America*, 92(1):408–420.

Zhu, H. (2018). Crustal wave speed structure of North Texas and Oklahoma based on ambient noise cross-correlation functions and adjoint tomography. *Geophysical Journal International*, 214(1):716–730.

Zhu, X. and McMechan, G. A. (1989). 2-D tomographic imaging of velocities in the Wichita uplift-Anadarko basin region of southwestern Oklahoma. *Bulletin of the Seismological Society of America*, 79(3):873–887.

Chapter 4

Earthquake depth and local velocity estimation using crustal reverberations and phase correlation for the Cushing Fault zone

4.1 Abstract

The significant rise in the seismicity in Oklahoma due to wastewater injection has reactivated several dormant fault zones in the region. The Cushing Fault zone in central Oklahoma is one such location that has observed several M>4 earthquakes. Accurate earthquake location estimates is a key parameter to understand hazard and injection-induced triggering mechanism. Several earthquake relocation algorithms reduce the errors in lateral earthquake locations, but earthquake depth remains a challenge due to lack of accurate velocity model and trade-off during inversion. In 2019, we deployed a dense network of 130 5Hz 3-component Fairfield nodes covering the Cushing Fault Zone. We use the data recorded by this array for three events within the Cushing Fault Zone and observe phase conversions for all the three events.

To model these phase conversions, we first use Velest algorithm to relocate earthquakes using a 1D local velocity model. Then, we perform forward travel time modelling to evaluate the effects of basement depth, earthquake depth, and velocity changes on the different phase arrivals. The forward modeling results suggest that these converted phases are S-to-P conversion (S_P) at the basement interface. We further compute synthetic seismograms using F-K algorithm to model the converted phase. We use the observed delay times between S and S_P phases to determine the basement depth. We use delay times between P and S_P phases to constrain earthquake depths. The lateral earthquake locations are constrained through Velest, and depth estimates are enhanced by the delay time from the converted phase.

4.2 Introduction

In the past decade, Oklahoma experienced an exponential rise in seismicity, primarily attributed to wastewater disposal in the subsurface (Ellsworth, 2013; Keranen et al., 2014; Walsh and Zoback, 2015; Weingarten et al., 2015). The pore pressure changes resulting from fluid injection coupled with local and regional stress conditions have led to reactivation of previously unmapped faults in the crystalline basement (Alt and Zoback, 2017; Keranen et al., 2013; McNamara et al., 2015a; Yeck et al., 2016). One such fault system has been the Cushing fault zone in northern Oklahoma which has experienced several $>$ 4 M earthquakes and a M5.0 earthquake sequence (McNamara et al., 2015b). Although the frequency of earthquakes has decreased in the past few years due to earthquake mitigation activities (McNamara et al., 2015b; Langenbruch and Zoback, 2016), one of the largest earthquake event recorded in Oklahoma, M5.8 in Pawnee, occurred during this period (Yeck et al., 2017).

Cushing, Oklahoma is an important oil and gas transportation hub and is one of the largest crude oil storage facilities in the United States. These strategic assets are situated above a complex system of conjugate faults known as the Cushing fault zone. Cushing fault itself serves as a conjugate fault structure to the more prominent Wilzetta Fault Zone in Oklahoma (Figure 4.1). The Cushing fault was previously unmapped and was reactivated as a result of M4 and M4.3 earthquake sequences in October 2014 (McNamara et al., 2015b). An M5.0 mainshock event occurred within the Cushing fault zone in 2016. These subsequent earthquakes reactivated another unmapped fault in the Cushing fault zone. So far, these earthquakes have not caused any significant damage to the strategic oil reserve facility but have yielded extensive structural damage to properties in the city. (McNamara et al., 2015b) postulates a future occurrence of a >M5.0 earthquake that could cause damage to the critical infrastructure in the region.

Cushing fault zone is located in the Cherokee Platform province where the shallow crystalline basement is covered by a thin sedimentary layer (Johnson, 2008). Most of the earthquakes in the Cushing fault zone have occurred in the shallow crystalline basement between 3-5 km (McNamara et al., 2015b). In order to understand earthquake triggering mechanisms and conduct accurate stress analysis with respect to the local fluid injection activities, we need precise earthquake depth locations. Due to the absence of an accurate velocity model in the region and sparse station coverage, earthquake depth and origin times could have large errors. In this study, we model delay times between different crustal phases using travel time modelling and forward waveform modelling to characterize the basement depth, velocity model, and earthquake depths. We use vertical component records for subsequent modelling and comparison. Figure 4.1 shows the earthquake and station locations in Oklahoma.

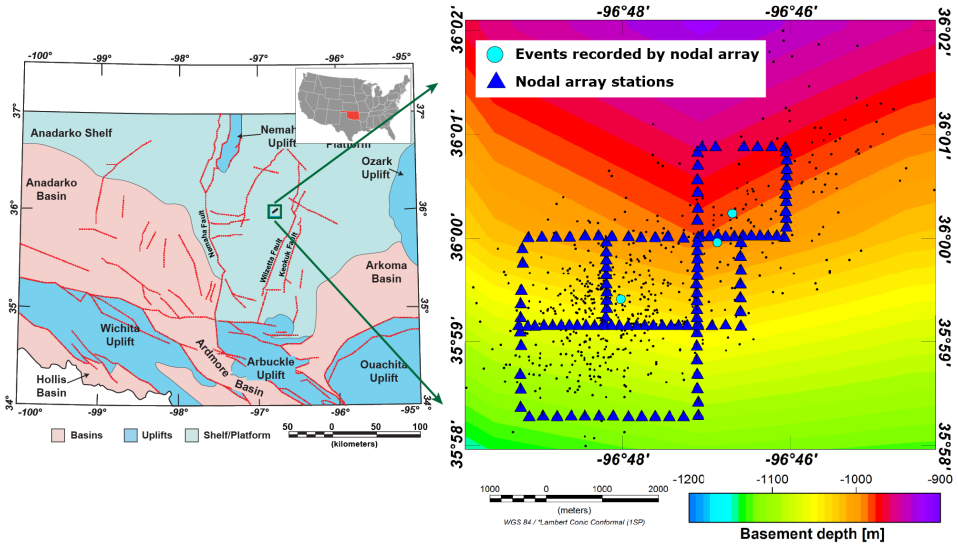


Figure 4.1: Left: Overview of tectonic provinces and faults in Oklahoma. The black square shows the location of the Cushing Fault zone. Right: Map view of nodal array stations (blue triangles) and earthquake locations (black dots) from Oklahoma Geological Survey (OGS) catalog from October 2014 to May 2018. The background is the basement depth map derived from basement penetrating wells (Northcutt and Campbell, 1996). The three cyan circles indicate earthquakes used in this study.

4.3 Data

In this study, we use data from 130 ZLAND Fairfield nodes deployed from November 5th, 2019 to December 16th, 2019 in Cushing, Oklahoma. The nodes were deployed with a dense spacing of 200±50 m in a grid pattern along the roads. Three events are recorded within the array and are used for further processing in this study. The data are recorded with a sampling rate of 500 Hz and filtered between 1 and 20 Hz. An autopicker (Li and Peng, 2016) is used to pick the initial P and S arrivals and the waveforms are trimmed into 4-second segments, taking the origin time of each event as 0 s. Original locations for the three events are shown in Figure 4.1 (Table 4.1). For all three events, we observe a shallow crustal phase that arrives between P and S arrivals (Figure 4.2a,b).

4.4 Methodology

We follow the following workflow to process and analyze our data:

- Relocate the three cataloged earthquakes using Velest algorithm (Kissling et al., 1994) and a local 1D velocity model from Tan et al. (2021) (Figure 4.2c).
- Perform travel time modeling to identify the shallow crustal phase observed between P and S arrivals.
- Use delay time estimates from travel time modelling to constrain basement depth.
- Use the basement depth constraints derived from previous step to perform forward waveform modelling and constrain earthquake depth.

4.4.1 Earthquake Relocation

We perform relocation for the three events using a recently published shear wave velocity model by Tan et al. (2021). We use V_P/V_S ratio of 1.73 to get the P wave velocity model for the region. We use single-event mode in the Velest algorithm (Kissling et al., 1994) to keep the velocity constant and only performed event relocation. We do not perform joint inversion of velocity model and event location due to insufficient number of events. A future study with more complete event detection can improve local velocity estimation. We determine the confidence intervals for the location estimates through bootstrapping, by randomly selecting 80% of the travel time data to derive the event relocations and repeating 50 times. Relocated events and re-aligned waveforms along with the velocity model are shown in Figure 4.2. The location uncertainties from bootstrapping are shown in Figure 4.3.

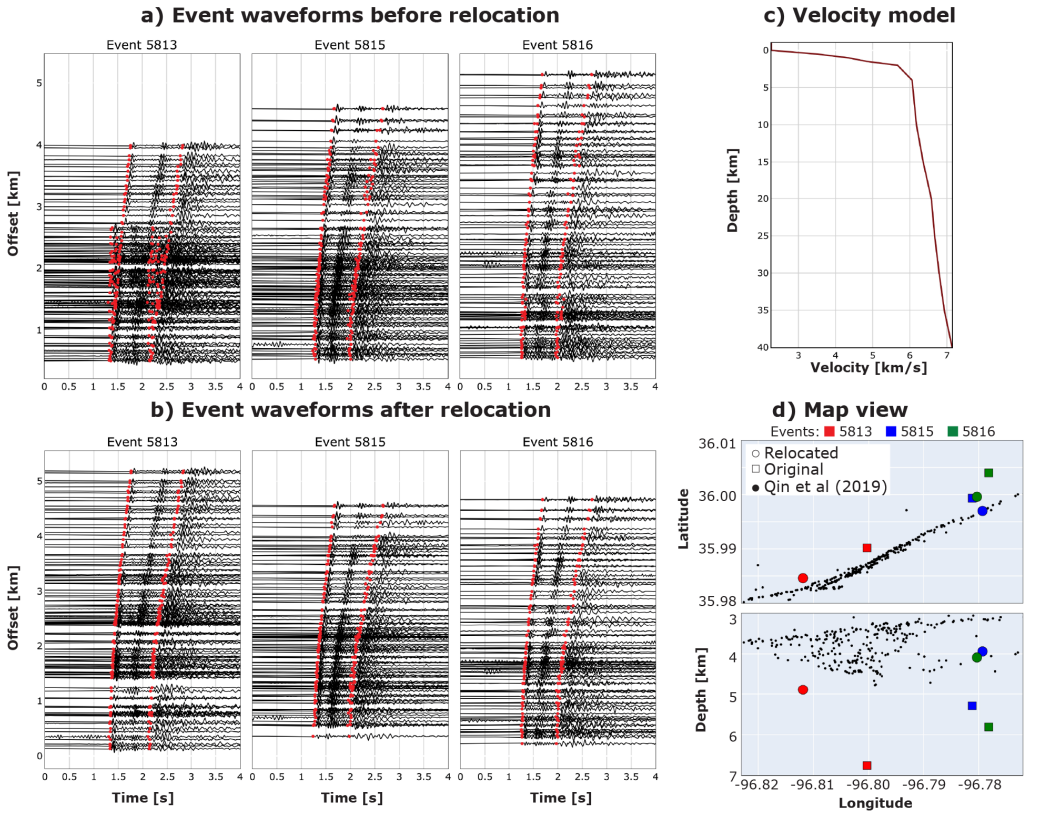


Figure 4.2: a,b)Event waveform aligned using the original catalog location and relocation from Velest. Red dots indicate the picked P and S arrival times for each event. c) P wave velocity model derived from Tan et al. (2021) used for relocation. d) Map and cross section views showing the location of events before and after Velest relocation. Black dots denote seismicity used in Qin et al. (2019) for the Cushing fault zone.

4.4.2 Travel Time Modeling

4.4.2.1 Phase Identification

Figure 4.2b shows distinct shallow crustal phase arrivals between the initial P and S arrivals. Visual inspection of the observed waveform suggests that the crustal phase may represent a phase conversion at the sediment-basement interface. This is because the second crustal phase to arrive is much faster that the initial S arrival and thus cannot represent a deep crustal phase. The sedimentary layers in the Cherokee platform are composed of inter-bedded

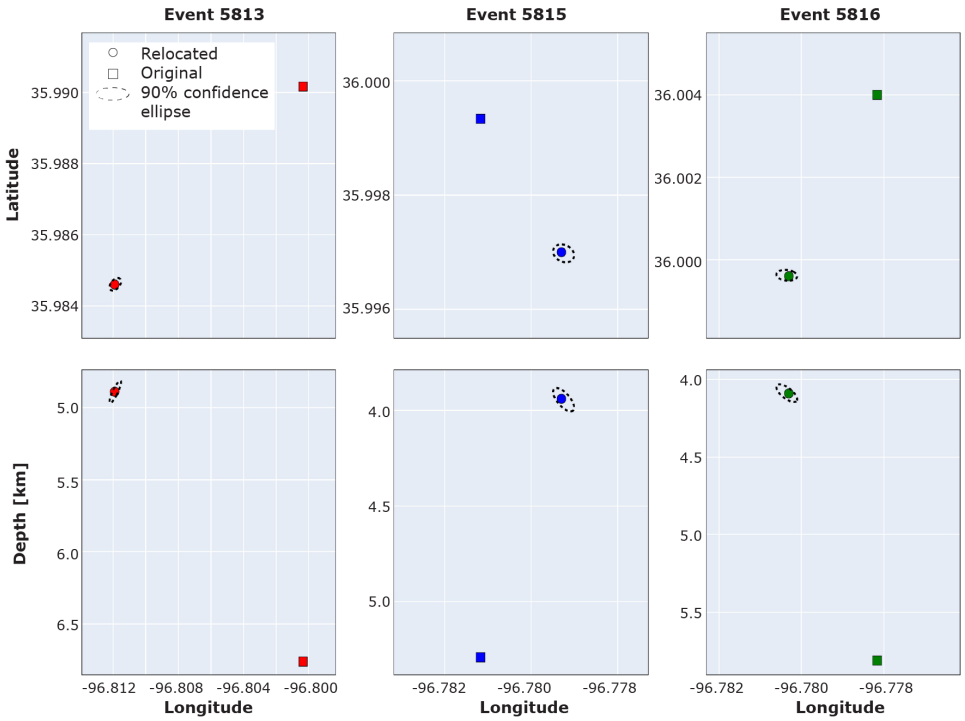


Figure 4.3: Map and cross section view for the three events showing the 90% confidence interval (black dashed ellipse) based on bootstraping.

sandstone, shale, and limestones (Johnson, 2008) and the basement is composed of Precambrian granite-rhyolite rocks. The significant contrast between the Precambrian basement and the sedimentary rocks can cause the phase conversion observed in our data. To identify this crustal phase we perform travel-time modelling using a simple two-layered earth model. We model the arrival times for phases P, S, and P to S (P_S) and S to P (S_P) conversions at a given basement interface for differing values of offsets. Figure 4.4 shows comparison between modelled travel times for different phases and waveforms for one of the events. Due to assumptions in basement depth, velocity model, and earthquake depth the arrival times for the different phases for modelled travel times do not have an absolute match with the observed arrivals but the relative delay time variations between different phases can be used to identify the phase observed in the data. Our modeling results reveal that the

converted phase observed is an S to P conversion possibly occurring at the sediment-basement interface.

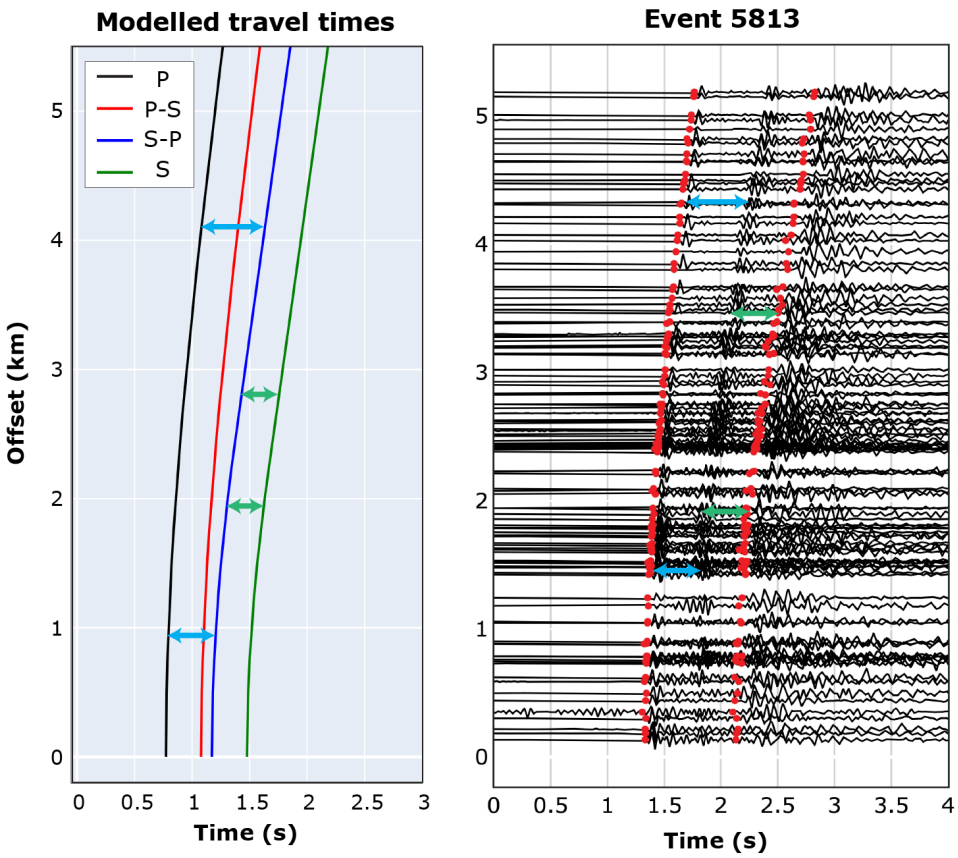


Figure 4.4: Comparison of modelled travel times for different phases and observed data. Blue arrows show increase in delay time between P and S-to-P phases with offset and a similar observation noted on observed waveform. Green arrows show the almost constant delay time between S-to-P and S phases in the modelled waveform which is consistent with the observed arrivals as shown.

4.4.2.2 Basement Depth Determination

Various factors like event-station distance, earthquake depth, basement depth, and V_P/V_S ratio can influence the delay time between phases. To determine the dependency of each of these factors, we look at the travel time

for a given phase for a simple two layer model as given by:

$$T(p) = \frac{u_1^2 \Delta h}{\sqrt{u_1^2 - p^2}} + \frac{u_2^2 \Delta (z - h)}{\sqrt{u_2^2 - p^2}} \tag{4.1}$$

where u_1, u_2 : are slowness of the phase for layer 1 and 2 respectively, h : basement depth, z : earthquake depth, and p : ray parameter. Layer 1 is assumed to be the sedimentary layer and layer 2 is assumed to be the basement layer. Once we identify the converted phase as S_P conversion at basement, we assess the influence of various factors on the time delay between each of the phase arrivals. We calculate travel time estimates for differing earthquake depths, basement depths, and local velocity estimates. From the above equation we determine that for a given velocity model, the delay time between S and S_P phase increases as the basement depth increases, and remains unaffected by any changes in offset and earthquake depth (Figure 4.5). Further, the delay times between S and S_P phase remain constant beyond an offset of 3.5 km for a given velocity and basement depth. On the other hand, the delay time between S_P and P phase depends on earthquake depth and offset for a given velocity model. So we first use delay time between S and S_P phase to constrain the basement depth and velocity model, then we use the delay time between S_P and P phase to constrain the earthquake depth.

We use an STA/LTA based picker to pick the S_P phase in the observed data for all three events. We compute delay times between S and S_P phases for the two layer model for differing basement depths and compare them to the delay times observed in the data to determine the basement depth in the study area. This step is important to constrain the basement depth prior to constraining the earthquake depths in the region. We use trial and error method to determine an appropriate V_P/V_S ratios for the sedimentary layer.

4.4.3 Forward Waveform Modelling and Earthquake Depth Estimation

We use the basement depth estimate and a favourable V_P/V_S ratio derived from travel time modelling to calculate synthetic seismograms of select stations. We use F-K modeling algorithm (Zhu, 2018) to model synthetic seismograms for all stations that recorded the three local events. The model space is represented by a 1-D velocity model with basement depth derived from travel time modelling. The source is defined as a right-lateral strike slip fault with strike, dip, and rake of 240°, 80°, and 180° respectively. The azimuth used in the calculation of the synthetic seismograms for each station was based on the location of the earthquake from Velest inversion. Earthquake depth is varied while keeping all the other parameters constant for a given station. Finally, for all the synthetic and observed waveforms, bandpass filter between 1 to 20 Hz was applied. The delay times between P and S_P, and P and S phases increase as the earthquake depth increases for a given velocity and basement depth. We use STA/LTA based picking algorithm to pick P, S_P, and S phases for the modelled waveforms. The delay time between P and S_P, and P and S also increase with increasing offset. This influence of offset is avoided as we only compare the modeled seismogram for each station to the respective observed waveforms. We compute the P and S_P delay times for the modelled waveforms. These are compared to the corresponding delay times observed in our data. We only use the P and S_P delay times to estimate earthquake depth as they do not depend on the V_P/V_S ratio of the sedimentary layer. The earthquake depth is estimated based on the minimization of residuals between observed and modeled delay time for P and S_P phases from all stations.

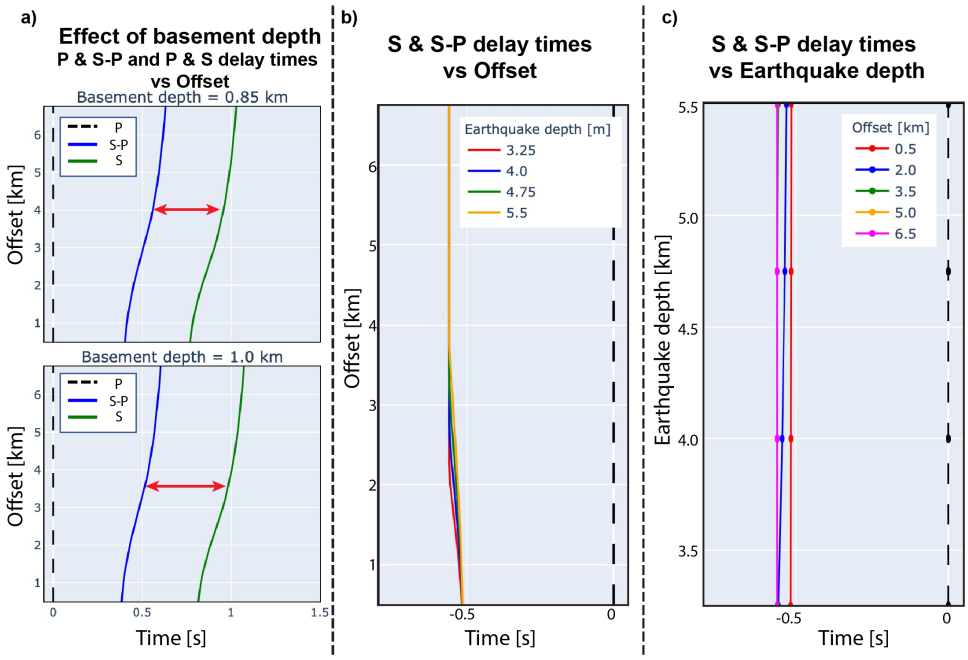


Figure 4.5: a)For a given velocity model: delay time between S and S_P increases as basement depth increases, b) Delay times between S and S_P arrivals vs offset when plotted for different earthquake depths shows that earthquake depth has almost no influence on the delay time beyond 3 km offsets, c) Delay times between S and S_P arrivals vs earthquake depth for different offsets, offsets beyond 3.5 km are not clearly differentiated as the delay times for those remain constant.

4.5 Results

4.5.1 Event Relocation

The relocated event locations are given in Table 4.2. The seismicity in the Cushing Fault Zone is concentrated within the uppermost basement up to 5 km depth. The three events are shifted to shallower depths after Velest relocation, which seem consistent to the event locations from Qin et al. (2019) (Figure 4.2). The improvement in location estimates can be clearly observed through the improvement in waveform alignment (i.e., comparing Figure 4.2a versus Figure 4.2b), especially for event 5813. We use these new event locations for further analysis.

Event ID	Origin time	Magnitude	Latitude	Longitude	Depth
5813	2019-11-14 18:26:11.81	2.48	35.9902	-96.8003	6.76
5815	2019-11-11 23:24:23.93	2.03	35.9993	-96.7812	5.29
5816	2019-11-06 18:19:12.91	1.61	36.0040	-96.7782	5.81

Table 4.1: Original event locations and magnitudes.

Event ID	Latitude	Longitude	Depth	Final depth
5813	35.9846	-96.8119	4.89	3.3
5815	35.9970	-96.7793	3.94	2.7
5816	35.9996	-96.7803	4.09	2.7

Table 4.2: Relocated event locations and depth estimates from Velest relocation. Last column shows the final depth estimates derived using phase delay times.

4.5.2 Basement Depth and V_P/V_S Estimates

We determine a V_P/V_S ratio of 2.5 for the sedimentary layer through trial and error method for our data. We calculate travel times for different phases by varying the basement depth and V_P/V_S ratios and compare the modeled times to observed data. Our modelling reveals that the V_P/V_S ratio for the sedimentary layer in our study area is 2.5. We use this V_P/V_S ratio for the further travel time modeling and forward waveform modeling. We use delay times for stations with an offset of 3.5 km or greater for each event to independently determine the basement depths at station locations. 70 out 126 stations (offsets $>$ 1 km) had basement depth in range 1.04-1.06 km determined from at least two events. The median depth estimate from each of the event is 1.052 km (Figure 4.6). The basement depth estimates from our method are consistent with the basement depth derived from basement penetrating wells (Campbell and Weber, 2006) in this region, which is $\sim$1 km.

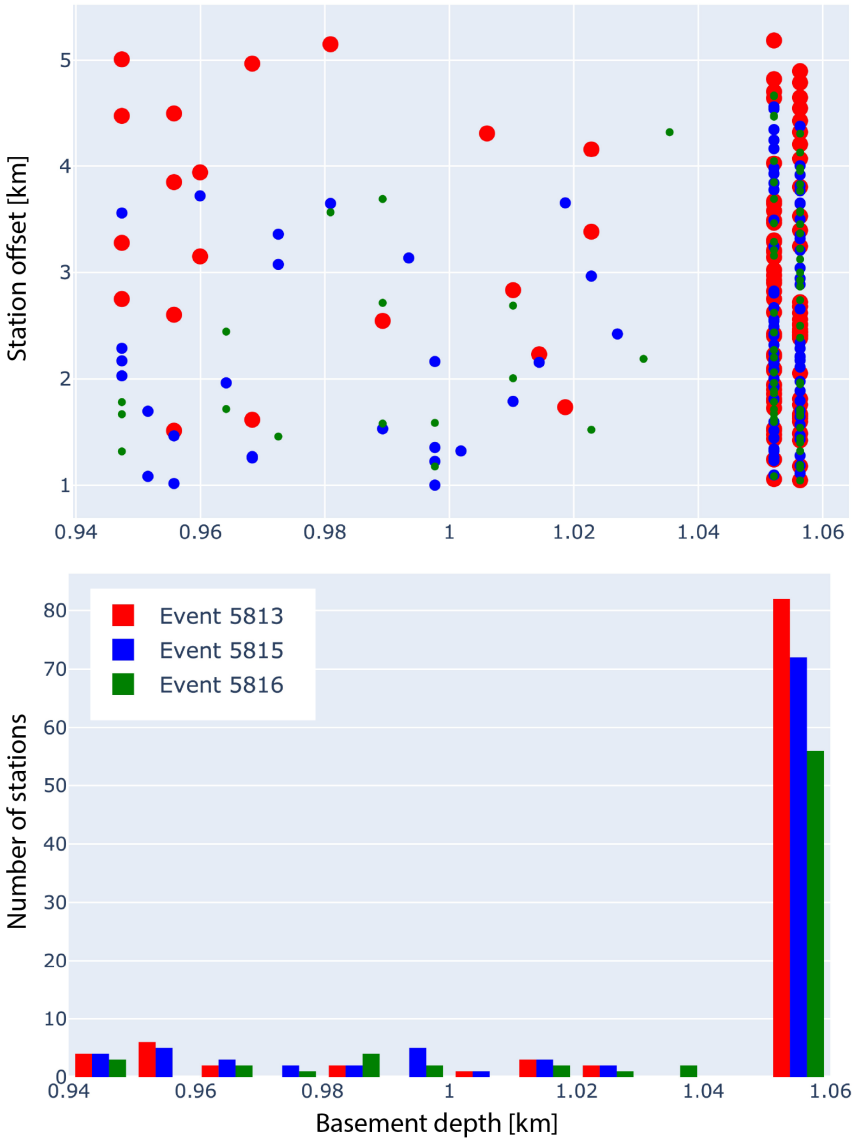


Figure 4.6: (top) Distribution of basement depth estimates at each station (offset >1 km) from each of the three events [Red:5813, Blue:5815, Green:5816], (bottom) histogram distribution of basement depth estimates show that basement depth estimates for majority of stations lie between 1.04 and 1.06 km.

4.5.3 Constraints on Earthquake Depth

The basement depth of 1.05 km is used to model synthetic seismograms using F-K algorithm (Zhu, 2018). We estimate the earthquake depths for the three events by minimizing the delay time residuals between observed and

modelled data for P and S_P phases. We obtain minimum combined residuals of ∼0.22, ∼0.22, and ∼0.23 for corresponding earthquake depths of 3.3 km, 2.7 km, and 2.7 km for events 5813, 5815, and 5816 respectively (Table 4.2). Figure 4.7 shows the total misfit for P and S_P delay time from all stations versus depth for the three events. We further discuss the implications of the residuals and the final earthquake depth estimates in the following section.

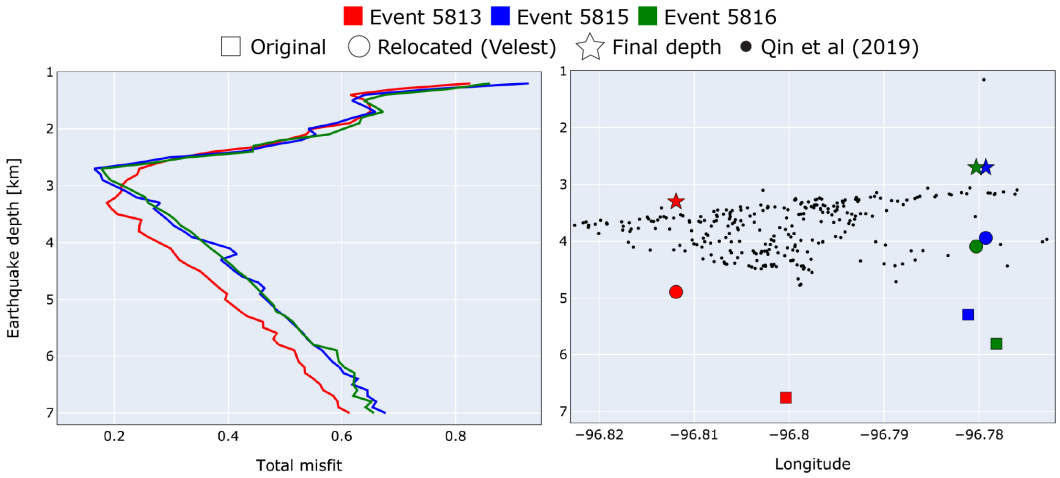


Figure 4.7: P - S_P delay time misfits plotted for the three events. Minimum value of misfit represents the chosen final depth estimates for each of the events.

4.6 Discussion

We identify S_P conversion at the sediment-basement interface in our data caused by high contrast in seismic velocities across the interface. Previously, shallow crustal reverberations have been used to constrain earthquake depth and shallow crustal structures (Frohlich et al., 2014; Mori, 1991). Our travel time modelling suggests that the delay times between P and S_P, S_P and S, and P and S are largely controlled by the sedimentary layer velocities, basement depth, and the earthquake depth. We develop a systematic methodology to

use the delay times between P and S_P, and S_P and S phases to constrain the basement depth and earthquake depths for the Cushing Fault zone.

The velocity model for the sedimentary layer is important to constrain, as most of the earthquakes are located in the shallow basement, so sediment velocity can play an important role in obtaining accurate event depths. Travel time modelling reveals that the V_P/V_S ratios for the sedimentary layers influence the delay times between S_P and S arrivals. High V_P/V_S ratio would suggest a shorter time delay between S_P and S phases while a larger V_P/V_S ratio would decrease the time between these phases. The delay times between S_P and S arrivals have a direct relationship with the basement depths which implies an increase in basement depth would increase the delay time between the two phases and vice versa. In this study, we estimate the V_P/V_S ratios for the sedimentary layers through trial and error approach.

Basement depth estimates from well data suggest basement depth variation of 0.9-1.1 km within the study area(Figure 4.1). We observe that basement depth largely controls the delay times between P and S_P, and S_P and S arrivals when all the other variables are kept constant. The delay times between P and S_P arrivals also depend on the earthquake depths while the S_P and S delay times remain constant with varying earthquake depths. This is consistent as the S to P conversion occurs at the basement interface and the time delay is only due to the basement depth and P and S wave velocities within the sedimentary layer. The independence of S_P and S delay times from earthquake depths is useful in constraining the shallow crustal structure, especially for areas with no basement well penetration, if the velocity model in the region is relatively well resolved. The travel time modelling for our data reveals a basement depth of $\sim$1.05 km for the Cushing Fault zone.

The earthquake depth estimates for the three events in the study area

range from ∼2.7-3.3 km (Table 4.2), which are consistent with the background seismicity (Figure 4.7). Previous studies have reported the depth range of 3-4.5 km for seismicity in the Cushing Fault zone (Qin et al., 2019). Our travel time models suggest that the earthquake depths largely control the delay times between P and S_P arrivals. These delay times are independent of the sedimentary layer velocities. Once basement depth is constrained, these delay times can be used to reliably constrain the earthquake depth in the region. To get a more accurate delay time estimate for the modelled data, we have generated synthetic seismograms using F-K algorithm by taking into account the fault geometry and station azimuths in the study area. We use velocity model derived from Tan et al. (2021) to compute these synthetic seismograms and use the V_P/V_S ratios derived from delay times. Delay times between converted phases derived from waveform modelling would be more reliable to estimate earthquake depths than the previous relocation using only P and S travel times.

The results for basement depth and earthquake depth estimates derived in this study can be further improved by reducing the uncertainties associated with the local velocity model. In the future, we aim to detect more local earthquakes and conduct a joint inversion of velocity model and earthquake location. This will reduce uncertainty of the V_P/V_S ratios for the sedimentary layers. In this study we used the fault orientation for the main Cushing Fault to generate synthetic waveforms, instead of focal mechanism solutions for individual earthquakes. Future work will include full waveform inversion to obtain more accurate source mechanism solutions.

4.7 Conclusions

In this study, we present results of basement depth and earthquake depth estimations from travel time and waveform modeling for three events recorded by the temporary nodal deployment in Cushing, Oklahoma. Travel time estimates for the event reveal a shallow basement depth of 1.05 km and slow sediment S wave velocities ($V_P/V_S = 2.5$). High V_P/V_S ratio can be related to the presence of fractures in the region. Phase delay times are affected by the basement depth, sedimentary velocity, and earthquake depth. Delay times between P and S_P, and S and S_P can be reliably used to estimate earthquake depth and basement depth respectively once the velocities are constrained for the sediment and basement layers.

Similar methodology can be used to estimate shallow crustal structure and earthquake depths in areas where similar phase conversions are recorded. Our future work will involve joint inversion to estimate velocity and earthquake locations to constrain the lateral location and obtain an improved velocity model. This will be followed by travel-time modelling assuming a variable V_P/V_S ratio for both sedimentary and basement layers to further constrain the velocity model, and a full waveform inversion to constrain earthquake depth and source mechanism.

Bibliography

Alt, R. C. and Zoback, M. D. (2017). In situ stress and active faulting in oklahoma. *Bulletin of the Seismological Society of America*, 107(1):216–228.

Campbell, J. A. and Weber, J. L. (2006). Wells drilled to basement to basement in Oklahoma. *Oklahoma Geological Survey Special Publication 2006-1*.

Ellsworth, W. L. (2013). Injection-Induced Earthquakes. *Science*, 341(6142):1225942–1225942.

Frohlich, C., Ellsworth, W., Brown, W. A., Brunt, M., Luetgert, J., MacDonald, T., and Walter, S. (2014). The 17 may 2012 m4. 8 earthquake near timpson, east texas: An event possibly triggered by fluid injection. *Journal of Geophysical Research: Solid Earth*, 119(1):581–593.

Johnson, K. (2008). Geologic History of Oklahoma. *Educational Publication*, 9:3–8.

Keranen, K. M., Savage, H. M., Abers, G. A., and Cochran, E. S. (2013). Potentially induced earthquakes in oklahoma, usa: Links between wastewater injection and the 2011 mw 5.7 earthquake sequence. *Geology*, 41(6):699–702.

Keranen, K. M., Weingarten, M., Abers, G. A., Bekins, B. A., and Ge, S. (2014). Sharp increase in central Oklahoma seismicity since 2008 induced by massive wastewater injection. *Science*, 345(6195):448–451.

Kissling, E., Ellsworth, W. L., Eberhart-Phillips, D., and Kradolfer, U. (1994). Initial reference models in local earthquake tomography. *Journal of Geophysical Research: Solid Earth*, 99(B10):19635–19646.

Langenbruch, C. and Zoback, M. D. (2016). How will induced seismicity in oklahoma respond to decreased saltwater injection rates? *Science Advances*, 2(11):e1601542.

Li, Z. and Peng, Z. (2016). An Automatic Phase Picker for Local Earthquakes with Predetermined Locations: Combining a Signal-to-Noise Ratio Detector with 1D Velocity Model Inversion. *Seismological Research Letters*, 87(6):1397–1405.

McNamara, D. E., Benz, H. M., Herrmann, R. B., Bergman, E. A., Earle, P., Holland, A., Baldwin, R., and Gassner, A. (2015a). Earthquake hypocenters and focal mechanisms in central oklahoma reveal a complex system of reactivated subsurface strike-slip faulting. *Geophysical Research Letters*, 42(8):2742–2749.

McNamara, D. E., Hayes, G. P., Benz, H. M., Williams, R., McMahon, N. D., Aster, R., Holland, A., Sickbert, T., Herrmann, R., Briggs, R., et al. (2015b). Reactivated faulting near cushing, oklahoma: Increased potential for a triggered earthquake in an area of united states strategic infrastructure. *Geophysical Research Letters*, 42(20):8328–8332.

Mori, J. (1991). Estimates of velocity structure and source depth using multiple p waves from aftershocks of the 1987 elmore ranch and superstition hills, california, earthquakes. *Bulletin of the Seismological Society of America*, 81(2):508–523.

Northcutt, R. A. and Campbell, J. A. (1996). Geologic Provinces of Oklahoma. *Shale Shaker*.

Qin, Y., Chen, X., Walter, J. I., Haffener, J., Trugman, D. T., Carpenter, B. M., Weingarten, M., and Kolawole, F. (2019). Deciphering the Stress

State of Seismogenic Faults in Oklahoma and Southern Kansas Based on an Improved Stress Map. *Journal of Geophysical Research: Solid Earth*, 124(12):12920–12934.

Tan, J., Langston, C. A., and Ni, S. (2021). Shallow shear-wave velocity structure in oklahoma based on the joint inversion of ambient noise dispersion and teleseismic p-wave receiver functions. *Bulletin of the Seismological Society of America*, 111(2):654–670.

Walsh, F. R. and Zoback, M. D. (2015). Oklahoma's recent earthquakes and saltwater disposal. *Science Advances*, 1(5):e1500195.

Weingarten, M., Ge, S., Godt, J. W., Bekins, B. A., and Rubinstein, J. L. (2015). High-rate injection is associated with the increase in u.s. mid-continent seismicity. *Science*, 348(6241):1336–1340.

Yeck, W. L., Hayes, G. P., McNamara, D. E., Rubinstein, J. L., Barnhart, W. D., Earle, P. S., and Benz, H. M. (2017). Oklahoma experiences largest earthquake during ongoing regional wastewater injection hazard mitigation efforts. *Geophysical Research Letters*, 44(2):711–717.

Yeck, W. L., Weingarten, M., Benz, H. M., McNamara, D. E., Bergman, E., Herrmann, R., Rubinstein, J. L., and Earle, P. S. (2016). Far-field pressurization likely caused one of the largest injection induced earthquakes by reactivating a large preexisting basement fault structure. *Geophysical Research Letters*, 43(19):10–198.

Zhu, H. (2018). Crustal wave speed structure of North Texas and Oklahoma based on ambient noise cross-correlation functions and adjoint tomography. *Geophysical Journal International*, 214(1):716–730.

Chapter 5

Conclusions and future work

5.1 Summary of Results

In this dissertation, I have modelled regional and local crustal structures in Oklahoma using induced seismicity. One of the goals of my work was to explore non-standard methodologies to evaluate local earthquake data sets. Some of the important results from my research are as follows:

- Common midpoint stacking and inversion methodology of processing active seismic data can be successfully adapted and applied to process local passive seismic data. Stacking of waveforms minimizes the errors associated with earthquake hypocenter and origin time and produce robust and deep crustal 3D seismic velocity models.

- The lower crust in Oklahoma has a mafic composition that provides evidence for origin of SGRP through basaltic underplating and crustal melting.

- We don't find evidence for the extension of an MCR-like structure into Oklahoma.

- Delay time between P, S, and shallow crustal converted phases like S_P and P_S can be used to uniquely determine the basement structure and enhance earthquake depth estimates.

The seismicity in Oklahoma has provided a unique natural laboratory to study earthquake processes in real time. Study of earthquake processes require knowledge about the crustal structure and the results of this dissertation provide a detailed image of the subsurface in Oklahoma.

In Chapter 2 and 3, I have used active seismic processing techniques of common midpoint stacking and inversion to generate 3-D P and S wave velocity models for Oklahoma using the local earthquake waveforms. In comparison to conventional earthquake travel-time tomography, which generally provides velocity model for the upper crust ($\sim$15 km depth), this methodology reveals the velocity structure up to 35-40 km depth (lower crust). The observed regional velocity anomalies generally conform with the major geologic structures (eg. Nemaha Uplift, Anadarko basin) and the gravity anomalies in the region. Further we combine the P and S wave velocity models to compute the V_P/V_S and Poisson's ratios. High V_P and high V_P/V_S ratio for the lower crust provides evidence for a mafic lower crust. This methodology provides robust V_P and V_S models that can be further used as initial model inputs for high resolution local earthquake tomography. Seismic velocity and Poisson's ratio variation with depth provides us with new observations for the deeper crust of Oklahoma and provides the necessary information to answer questions regarding the formation of the SGRP rocks. We interpret a felsic upper crust that is heterogeneous, intermediate/metamorphic middle crust that transitions into a mafic and more homogeneous lower crust. Our results demonstrate that the workflow described in Chapter 2 can be applied to similar data sets in other parts of the world.

In Chapter 4, I used the induced seismicity to look at the local structures in the Cushing Fault Zone in Oklahoma. A nodal array was deployed just above the Cushing Fault Zone and data recorded for three earthquakes within the array was used for delay time analysis. I established a methodology wherein I used the delay times between S and S_P phases to constrain the basement depth in the region. Further using waveform modelling I show that once the velocity model and basement structure is constrained, the delay times between S_P and P phases can be used to further enhance the earthquake depths. Constraining the earthquake depth is an important factor in studying and thus controlling the induced seismicity in Oklahoma.

5.2 Future Work

Oklahoma provides a unique opportunity in terms of the availability of passive seismic data that can be used to investigate the crust. The deeper crust requires further investigation to establish crustal compositions and derive more details regarding the processes involved in the formation and evolution of the Granite-Rhyolite province. The P and S wave velocities developed in this dissertation can be used to invert for major oxide composition similar to work by Behn and Kelemen (2003). The Poisson's ratio and V_P/V_S ratio for Oklahoma can be used to constrain the rock composition at a given pressure/temperature conditions. The velocity estimates can also be used to model the density structure in the region. The velocities can be used as initial models to develop high resolution velocity estimates or for relocation of earthquakes in the region.

In the last chapter, I presented the preliminary results for basement depth, earthquake depth, and local velocity model from travel time and forward waveform modeling. The relocation of the earthquakes did not involve inversion of

the velocity structure in the region. I will incorporate more events to simultaneously invert for the local velocity model along with earthquake relocation. For the computation of synthetic seismograms I used a constant focal mechanism solution published for the main Cushing fault (Qin et al., 2019). In future I will invert for the focal mechanisms of each of the events to compute the synthetic seismograms. This will give us more accurate waveform estimates for each of the events. I will add amplitude misfit as an added criteria along with the delay times to constrain the earthquake depth estimates.

Bibliography

Behn, M. D. and Kelemen, P. B. (2003). Relationship between seismic p-wave velocity and the composition of anhydrous igneous and meta-igneous rocks. *Geochemistry, Geophysics, Geosystems*, 4(5).

Qin, Y., Chen, X., Walter, J. I., Haffener, J., Trugman, D. T., Carpenter, B. M., Weingarten, M., and Kolawole, F. (2019). Deciphering the Stress State of Seismogenic Faults in Oklahoma and Southern Kansas Based on an Improved Stress Map. *Journal of Geophysical Research: Solid Earth*, 124(12):12920–12934.